Project Acronym:

SOUNDPET (INTEGRATED/0918/0008)

MRI-guided Focused ultraSOUND system for cancer in PETs
(dogs and cats)

Deliverable number: 2.6

Title: Publication in a scientific journal

Prepared by:

Marinos Giannakou (MEDSONIC, Limassol, Cyprus)
Nikolas Evripidou (CUT, Limassol, Cyprus)
Antria Filippou (CUT, Limassol, Cyprus)
Anastasia Antoniou (CUT, Limassol, Cyprus)
Andreas Georgiou (CUT, Limassol, Cyprus)
Christakis Damianou (CUT, Limassol, Cyprus)
Leonidas Georgiou (GOC, Limassol, Cyprus)
Theodora Christodoulou (GOC, Limassol, Cyprus)
Natalie Panayiotou (GOC, Limassol, Cyprus)
Cleanthis Ioannides (GOC, Limassol, Cyprus)
Nikolaos Zamboglou (GOC, Limassol, Cyprus)

Date: 22/07/2022

Table of Contents

Executive summary

This deliverable presents the Journal papers that were published during the second year of the SOUNDPET project. Below, we provide a list of the published papers, including their title, the corresponding scientific journal and DOI.

	Title	Scientific Journal	DOI Accepted Date
1	MR relaxation properties of tissue-mimicking phantoms (Review)	*Ultrasonics*	10.1016/j.ultras.2021.106600 21/09/2021
2	MR relaxation times of agar-based tissue mimicking phantoms	*Journal of Applied Clinical Medical Physics*	10.1002/acm2.13533 29/12/ 2021
3	Robotic system for top to bottom MRgFUS therapy of multiple cancer types	*International Journal of Medical Robotics and Computer Assisted Surgery*	10.1002/rcs.2364 05/01/2022
4	Full coverage path planning algorithm for MRgFUS therapy	*International Journal of Medical Robotics and Computer Assisted Surgery*	10.1002/rcs.2389 06/03/2022
5	Ultrasonic attenuation of canine mammary tumours	*Ultrasonics*	10.1016/j.ultras.2022.106798 23/06/2022

MR relaxation properties of tissue-mimicking phantoms

Anastasia Antoniou, Christakis Damianou [*]

Department of Electrical Engineering, Computer Engineering, and Informatics, Cyprus University of Technology, Limassol, Cyprus

A B S T R A C T

High quality tissue-mimicking phantoms (TMPs) have a critical role in the preclinical testing of emerging modalities for diagnosis and therapy. TMPs capable of accurately mimicking real tissue in Magnetic Resonance guided Focused Ultrasound (MRgFUS) applications should be fabricated with precise T1 and T2 relaxation times. Given the current popularity of the MRgFUS technology, we herein performed a systematic review on the MR relaxation properties of different phantoms types. Polyacrylamide (PAA) and agar based phantoms were proven capable of accurately replicating critical thermal, acoustical, and MR relaxation properties of various body tissues. Although gelatin phantoms were also proven factional in this regard, they lack the capacity to withstand ablation temperatures, and thus, are only recommended for hyperthermia applications. Other gelling agents identified in the literature are Poly-vinyl alcohol (PVA), Polyvinyl Chloride (PVC), silicone, and TX-150/ TX-151; however, their efficacy in thermal studies is yet to be established. PAA gels are favorable in that they offer optical transparency enabling direct visualization of coagulative lesions. On the other hand, agar phantoms have lower preparation costs and were proven very promising for use with the MRgFUS technology, without the toxicity issues related to the preparation and storage of PAA materials. Remarkably, agar turned out to be the prominent modifier of the T2 relaxation time even for phantoms containing other types of gelling agents instead of agar. This review could be useful in manufacturing realistic MRgFUS phantoms while simultaneously indicating an opportunity for further research in the field with a particular focus on the MR behavior of agar-based TMPs.

1. Introduction

Tissue Mimicking Phantoms (TMPs) serve as a valuable tool in the process of evaluating diagnostic and therapeutic modalities both in the preclinical setting and clinical routine [1]. Gel phantoms enable ergonomic and cost-effective biomedical research simultaneously contributing to the minimization of animal testing, as well as quality assurance (QA) practices in medicine [1,2]. In the last decade, the increasing utilization of Magnetic Resonance guided Focused Ultrasound (MRgFUS) [3] has resulted in an increased need for high quality TMPs suitable for use with this emerging technology, thus accelerating its clinical adaption. Remarkably, the methods and tools for QA of FUS are still to be standardized. Thereby, gel phantoms with tissue-like behavior could serve as a handy tool in the preclinical validation of emerging applications and quality control of clinical systems while concurrently contributing to establish reliable QA standards in the field of MRgFUS.

FUS induces thermal and mechanical effects in tissue that were proven to be essential in many therapeutic applications [4].

Extracorporeal US can be precisely delivered into a millimeter-sized area of malignant tissue in a totally non-invasive manner [4]. Temperature elevations of up to 90 °C can be produced at the focal point within a few seconds of sonication, causing instant coagulative death of cells [5]. Hence, FUS has emerged as an alternative option to surgical interventions for several oncological applications [6]. The technology has also proven remarkably effective in neurological applications [6].

Thermal ablation with FUS is typically performed under US or Magnetic Resonance Imaging (MRI) guidance [6]. MRI guidance is superior in terms of imaging resolution and soft tissue contrast, thereby offering more accurate delineation of tumour margins [7]. Besides its excellent imaging capabilities, monitoring of the temperature changes during FUS heating is feasible through MR thermometry [8].

The contrast in MR images arises from variability in the proton density (ρ) and longitudinal (T1) and transverse T2 (and T2*) magnetic relaxation times of tissues [8]. Accordingly, temperature monitoring in the MRI setting is based on these temperature-sensitive parameters [8], especially for lipid-rich tissues [9]. In this regard, Waspe et al. [10]

assessed the feasibility of monitoring temperature changes during FUS by dynamic T2 mapping.

MR parameters have also been shown to greatly affect the contrast between normal soft tissue and FUS lesions. There is a limited number of preclinical animal studies reporting post-sonication relaxation times of FUS lesions [11–13]. *In vivo* experiments in rabbit tissues proved that the T1 and T2 values of thermal lesions depend greatly on the tissue type [11]. Similarly, lesions inflicted in *ex vivo* porcine tissue exhibited different MR appearance depending on the tissue type despite the use of similar acoustic parameters [12], thus confirming that the host tissue properties define the MR appearance of lesions. All inflicted lesions presented T2 values significantly higher than the surrounding untreated tissue and appeared hyperintense in T2-weighted images [12]. A further remarkable finding is that vacuolated and paste-like lesions were estimated to possess higher T2 values compared to thermal lesions [12]. A similar conclusion was reached by Kholmovski et al. [13], who performed radiofrequency ablation in 6 canines, with the acute results revealing higher T2* relaxation times within lesions in normal myocardium. In long-term examination, opposite results were obtained, with the lesions presenting a gradual decrease of the T2* value [13].

Regarding the longitudinal relaxation time T1, various studies [14–16] suggest a trend towards higher T1 values in FUS lesions compared to the surrounding normal tissues. In animal studies performed by Walker et al. [14], the ablated areas appeared hypointense in T1 images in the acute phase post-treatment. Notably, a clinical study that investigated the feasibility of transcranial MRgFUS to treat essential tremor reported T1 gradual shortening at the lesion site, typically beginning at 1-month post-treatment [16].

A tissue like thermal behavior is of paramount importance for phantoms intended for MRgFUS applications since the therapeutic result is evaluated via thermometry based feedback [17]. However, the previously reported data suggest that besides thermal properties, TMPs should also be able to replicate critical MR properties of biological tissues in order to be qualified for use with MRgFUS. So far, studies have predominantly examined the thermal and acoustical properties of FUS phantoms, whereas much less effort was devoted to the investigation of their MR properties [17,18]. At this point, it should be noted that phantom materials that are currently used for imaging purposes might also exhibit potential for use with ablation procedures. Thereby, state-of-the-art research in MR properties of gel phantoms intended for various applications, including those for medical applications and quality assessment purposes, was carried out. Herein, we briefly summarize the collected data, with special emphasis on the materials most widely used for phantom development and their MR relaxation properties.

2. Methodology

The PubMed database was mainly used since it includes a wide variety of sources in the specific field of biomedical sciences covering all time periods, with 7.1 million articles archived. A systematic search of the PubMed papers was carried out using specific vocabulary. The keywords {T1, MRI, US, phantom} were applied without any year range filter, thus not limiting the amount of data and resulted in a total of 608 results. Additional exclusion criteria were not applied, and all articles were considered to eliminate the possibility of missing articles of irrelevant titles which may actually include useful information. A scientific staff member with experience in therapeutic US and TMPs fabrication evaluated the results to ensure all criteria were applied properly and select the relevant articles for inclusion. A total of 39 articles were considered relevant. Supplementarily, another 5 articles were retrieved from Google Scholar searches of similar keywords.

The search results are organized in three sections. The first one briefly introduces the critical properties of phantoms intended for MRgFUS studies to facilitate the reader's understanding. Next, the included articles are classified into five main categories based on the phantom type (i.e., gelling agent used). Critical tissue mimicking properties and any interesting trend in MR properties of each category are listed. The rest of the paper briefly summarizes and discusses the search results and underlines opportunities for further research in the field that would possibly close gaps identified in existing studies. To the best of our knowledge, this is the first attempt to review the MR properties of TMPs.

3. Critical parameters of MRgFUS phantoms

Firstly, TMPs intended for FUS studies should possess similar acoustic behavior, with the speed of sound in the medium, characteristic acoustic impedance, and attenuation coefficient being the most significant properties to be emulated [17,19].

More importantly, the thermal characteristics of biological tissues need to be replicated by phantoms intended for thermal studies with FUS. The thermal profile of a TMP during FUS exposure is mostly governed by specific parameters, among which the most common are the specific heat capacity, thermal conductivity, and thermal diffusivity [17,19]. These parameters are particularly crucial in the process of assessing tissue necrosis during ablation under the guidance of MRI. In fact, since the therapeutic result is evaluated via thermometry based feedback, a tissue like thermal behavior is of paramount importance, whereas rigorous modeling of acoustic properties is not required in this regard.

Besides the thermal behavior of TMPs, MR parameters are also critical in determining their suitability for MRgFUS applications. As previously reported, both the contrast in MR images and temperature monitoring during high intensity FUS (HIFU) exposures are based on changes in the magnetic relaxation times T1 and T2 of tissues [8]. Most importantly, these parameters greatly affect the contrast between normal soft tissue and FUS lesions [11–13]. Accordingly, it is essential for MRgFUS phantoms to produce tissue-like MR signal in the process of evaluating therapeutic protocols.

4. Gel phantoms for evaluating diagnostic and therapeutic modalities

4.1. Agar gels

Agar probably constitutes the most widely used gelling agent for the construction of phantoms for multiple purposes, as confirmed by the current literature search. The widespread use of agar gels may be attributed to several factors, including their ease and low-cost fabrication, as well as their sufficient mechanical strength, which allows them to be formulated in different shapes and layered structures [20]. Another significant benefit of agar as a gelling agent relates to its high melting point of near 78 °C [21], which makes it ideal for thermal studies. Additional benefits of these gels will become apparent through the remainder of the paper.

The standard fabrication techniques of agar gels involve heating up degassed/deionized water in an appropriate buffer to about to 50 °C when the agar powder is slowly added, and then gradually heating the mixture to the melting point of agar, while it is continuously stirred to mitigate aggregation of agar in water [22,23]. The properties of agar gels can be easily and independently varied by adjusting the concentration of other ingredients added during the manufacturing process [20,22,24].

A wide variety of agar-based phantoms simulating thermal and acoustical properties of different types of soft tissue can be found in the literature [17,24–31]. Ultrasonic attenuation was found to vary with the addition of scattering particles such as silicon dioxide [24], magnesium [28], calcium [28], potassium [28], cellulose [29] and graphite [29] particles, as well as with the addition of glass beads [30]. Evaporated milk was proven a dominant absorber of acoustic energy [20]. Notably, glycerol has been proposed as a modifier of ultrasonic velocity [29].

Agar gels can also provide tissue-like signal (i.e., T1 and T2) in MRI [32], and thus, they were predominantly selected for validating new MRI protocols and imaging techniques [23,32–40]. MRI compatible phantoms simulating specific body parts such as brain [41], prostate [42], carotid [32], renal artery [43], and neonatal brain [44] exist in literature. Proper MRI imageability is also required for MRgFUS phantoms since accurate replication of MR relaxation properties is essential for producing tissue-like signal in MRI and more accurately testing and optimizing therapeutic protocols. In this regard, several agar-based TMPs were designed specifically for thermal ablation studies [22,25,27,45].

Literature data clearly indicates that the transverse relaxation time T2 predominantly depends on the agar concentration [23,33,34,46–49]. As described in more detail below, agar also served as the main T2 modifier in phantoms containing other types of gelling agents [46,48].

The addition of MR contrast agents enables better MR visibility while concurrently affecting the magnetic relaxation properties of phantoms [38, 39, 44, 50. Gadolinium-(Gd) based contrast agents were extensively used allowing adjustment of MR relaxation times, more significantly affecting the longitudinal value T1 [38,39,44]. T1 was also varied by incorporating different concentrations of paramagnetic ion salts such as Manganese(II) chloride (MnCl$_2$) [35], Nickel chloride (NiCl$_2$) [36], and Gadolinium(III) chloride (GdCl$_3$) [37]. Moreover, varying concentration of copper (Cu) ions enables changing the T1 values of agar gels [23]. It is important to note that addition of Cu ions requires the presence of another ingredient called Ethylenediaminetetraacetic acid tetrasodium hydrate (EDTA), which combines to Cu ions forming a stable free molecule; Cu-EDTA. Otherwise, Cu ions will be deposited on agar and loss their T1-modifying capacity [23]. In a representative study by D'Souza et al. [49], the concentration of agar (T2 modifier) and Cu-EDTA (T1 modifier) were properly selected, allowing the creation of phantoms simulating the magnetic relaxation properties of prostate and muscle tissue.

By using preservatives, such as thimerosal [49] and sodium azide (NaN$_3$) [31], bacterial invasion is prevented, thus extending the phantom lifetime. It is also noteworthy that several studies proposed the addition of animal hide gelatin in combination with agarose as a way to prevent the expulsion of an aqueous solution that may be produced in agar only gels [51].

Although agar-based phantoms were proven functional in a wide range of applications, they are accompanied by some limitations. Firstly, they have relatively low toughness and thus are easily fragile [1]. Also, they provide limited optical opacity, which prevents direct visualization of lesion formation in cases of thermal exposures [1]. Extensive results of prior research are summarized in Table 1. The referenced study, purpose of study, phantom recipe, and estimated relaxation times T1 and T2 are listed in this table.

4.2. Gelatin gels

Another category of phantoms that are easily fabricated and were proven factional is the gelatin-based phantoms [52–56]. Again, the gelation process involves solving gelatin powder in aqueous solutions while several soft tissues can be accurately mimicked by adding a proper concentration of other ingredients to the base recipe [52–56]. For instance, evaporated milk [52] and graphite powder [57] can be included to control the acoustic behavior of these gels, whereas the addition of ethanediol and polyethylene powder allows modification of electrical properties [58]. These phantoms can be manufactured in a low cost and easy way, with proper mechanical stiffness by incorporating cross-linkers during the phantom-making process [55].

Similar to agar phantoms, gelatin-based gels doped with an MRI contrast agent, most commonly a Gd-based agent, constitute a handy tool for MRI applications [56]. In cases where US compatibility is desired, acoustic modifiers should also be added in these phantoms. Farrer et al. [55] used porcine gelatin powders with three different

bloom values (125, 175, and 250) for the construction of MRgFUS phantoms of different mechanical stiffness, in which evaporated milk was the main attenuation component. The estimated T1 and T2 values varied for the different bloom types of gelatin [55]. An interesting trend was also observed by Hofstetter et al. [52], who developed a gelatin-based MRI/US compatible phantom containing psyllium husk as the ultrasonic scattering agent. Interestingly, both relaxation times were found to be decreasing with increasing concentration of psyllium husk. Again, evaporated milk was included replacing a percentage of the water component to enhance ultrasonic absorption [52].

Another typical material found in gelatin phantoms is oil [53,54]. These phantoms are commonly referred to as oil-in-gelatin phantoms and are mainly involved in elastography studies, in which the elastic modulus depends on the volume percentage of oil [54]. Remarkably, the oil concentration was shown to have a noticeable effect on the MR relaxation properties of oil-in-gelatin dispersions [53,54]. In a study by Madsen et al. [54], the use of safflower oil was proven suitable particularly for US elastography [54]; however, the resultant relaxation properties of phantoms differed considerably from those of soft tissue [54]. Advantageously, Yuan et al. [53] selected pure vegetable oil to develop an oil-in gelatin human thigh phantom intended for radio-frequency heating because its thermal and MR properties are comparable to that of human fat. In this category of phantoms, thimerosal served as the preservative component [54].

Typically, gelatin phantoms possess a relatively low mechanical strength, as well as a low melting temperature making them impractical for thermal regimes exceeding 50 °C [59]. These limitations can be fairly addressed with the addition of a bonding agent such as formaldehyde [60] or glutaraldehyde [61]. These chemicals act as cross-linkers of gelatin [54], thus increasing the stiffness and temperature tolerance during thermal exposures in gelatin phantoms [62]. In fact, the typical melting point of gelatin of about 32 °C [63] can be increased to more than 60 °C when using a cross-linking agent [62,63]. Though this technique has essential benefits, it may cause unfavorable changes in other critical parameters [55].

Phantoms composed of mixtures of agar and gelatin have emerged as alternative candidates for elastography [63] and MRI [51,62] applications. Employment of agar results in stiffer phantoms (i.e., higher Young's modulus) with increased geometrical stability while at the same time enabling the embedment of inclusions to gelatin gels [63]. To be more specific, a different dry-weight gelatin concentration between background and inclusions could result in over-time size changes of inclusions due to osmotic effects [63]. This phenomenon does not occur in the case of agar, and thus, a phantom of proper stability can be produced by incorporating different agar concentrations between background and inclusions [63]. It is also noteworthy that several studies proposed the addition of animal hide gelatin in combination with agarose as a way to prevent the expulsion of aqueous solution which may be produced in agar only gels [51].

Cu ions have the capacity to lower T1 values of agar/gelatin phantoms [51,63]. They are usually added in the form of ionic salts such as Cupric chloride (CuCl$_2$). As previously described for the agar gels, addition of EDTA is required for preventing the arrestment of ions to gelatin molecules [51,63]. A representative example is a study by Madsen et al. [63], who developed an agar/gelatin elastography phantom consisting of agar as the stiffness agent, Cu-EDTA as the T1 modifier, formaldehyde as the cross-linking agent, and glass beads as the attenuation and backscatter component. Sodium chloride (NaCl) was also included to offer tissue-like NMR coil loading. Alternatively, Blechinger et al. [62] selected glycerol instead of paramagnetic ions to attain the desired T1 in an animal hide gel/agar phantom. Variations in glycerol concentration significantly varied T1 values, whereas T2 was minimally affected. In fact, T2 was strongly affected by the animal hide gel concentration [62], confirming that the relaxation times can be varied independently. In line with the previously reported data, the resultant phantom showed durable stability, without any fluid

Table 1

T1 and T2 relaxation times of agar-based phantoms, along with the MR technique used for relaxometry mapping and the temperature at which measurements were conducted (if provided by the relevant study). IR = Inversion Recovery; ME = Multi-Echo; SE = Spin-Echo; FSE = Fast SE; T2-w = T2-weighted; T1-w = T1-weighted; TSE = Turbo SE; CPMG = Carr-Purcell-Meiboom-Gill; TIRSE = Turbo Inversion Recovery SE; SR = Saturation Recovery; DESPOT = Driven Equilibrium Single Pulse Observation of T1/T2; UTE-MRF = Ultrashort Echo time MR fingerprinting.

Agar-based phantoms				
Recipe	**T1 rel. time (ms)**	**T2 rel. time (ms)**	**Purpose**	**Ref.**
3% agarose in water 3 % fibrous cellulose 7% glycerol 0.05 % methylene blue	1679 ± 15 3 T MR scanner *IR* seq. TI: 50–5000 ms	41 ± 1 3 T MR scanner *ME SE* seq. -	Tumour mimic for MRgFUS studies	[45]
0.5 % agar in water 5–30 µl gadopentetate acid meglumine	735–1667 3 T MR scanner *IR SE* seq. TI: 100–2100 ms	236–311 3 T MR scanner *ME SE* seq. TE: 8–56 ms	Phantom for testing fast T1 mapping method	[38]
2 % w/v agar 4 % w/v wood powder	844 1.5 T MR scanner *T1-w IR FSE* seq. TI: 200–1600 ms	66 1.5 T MR scanner *T2-w FSE* seq. TE: 23–101 ms	TMP for MRgFUS applications	[22]
0.6 % agar solution 0–0.15 mM $MnCl_2$	700–1800 3 T MR scanner *2D IR TSE* seq. TI: 30–2000 ms	–	Brain MRI phantom	[41]
4% agarose gel	1207 ± 168 1.5 T MR scanner *IR* seq.	66 ± 9 1.5 T MR scanner *ME* seq.	CT/MRI prostate phantom	[42]
2 % w/v agar 25% v/v evaporated milk 1.2% w/v silica	852 1.5 T MR scanner *IR SE* seq. TIs: 66–750 ms	66 1.5 T MR scanner *T2-w FSE* seq. ETs: 18–99 ms	Brain TMP for US surgery	[25]
1 L of distilled water 35 g high gel strength agar 80 mL glycerol. 30 g cellulose particles (size: 50 µm) 20 mL of formaldehyde (2 wt%)	1090 ± 140 (0.5 T) 1150 ± 162 (1.5 T)	42 ± 3 (0.5 T) 50 ± 6 (1.5 T)	Carotid Phantom for MRI applications	[32]
82.97 wt% distilled water 3.0 wt% agar 11.21 wt% glycerol 0.53 wt% silicon carbide (400 grain) 0.88 wt% aluminum oxide (0.3 µm) 0.94 wt% aluminum oxide (3 µm) 0.46 wt% benzalkoniumchloride	1504 ± 10 3 T MR scanner *IR* seq. -	40.0 ± 0.4 3 T MR scanner *CPMG* SE seq. TEs: 10–80 ms	Multimodality renal artery phantom	[43]
0.3 % w/v agarose + 0.03 mM Gd-DTPA 0.6 % w/v agarose + 0.10 mM Gd-DTPA	1654 ± 9 1134 ± 7 1.5 T MR scanner *2D TIRSE* seq. TIs: 25–3970 ms 19 °C	376 ± 4 200 ± 7 1.5 T MR scanner *2D CPMG ME SE* seq. TEs: 20 –640 ms 19 °C	TMP simulating T1 and T2 of neonatal brain	[44]
0.3–4 wt% agarose 0.5–8 mM Ni^{2+}	180–1400 10.7 MHz (0.25 T) MR analyzer *SR* seq.	34–200 10.7 MHz (0.25 T) MR analyzer *SE* seq.	TMP for MR imaging	[34]
agarose gel 0.0–2.0 mM gadolinium 0, 10, 20, 100% peanut oil (content ratio)	$50 < T_1 < 350$ 3 T MR scanner *DESPOT* seq	–	Method for fast MR mapping	[39]
agarose & varying concentration of $MnCl_2$	397 ($\pm$12)–759 ($\pm$19) 3 T MR scanner *UTE-MRF* seq.	37 ($\pm$3)–85 ($\pm$7) 3 T MR scanner *UTE-MRF* seq.	Evaluation of methods for MR parameter mapping	[35–37]
agarose & varying concentration of $NiCl_2$	200 < T1 < 1500 1.5 T MR scanner *IR SE* seq. TI: 50–3000 ms	41–80 (1.5 T) 1.5 T MR scanner *ME SE* seq.		
agarose & varying concentration of GdCl3	200–1600 (1.5/3 T) *2D IR single echo SE* seq. TI: 50–3800 ms or *Look-Locker* seq.	-		
2 % w/v agar 2 % w/v silicon dioxide 40 % v/v evaporated milk	776 1.5 T MR scanner *IR SE* seq. TIs: 50 –800 ms	66 1.5 T MR scanner *T2-w FSE* seq. TEs: 10.8–150.8 ms	MRI bone phantom for thermal exposures	[27]
0.5–4.0 % w/v agarose	1000 ($\pm$92) − 1481 ($\pm$151) 5 MHz NMR spectrometer	23 ($\pm$9) − 240 ($\pm$15) 5 MHz NMR spectrometer	TMP for NMR imaging	[23]

Table 1 (*continued*)

Agar-based phantoms

Recipe	T1 rel. time (ms)	T2 rel. time (ms)	Purpose	Ref.
	1390 ($\pm$84) − 2743 ($\pm$71) 60 MHz NMR spectrometer *IR* seq.	27 ($\pm$3) − 278 ($\pm$43) 60 MHz NMR spectrometer *CPMG SE* seq.		
1.3% w/v agar 0–26.7 % w/v granulated sugar	921 ($\pm$16) − 2239 ($\pm$55) 3 T MR scanner *IR* seq.	68 $\pm$ 2–73 $\pm$ 3 3 T MR scanner *ME* seq.	Evaluation of methods for breast diffusion-weighted MRI	[40]
0.24–2.38 % Agarose 0.18–5.55 mM NiCl$_2$	256–1870 1.4 T Minispec relaxometer 22 °C 250–1872 3 T MR scanner *IR* seq. 21 $\pm$ 2 °C	50–288 1.4 T Minispec relaxometer 22 °C 42–231 3 T MR scanner *SE* seq. 21 $\pm$ 2 °C	Phantom for global T1 mapping quality assurance	[33]
Prostate 50 % v/v agarose solution (2% dry w/v) 50 % v/v condensed milk 7.9 % v/v n-propyl alcohol (per agarose) 0.06 w/v % CuCl2 salt (per total volume) 0.103 w/v % Ethylenediamine tetra acetic acid (EDTA) (per total volume) 1 g/l of 45–53 μm diameter glass beads thimerosal	937 $\pm$ 13 40 MHz Minispec relaxometer *IR* seq. 21 °C	88 $\pm$ 3.8 40 MHz Minispec relaxometer *CPMG SE* seq. 21 °C	TMP multi-imaging modality	[49]
Muscle 50 % v/v agarose solution (6% dry w/v) 50 % v/v condensed milk 7.9 % v/v n-propyl alcohol (per agarose) 0.048 % w/v CuCl2 salt (per total volume) 0.082 % w/v EDTA (per total volume) 5 % w/v microscopic glass beads thimerosal	686 $\pm$ 9 40 MHz Minispec relaxometer *IR* sequence 21 °C	36.7 $\pm$ 1.9 40 MHz Minispec relaxometer *CPMG SE* seq. 21 °C		

extrusions, most probably due to the addition of formaldehyde and n-propanol offering antibacterial activity, also given the agar-enhanced rigidity. The proposed gelatin-based phantoms and their T1 and T2 relaxation times are summarized in Table 2.

4.3. Polyacrylamide (PAA) gels

Another candidate material for fabrication of stable TMPs is PAA [50,64–69]. PAA is probably the most popular material for fabricating heat-responsive phantoms, primarily due to its high melting point [64]. It is also of paramount importance that these phantoms offer optical transparency [65], enabling visual confirmation of coagulation in the phantoms. Common catalysts added for activating PPA polymerization are the ammonium persulfate (APS) and tetramethylethylenediamine (TEMED) [50,68–70].

Thermoresponsive proteins such as Bovine serum albumin (BSA) were found to enhance acoustic absorption in PAA phantoms [66]. When these proteins are heated at lethal temperatures undergo irreversible changes in MR values and become opaque, thus enabling discrimination of the heated area both visually and via changes in MRI signal intensity [66,67]. Specifically, white-opaque lesions are formed when BSA is coagulated at temperatures between 60 °C and 70 °C. Additional ingredients such as evaporated milk, corn syrup [71], glass beads [72], and silica particles [68] can be used to adjust the acoustical properties of PAA-BSA phantoms in the range of human tissues.

Bazrafshan et al. [70] developed an MR visible liver mimicking phantom intended specifically for Laser interstitial thermal therapy (LITT) applications. The PAA gel was doped with BSA protein for visualization of thermal effects. Poly-vinyl alcohol (PVA) microspheres were also incorporated to enhance photon scattering. The addition of two different MR contrast agents; Magnevist and Lumirem, allowed modification of the T1 and T2 relaxation times, respectively [70]. NaN$_3$ was used to prevent microbial growth [70]. Notably, a PAA-based phantom for LITT applications may also contain bovine hemoglobin as a photon absorber [50].

TMPs containing thermochromic ink that exhibits progressive color change upon heating can also be used for visual monitoring of thermal ablation [68]. Eranki et al. [68] developed a PAA-based thermochromic TMP intended for HIFU applications. Both BSA protein and a thermochromic ink that under heating changes color from white to magenta were added. Proper concentration of these inclusions allowed visualization of well-defined regions of permanent color change upon heating, which correlated well with MRI thermometry data and regions of hypointensity on T2-weighted images [68]. Similar to agar-based phantoms, silicon dioxide served as the attenuation component [68]. In this category of phantoms, NaCl is usually included to adjust electrical conductivity [68,70]; however, the relaxation values of PAA gels were found independent of the NaCl concentration [73].

Egg-white is another heat-responsive material that was proposed for irradiation studies with FUS as a less expensive alternative to BSA [69]. Careful selection of egg white concentration is critical to maintaining adequate optical clarity in phantoms. A suitable egg white (my mass) concentration of 10 to 40% was proposed by Takegami et al. [69] for sufficient visualization during HIFU exposures. Although the acoustic properties of the proposed phantom were found to be similar to those of soft tissues, MR relaxation properties were not investigated.

Toxic materials are typically employed complicating the preparation of PAA gels and generating safety concerns [74]. Specifically, the procedure involves polymerization of acrylamide, a toxic monomer, which requires proper care and may be hazardous when PAA-gels are not stored under proper environmental conditions [74]. Another limitation relates to the use of BSA or egg white, which undergo permanent changes when coagulated, thus making the phantoms unsuitable for repeated use. The relevant studies are listed in Table 3.

4.4. Carrageenan gels

Carrageenan constitutes a common additive that can be used as a bonding material for phantom fabrication [48]. Although, as a polysaccharide, it generally presents similar characteristics with agar,

Table 2

T1 and T2 relaxation times of gelatin-based phantoms, along with the technique used for relaxometry mapping and the temperature at which measurements were conducted (if provided by the relevant study). T2-w = T2-weighted; T1-w = T1-weighted; SPGR = Spoiled gradient recalled echo; IR = Inversion Recovery; CPMG = Carr-Purcell-Meiboom-Gill; STIR = Short T1 Inversion Recovery; ME = Multi-Echo; GRE = Gradient Recalled Echo; TSE = Turbo Spin Echo; MPME = Multi-Pathway Multi-Echo.

Gelatin-based phantoms				
Recipe	**T1 rel. time (ms)**	**T2 rel. time (ms)**	**Purpose**	**Ref.**
Tumour	1034.7	T2* 113.1	TMP for RF heating and MRI thermal monitoring	[53]
225 bloom gelatin in saline water				
5 % oil-in-gelatin dispersion				
Muscle	1084.9	64.5		
225 bloom gelatin in saline water	1.5 T MR scanner	1.5 T MR scanner		
10 % oil-in-gelatin dispersion	T1-w *SPGR* seq.	T2*-w *SPGR* seq.		
	TR: 50–3000	TE: 7.5–160.7		
13.3 wt% gelatin	560	230	Tissue-Mimicking Heterogeneous Elastography Phantoms	[54]
1 g/L thimerosal	**or**	**or**		
0.35 g/L formaldehyde	1610	416		
50 % safflower oil				
4 g/L glass beads				
or	40 MHz Bruker relaxometer	40 MHz Bruker relaxometer		
20 g/L glass beads	*IR* seq.	*CPMG* seq.		
	22 °C	22 °C		
11.1 % w/v porcine gelatin powders	970 ± 3 (125 bloom)	T2* 58 ± 7 (125 bloom)	TMPs for use with MRgFUS	[55]
(125/ 175/ 250 bloom)	853 ± 3 (175 bloom)	55 ± 7 (175 bloom)		
50 % v/v water–50 % v/v evaporated milk	1093 ± 5 (250 bloom)	67 ± 12 (250 bloom)		
vyse defoamer solution	3 T MR scanner	3 T MR scanner		
	STIR seq.	*ME GRE* seq.		
	TI: 50–2500 ms	TE: 2.83–80 ms		
50 vol% water–50 vol% evaporated milk	974–1038	T2: 97–108	Phantom for US and MRI imaging	[52]
111 g/L 250-bloom gelatin powder	3 T MR scanner	3 T MR scanner		
3.33 g/L DOWACIL 75	2D *IR TSE* seq.	2D *TSE* seq.		
0.5–16 g/L psyllium Husk	TI: 50–2500 ms	TE: 13.1–262 ms		
	21 °C	21 °C		
		T2*: 49–89		
		3D *GRE* seq.		
		TE: 3.96–62.92 ms		
		21 °C		
0.17 vol% defoamergelatin & varying concentration of gadolinium	150 < T1 < 5003 T MR scanner	100 < T2 < 2203 T MR scanner	New method to quantitatively map MR parameters	[56]
	MPME seq.	*MPME* seq.		
Gelatin/ Agar phantoms				
1.11–3.64 wt% agar	369–498	28–63	Heterogeneous elastography phantoms	[63]
3.60–5.70 wt% 200 bloom gelatin				
0.113–0.116 wt% CuCl₂-2H₂0				
0.33–0.34 wt% EDTA tetra-Na hydrate				
0.77–0.80 wt% NaCl				
0.24–0.33 wt% formaldehyde				
1.45–1.50 wt% German plus	60 MHz Bruker relaxometer	60 MHz Bruker relaxometer		
0–5.6 wt% glass bead	*IR* seq.	*CPMG* seq.		
	22 °C	22 °C		
Thalamus	T1 of water in phantom:	T2 of water in phantom:	Anthropomorphic MRS head phantom	[51]
2.3 wt% agar	1065 ± 30	98.06 ± 0.20		
7.5 wt% gelatin				
0.028 wt% CuCl2				
0.13 wt% EDTA-tetra Na				
0.1 wt% NaCl				
0.24 wt% HCHO				
0.1 wt% thimerosal				
Tumour	1215 ± 1	149.6 ± 0.2		
2 wt% agar				
7.5 wt% gelatin				
0.0223 wt% CuCl2				
0.101 wt% EDTA-tetra Na				
0.1 wt% NaCl				
0.24 wt% formaldehyde	1.9 T Bruker spectrometer	1.9 T Bruker spectrometer		
0.1 wt% thimerosal	*IR* seq.	*CPMG* sequence		
	22 °C	22 °C		
0–50 vol% (of liquid components) glycerol	200 < T1 < 1100	50 < T2 < 80	TMPs for MRI phantoms	[62]
40 vol% animal hide gel–60 vol% agar				
8.3 vol% n-propyl alcohol	10 MHz spectrometer	10 MHz spectrometer		
0.0065 mass ratio of p-methylbenzoic acid /animal hide gel	*IR* seq.	*CPMG SE* seq.		
	22 °C	22 °C		
0.017 mass ratio of formaldehyde				

Table 3

T1 and T2 relaxation times of PAA-based phantoms, along with the technique used for relaxometry mapping and the temperature at which measurements were conducted (if provided by the relevant study). ME = Multi-Echo; TSE = Turbo Spin Echo; IRTF = Inversion Recovery Turbo Flash; MCSE = Multi-Contrast Spin Echo.

PAA-based phantoms				
Recipe	T1 rel. time (ms)	T2 rel. time (ms)	Purpose	Ref.
70.0 % v/v deionized water	–	225 ± 14	TMP for HIFU applications	[68]
7.0 % v/v 40% acrylamide/bis-acrylamide		1.5 T MR scanner		
5.0 % v/v Magenta (thermochromic ink)		152 ± 8		
3.0 % w/v BSA		3 T MR scanner		
1.1% w/v Silicon dioxide		*2D ME TSE* seq.		
0.9 % w/v NaCl		TE: 50–450 ms		
0.15 % v/v APS				
0.15 % v/v TEMED				
37.9 vol% distilled water	$275 < T1 < 500$ for 25–75°C	$46 < T2 < 52$ for 25–75 °C	Liver-mimicking MRI phantom	[70]
30 vol% Rotiphorese® acrylamide				
16 wt% BSA				
10 vol% PVA microsphere				
0.04 vol% Magnevist®				
3.3 vol% Lumirem®	1.5 T MR scanner	1.5 T MR scanner		
0.08 vol% TEMED	*IRTF* seq.	*MCSE* seq.		
1.75 vol% APS	TI: 100–2500 ms	TE: 10.6–339.2 ms		
0.9 wt% NaCl				
0.03 wt% NaN3				
60 vol% distilled water	246.6–597.2	40.8–67.1	A liver mimicking MRI phantom for thermal therapy studies	[50]
30 vol% Rotiphorese® acrylamide	for 25–75 °C	for 25–75 °C		
5 vol% PVA microsphere				
3.92 ± 0.42 vol% bovine hemoglobin				
0.098 ± 0.023 vol% Magnevist®	1.5 T MR scanner	1.5 T MR scanner		
2.980 ± 0.067 vol% Lumirem®	*IRTF* seq.	*MCSE* seq.		
0.084 vol% TEMED	TI: 120–1000 ms	TE: 10.6–339.2 ms		
1.5 vol% APS				
0.9 wt% NaCl				
0.03 wt% NaN3				

carrageenan gels were proven less fragile than agar-based gels [48]. They are elastic and can be easily shaped to form strong phantoms of any configuration without the addition of other reinforcing materials [48]. It should though be noted that carrageenan phantoms are not suitable for HIFU exposures since they can only withstand temperatures of up to about 60 °C before liquefaction [48].

The addition of carrageenan in agar gels seems to solve the problem of low toughness in agar-only gels [2,46–48]. Yoshida et al. [48] developed an MRI phantom using carrageenan as a solidifier and agarose as the T2-modifying component. T1 values were adjusted by addition of proper GdCl$_3$ concentration. Furthermore, inclusion of NaCl affected both T1 and T2 values, with T1 being affected in a slightly larger degree [48]. Accordingly, in a study by Yoshimura et al. [46], both relaxation times T1 and T2 were found to be increasing, respectively, upon increasing concentration of GdCl$_3$ and agarose at a fixed concentration of carrageenan. Again, carrageenan served as the solidifying agent allowing the creation of a robust phantom, while agarose served as the T2 modifier [46]. Neumann et al. [47] have proposed a carrageenan phantom mimicking thorax tissue, in which T1 was adjusted by adding proper amount of gadoterate meglumine. Again, NaN$_3$ may be added in this phantom type acting as an antiseptic [47,48]. The proposed carrageenan phantoms are summarized in Table 4.

4.5. Other gelling agents

Other former candidates that were identified include PVA [75–77], Polyvinyl Chloride (PVC) [78–80], silicone [81,82] and TX-150/151 [83,84]. These materials served as gelling agents in phantoms intended for imaging applications. Detailed results can be found in Table 5.

PVA is a water-soluble rubbery synthetic polymer with which cryogels can be formed through a repeated freeze-thaw method [75–77]. PVA cryogels doped with Gd-based contrast agents were proposed for MR imaging studies [75]. It should be noted that different types of contrast agents can be used to offer compatibility with multiple imaging

modalities. For instance, a PVA-based brain phantom containing Barium sulfate (BaSO$_4$) as CT contrast agent, Copper sulfate (CuSO$_4$) as MR contrast agent, and talcum as US contrast agent was recommended by Chen et al. [76] for multimodal imaging. In such cases, the MR contrast agent acts as the main relaxation time modifier. A notable trend observed by Surry et al. [77] is that increasing number of freeze–thaw cycles during phantom preparation results in lower T1 relaxation times.

Another common synthetic chemical polymer is PVC. Soft PVC phantoms are relatively low-cost, with long-term easy storage [79]. The fabrication process involves heating up a mixture of PVC powder and softener until polymerization under constant stirring [78–80]. PVC gels mimicking soft tissue are useful in MR and US elasticity imaging [79]. Chatelin et al. [79] found that their MR relaxation properties are slightly influenced by the variation of the mass ratio PVC /plasticizer. In this study, cellulose served as a source of echogenicity without consistent influence on relaxation values [79]. Another study [80] confirmed that the MR properties of PVC gels can be regulated to mimic different soft tissues by adjusting the ratio of the softener to polymer [80]. Remarkably, inclusion of glass beads moderately lowered T2. Mineral oil was also incorporated to facilitate needle insertion applications but did not produce any apparent effect on T1 or T2 [80].

More recently, a polysaccharide material called TX-150 has been introduced as a candidate gelling agent for the construction of water-based TMPs for MRI applications [83,84]. Groch et al. [84] prepared a lesion phantom for MRI, in which increasing weight % concentration of TX-150 in degassed water shortened both relaxation times. This study suggests that T1 and T2 can be altered independently by incorporating metal phthalocyanines and 2-2-diphenyl-1 picrylhydrazyl, respectively [84]. A modified form of this polysaccharide; TX-151 was used in the development of an MRI compatible breast phantom by Mazzara et al. [83]. The amount of gelling agent had a weak influence on relaxation times. Aluminum powder served as the dielectric component having insignificant effect on T1 values. On the other hand, T2 was significantly shortened upon addition of aluminum and largely affected by varying

Table 4

T1 and T2 relaxation times of carrageenan-based phantoms, along with the technique used for relaxometry mapping and the temperature at which measurements were conducted (if provided by the relevant study). SR = Saturation Recovery; SE = Spin-Echo; T2-w = T2-weighted; T1-w = T1-weighted; IR = Inversion Recovery; TSE = Turbo Spin Echo.

Recipe	T1 rel. time (ms)	T2 rel. time (ms)	Purpose	Ref.
Carrageenan phantom				
5 wt% carrageenan 0.2 mM $MnCL_2$ 0.19 wt% NaCl 0.1 wt% NaN_3	429 (1.5 T)	84.9 (1.5 T)	MRI phantom	[88]
Carrageenan/ Agarose phantoms				
3 % carrageenan in distilled water	$100 < T1 < 2100$	$20 < T2 < 420$	Phantom compatible for MRI and hyperthermia	[48]
0–1.6 % agarose 0–140 µmol/ kg $GdCl_3$ 0–0.7 % NaCl 0.03 % NaN3	1.5 T MR scanner *SR* seq. TR: 140–16 474 ms 25 ± 1 °C	1.5 T MR scanner *SE* seq. TE: 15–300 ms 25 ± 1 °C		
3 wt% carrageenan in distilled water 0–1.6 wt% agarose 0–140 µmol/ kg $GdCl_3$ 0.03 wt% NaN_3	202–1904 1.5 T MR scanner *SR* seq. TR: 140–16 474 ms 25 ± 1 °C	38–423 1.5 T MR scanner *SE* seq. TE: 15–300 ms 25 ± 1 °C	Tissue mimicking MRI phantom	[46]
3 % carrageenan in distilled water	790 ± 28	65 ± 1	MR/ CT liver phantom	[47]
1.3 % agarose 2.37 ppm gadoterate meglumine 20 mM Na^+	3 T MR scanner *T1-w IR TSE* seq. TI: 250–5000 ms	3 T MR scanner *T2-w TSE* seq. TE: 15–240 ms		

aluminum (Al) concentration [83]. The relaxation time T1 was found to be decreasing with increasing Gd-DTPA concentration. Authors concluded that variation of these additives allows the creation of phantoms with a wide range of tissue-comparable MR relaxation times [83].

5. Discussion

Due to the increasing popularity of the MRgFUS technology, there is a critical need for TMPs that can replicate all the critical characteristics of human tissues, including acoustical, thermal, and MR properties. So far, TMPs have been widely characterized in terms of thermal and acoustical properties; however, more limited data is available about their MR properties. Thereby, this study aimed to review the MR relaxation properties of different phantom types through a systematic search of the literature. Although various physical properties of the referenced phantoms were discussed through the article, particular focus was placed on their T1 and T2 relaxation values.

In this article, the several phantoms previously proposed for a wide range of applications were briefly reviewed by category of gelling agent. However, the included studies could also be classified according to the intended application of the proposed phantom. Some studies were designed to investigate the physical parameters of phantoms intended

Table 5

T1 and T2 relaxation times of other tissue-mimicking materials, along with the technique used for relaxometry mapping and the temperature at which measurements were conducted (if provided by the relevant study). ME = Multi-Echo; FSE = Fast Spin Echo; IR = Inversion Recovery; T1-w = T1-weighted; T2-w = T2-weighted, GE = Gradient Echo; TSE = Turbo SE.

Recipe	T1 rel. time (ms)	T2 rel. time (ms)	Purpose	Ref.
PVA phantoms				
10 % PVA cryogel, 90 % water	1317 ± 23 106 ± 16	T2: 98 ± 8 T2*: 191 ± 36 T2: 122 ± 30 T2* 4.5 ± 0.56	MRI phantom	[75]
10 % PVA cryogel 50 µl/ml gadolinium solution	3 T MR scanner *3D fast-field ME* seq. TI: 20–2000 ms	3 T MR scanner T2*: *3D fast-field ME* seq. T2: *TSE* seq.		
10 wt% PVA in water solution 1–4 freeze–thaw cycles	718–1034 1.5 T MR scanner *2D FSE-IR* seq. TI: 50–3200 ms	108–175 1.5 T MR scanner *2D FSE* seq. TE: 15–195 ms	TMP for MR and US imaging	[77]
6 % PVA 1 freeze–thaw cycle 2 % BaSO4 0.025 % CuSO4	1004 –1213	163–182	Brain phantom for multimodal imaging	[76]
1 % talcum **or** 4 % PVA with 3 FTCs	1900–2600 3 T MR scanner *T1-w SE* seq.	1100–1665 3 T MR scanner *T2-w GE* seq.		
PVC phantoms				
12.3×10^{-2} g/mL PVC powder/ softener	206.81 ± 17.50 (3 T)	20.22 ± 5.74 (3 T)	Multi-purpose breast TMP	[78]
mass ratio PVC /plasticizer: 40–70%. 0.6, 0.8, and 1% concentrated cellulose	258–223 1.5 T MR scanner *TSE* seq. TI: 23–2,970 ms	50–44 1.5 T MR scanner *SE* seq. TE: 3.5–200 ms	TMP for MR and US elastography	[79]
0–1 ratio of softener to PVC polymer, 0/5 % mass fraction of mineral oil 0/1 % mass fraction of Glass beads	426.3–450.2 7 T RF volume coil *SE* seq. TI: 50–2500 ms	21.5–28.4 7 T RF volume coil *SE* seq. TE: 11–80 ms	TMP for multimodal imaging	[80]
Silicone phantoms				
–	410–765 (1.4 T)	50–165 (1.4 T)	Multimodality imaging Phantom	[81]
–	1002 ± 8 3 T MR scanner *Look-Locker IR* seq. TI: 30–4000 ms	58 ± 1 3 T MR scanner *ME SE* seq. TE: 40–400 ms	MR compatible cardiac left ventricle model	[82]
TX-150/ TX-151 phantoms				
7.00 wt% TX-151 polysaccharide material 83.50 wt% water 0.303 wt% NaCl 9.20 wt% Al powder 0.0–0.8 mM Gd-DTPA	174 (±10) – 1405 (±59) 1 T MR scanner 447 (±15) – 2949 (±213) 1.5 T MR scanner	30.4 (±0.2) – 36.3 (±0.1) 1 T MR scanner 19.6 (±0.1) – 24.8 (±0.6) 1.5 T MR scanner	Tissue mimicking MRI phantom	[83]

Table 5 (*continued*)

Recipe	T1 rel. time (ms)	T2 rel. time (ms)	Purpose	Ref.
0.08 mM GdDTPA 41.75 g water 0.1515 g NaCl g TX-151	746 ± 13–803 ± 28 (1 T) 1523 ± 147–1567 ± 77	25.4 ± 0.1–162.4 ± 10.2 (1 T) 18.8 ± 0.0–72.8 ± 3.2		
0–14.2 wt% Al	(1.5 T) *SE* seq. TR: 50–3000 ms 18 °C	(1.5 T) *SE* seq. TE: 20–160 ms 18 °C		
3–18 wt% TX-150 in degassed water	586 ± 30–2211 ± 37 20.9 MHz (0.5 T) NMR pulsed spectrometer *IR* seq. 20 °C	57–287 0.5 T MR scanner *SE* seq. 20 °C	Lesion phantom for MRI	[84]

specifically for thermal therapy studies, whereas the vast majority of included articles have proposed TMPs for imaging or QA purposes.

As confirmed by the search results, agar is probably the most common gelling agent for widespread applications. In fact, the majority of identified studies reporting MR properties of phantoms (~43%) involve the use of agar-based gels [22,23,25,32–45,49]. Agar has been quite extensively used as a gelling agent in FUS phantoms simulating different soft tissues, with additional materials added to adjust their thermal and acoustical properties [17,25–27]. In this regard, critical properties that have been sufficiently investigated include the speed of sound, acoustic attenuation, acoustic impedance, thermal diffusivity, specific heat capacity, and thermal conductivity [17,22,25]. In addition, their tissue-like MR signal makes them the material of choice for validating new MRI protocols and imaging techniques [23,32–40]. In such cases, modifiers of acoustic properties such as glycerol [32,43], cellulose particles [32], milk [49], and glass beads [49], are also added and adjusted to provide tissue-like US visibility.

Regarding thermal studies, PAA [50,68], agar [17,25–27], and gelatin [53,55] constitute the preferable gelling agents, each one having its own benefits and limitations. The ability of all three to accurately simulate physical properties of various biological tissues upon addition of proper concentration of inclusions has been demonstrated [1,2]. Both agar and PAA materials are characterized by temperature tolerance sufficiently high to maintain their physical and mechanical properties during HIFU exposures [21,64]. On the other hand, gelatin phantoms lack the capacity to withstand ablation temperatures. Their low melting temperature makes them unsuitable for thermal studies in which temperatures exceed 50 °C, and thus, are only recommended for hyperthermia applications [59].

Upon proper use and storage, gelatin gels can maintain long-term stability; however, they generally possess relatively low mechanical strength, which is strongly dependent on temperature variations [52]. Although their insufficient mechanical stability and temperature tolerance can be improved with the addition of a bonding agent such as formaldehyde [60] and glutaraldehyde [61], this may negatively affect their physical properties. Likewise, agar has been employed in gelatin phantoms to provide geometrical stability and allow the creation of inclusions without undesirable osmotic phenomena [63]. Thereby, the synergy of agar and gelatin seems to provide essential benefits related to long term stability and increased shelf life [63].

Except from being tissue equivalent and temperature resistant, phantoms intended for thermal ablation studies should ideally offer visualization of the coagulative regions, thus facilitating evaluation of therapeutic protocols. Visual capacity is also of great importance for visual assessment of the motion accuracy in robotic applications

[85,86]. Therefore, the optical transparency of PAA gels makes them favorable over agar gels [65]. However, synthesis of PAA gels is generally considered more complicated since it requires special care due to the use neurotoxic ingredients [74].

On the other hand, agar phantoms are easily prepared and stored, cost-effective, harmless, and with durable stability [2,22,23]. At this point, it should be noted that carrageenan can be used as a mechanical stabilizer in agar gels, enabling even more robust anatomical models [46,48]. It should though be pointed out that carrageenan cannot withstand ablation temperatures, and thus, it is unsuitable for HIFU therapies [48].

Other mimicking materials identified in the literature are the PVA [75–77], PVC [78–80], silicone [81,82], and TX-150/TX-151 gels [83,84]. Although various studies report some very promising results, the physical properties of these materials have not been sufficiently investigated, and their efficacy in thermal studies is yet to be established. This would of course require further evaluation of those characteristics critical for thermal applications, and particularly MRgFUS. In addition, proper gelation and solidification of such materials typically require multiple steps [75–77] leading to more complicated fabrication processes and sometimes to increased costs. Regarding TX-150, its gelation parameters are not well defined, thus causing difficulties in the fabrication process [83]. Moreover, TX-150 gels normally undergo bacterial degradation in just a few days. It is though notable that the addition of metal phthalocyanines was shown to create more stable and durable phantoms [84].

Potential modifiers of MR relaxation times become apparent through the collected data. T2 relaxation time was predominantly tailored by varying the gelling agent concentration. In fact, agarose served as the predominant T2 modifier in all the proposed agar-based phantoms [23,33,34,46–48], as well in phantoms containing other types of gelling agents [46–48]. Varying animal hide gel concentration also provides T2-modifying capacity [62], whereas both T1 and T2 of gelatin phantoms were found to vary for different types of gelatin [55]. This does not imply in the case of TX-151 gels, for which the amount of gelling agent seems to cause insignificant influence on relaxation times [83]. Regarding synthetic polymers, the MR properties of PVC gels can be adjusted to mimic different soft tissues by adjusting the ratio of the softener to polymer [80], whereas for PVA phantoms, smaller T1 values were observed with increasing number of freeze–thaw cycles [77].

Ingredients added as modifiers of acoustical properties also have a significant effect on the MR behavior of TMPs. Firstly, inclusion of glass beads was proven to slightly lower T2 of PVC phantoms [80]. A similar trend was reported in a study by Huber et al. [87], wherein the inclusion of glass beads lowered both T1 and T2 relaxation times of an agar/gelatin-based phantom. Another interesting trend observed is the decrease of T2 with increasing concentration of psyllium husk in gelatin-based phantoms [52]. Regarding the longitudinal relaxation time T1, it can be varied by incorporating different concentrations of paramagnetic ion salts, such as $MnCl_2$ [35], $NiCl_2$ [36], and $GdCl_3$ [37], or copper ions [23]. Finally, both T1 and T2 can be modified with the addition of proper type and concentration of MRI contrast agents [50].

Another remark emerging from the gathered data is that the same phantom ingredient may act differently on the MR relaxation properties when companied with different gelling agents. For instance, addition of NaCl in agar-based phantoms markedly affected T1 and T2 values [48]. On the contrary, the relaxation values of a PAA phantom were found independent of the NaCl concentration [73]. Therefore, the previously reported trends should be considered with caution, considering synergic components and how they may interrelate.

Preservatives are required to prevent bacterial invention and offer long-term use. NaN_3 is maybe the most widely used preservative since it was selected to lengthen the lifetime of various phantom types, including agar [31], PAA [70], and Carrageenan [47,48] phantoms.

Even though an ideal phantom would possess all the characteristics of the simulated tissue, this is extremely difficult. Thus, phantom recipes

are adjusted to simulate only the critical properties of tissue depending on the intended phantom application. In the current study, focus was placed on the MR properties of a wide range of TMPs. In synergy with other studies reviewing acoustical and thermal properties, the reported data is expected to facilitate the selection of appropriate materials for the construction of high-quality MRgFUS phantoms.

6. Conclusions and future prospects

In conclusion, agar-based phantoms appear to be very promising for use with the MRgFUS technology, without the toxicity issues related to PAA materials. Agar gels can be formed in any configuration through a simple manufacturing process while maintaining sufficient mechanical strength upon solidification. In addition, their lifetime can easily be extended with the addition of preservatives. In this category of phantoms, cheap and easy to obtain ingredients can be added as modifiers of acoustical and thermal properties. Their MR relaxation times can be predominantly tailored by varying the agar concentration to accurately match those of human tissue. However, the literature lacks targeted research on specific trends between added ingredients and resultant MR properties of these phantoms. The effect of varying concentration of common inclusions such as silicon dioxide and evaporated milk on the resultant MR relaxation properties of these phantoms is still to be investigated. Overall, the provided data could be useful in manufacturing more effective and realistic MRgFUS phantoms, while simultaneously indicating an opportunity for further research in the field with a particular focus on the MR behavior of agar-based TMPs.

Declaration of Competing Interest

The authors declare that they have no known competing financial interests or personal relationships that could have appeared to influence the work reported in this paper.

References

[1] C.K. McGarry, et al., Tissue mimicking materials for imaging and therapy phantoms: A review, Phys. Med. Biol. 65 (23) (2020) 1–43, https://doi.org/10.1088/1361-6560/abbd17.
[2] A. Dabbagh, B.J.J. Abdullah, C. Ramasindarum, N.H. Abu Kasim, Tissue-mimicking gel phantoms for thermal therapy studies, Ultrason. Imaging 36 (4) (2014) 291–316, https://doi.org/10.1177/0161734614526372.
[3] K. Abe, T. Taira, Focused ultrasound treatment, present and future, Neurol. Med. Chir. 57 (8) (2017) 386–391, https://doi.org/10.2176/nmc.ra.2017-0024.
[4] Z. Izadifar, Z. Izadifar, D. Chapman, P. Babyn, An introduction to high intensity focused ultrasound: systematic review on principles, devices, and clinical applications, J. Clin. Med. 9 (2) (2020) 460, https://doi.org/10.3390/jcm9020460.
[5] C.R. Hill, G.R. ter Haar, High intensity focused ultrasound—potential for cancer treatment, British J. Radiol. 68 (816) (1995) 1296–1303, https://doi.org/10.1259/0007-1285-68-816-1296.
[6] N.M. Duc, B. Keserci, Emerging clinical applications of high-intensity focused ultrasound, Diagnostic Intervent. Radiol. 25 (5) (2019) 398–409, https://doi.org/10.5152/dir.2019.18556.
[7] C.G. Hernando, L. Esteban, T. Cañas, E. Van Den Brule, M. Pastrana, The role of magnetic resonance imaging in oncology, Clin. Transl. Oncol. 12 (9) (2010) 606–613, https://doi.org/10.1007/s12094-010-0565-x.
[8] V. Rieke, K.B. Pauly, MR Thermometry, J. Magn. Reson. Imaging 27 (2) (2008) 376–390, https://doi.org/10.1002/jmri.21265.MR.
[9] N. Todd, M. Diakite, A. Payne, D.L. Parker, A Hybrid PRF/T1 Technique for Simultaneous Temperature Monitoring in Adipose and Aqueous Tissues, Magn. Reson. Med. 69 (1) (2014) 62–70, https://doi.org/10.1002/mrm.24228.

[10] A.C. Waspe, et al., Dynamic T2-mapping during magnetic resonance guided high intensity focused ultrasound ablation of bone marrow, AIP Conf. Proc. 1503 (222) (2012) 2–7, https://doi.org/10.1063/1.4769948.
[11] V. Hadjisavvas, K. Ioannides, M. Komodromos, N. Mylonas, C. Damianou, Evaluation of the contrast between tissues and thermal lesions in rabbit in vivo produced by high intensity focused ultrasound using fast spin echo MRI sequences, J Biomed. Sci. Eng. 4 (1) (2010) 51–61, https://doi.org/10.4236/jbise.2011.41007.
[12] A. Eranki, N. Farr, A. Partanen, K.V. Sharma, C.T. Rossi, A.Z. Rosenberg, AeRang Kim, M. Oetgen, H. Celik, D. Woods, P.S. Yarmolenko, P.C.W. Kim, B.J. Wood, Mechanical Fractionation of Tissues using Microsecond-Long HIFU Pulses on a Clinical MR-HIFU System, Int. J. Hyperthermia 34 (8) (2018) 1213–1224, https://doi.org/10.1080/02656736.2018.1438672.
[13] E. Kholmovski, R. Ranjan, N. Angel, N.F. Marrouche, T2* -weighted MRI technique for visualization of RF ablation lesions, J. Cardiovasc. Magn. Reson. 18 (Suppl 1) (2016) 2–4, https://doi.org/10.1186/1532-429X-18-S1-O128.
[14] M.R. Walker, J. Zhong, A.C. Waspe, T. Looi, K. Piorkowska, C. Hawkins, J.M. Drake, M. Hodaie, Acute MR-guided high-intensity focused ultrasound lesion assessment using diffusion-weighted imaging and histological analysis, Front. Neurol. 10 (2019), https://doi.org/10.3389/fneur.2019.01069.
[15] N. McDannold, K. Hynynen, D. Wolf, G. Wolf, F. Jolesz, MRI evaluation of thermal ablation of tumors with focused ultrasound, J. Magn. Reson. Imaging 8 (1) (1998) 91–100, https://doi.org/10.1002/jmri.1880080119.
[16] M. Wintermark, J. Druzgal, D.S. Huss, M.A. Khaled, S. Monteith, P. Raghavan, T. Huerta, L.C. Schweickert, B. Burkholder, J.J. Loomba, E. Zadicario, Y. Qiao, B. Shah, J. Snell, M. Eames, R. Frysinger, N. Kassell, W.J. Elias, Imaging findings in mr imaging-guided focused ultrasound treatment for patients with essential tremor, Am. J. Neuroradiol. 35 (5) (2014) 891–896, https://doi.org/10.3174/ajnr.A3808.
[17] G. Menikou, C. Damianou, Acoustic and thermal characterization of agar based phantoms used for evaluating focused ultrasound exposures, J. Ther. Ultrasound 5 (2017) 1–14, https://doi.org/10.1186/s40349-017-0093-z.
[18] C.K. McGarry, et al., Tissue mimicking materials for imaging and therapy phantoms: A review, Phys. Med. Biol. 65 (23) (2020), https://doi.org/10.1088/1361-6560/abbd17.
[19] R.L. King, B.A. Herman, S. Maruvada, K.A. Wear, G. Harris, Development of a HIFU phantom, AIP Conf. Proc. 911 (2007) 351–356, https://doi.org/10.1063/1.2744296.
[20] T. Drakos, et al., Ultrasonic Attenuation of an Agar, Silicon Dioxide, and Evaporated Milk Gel Phantom, J. Medical Ultrasound (2021) 1–11, https://doi.org/10.4103/JMU.JMU.
[21] R. Ortega, A. Téllez, L. Leija, A. Vera, Measurement of ultrasonic properties of muscle and blood biological phantoms, Phys. Proc. 3 (1) (2010) 627–634, https://doi.org/10.1016/j.phpro.2010.01.079.
[22] T. Drakos, M. Giannakou, G. Menikou, G. Constantinides, C. Damianou, Characterization of a soft tissue-mimicking agar/wood powder material for MRgFUS applications, Ultrasonics 113 (2021) 10635, https://doi.org/10.1016/j.ultras.2021.106357.
[23] M.D. Mitchell, H.L. Kundel, L. Axel, P.M. Joseph, Agarose as a tissue equivalent phantom material for NMR imaging, Magn. Reson. Imaging 4 (3) (1986) 263–266, https://doi.org/10.1016/0730-725X(86)91068-4.
[24] A. Partanen, C. Mougenot, T. Vaara, Feasibility of agar-silica phantoms in quality assurance of MRgHIFU, AIP Conf. Proc. 1113 (2009) 296–300, https://doi.org/10.1063/1.3131434.
[25] G. Menikou, T. Dadakova, M. Pavlina, M. Bock, C. Damianou, MRI compatible head phantom for ultrasound surgery, Ultrasonics 57 (2015) 144–152, https://doi.org/10.1016/j.ultras.2014.11.004.
[26] G. Menikou, M. Yiannakou, C. Yiallouras, C. Ioannides, C. Damianou, MRI-compatible breast/rib phantom for evaluating ultrasonic thermal exposures, Int. J. Med. Rob. Comput. Assisted Surg. 14 (1) (2018) 1–12, https://doi.org/10.1002/rcs.1849.
[27] G. Menikou, M. Yiannakou, C. Yiallouras, C. Ioannides, C. Damianou, MRI-compatible bone phantom for evaluating ultrasonic thermal exposures, Ultrasonics 71 (2016) 12–19, https://doi.org/10.1016/j.ultras.2016.05.020.
[28] D. Johnson, V. Zderic, Design and construction of a flow phantom for HIFU research, Proc. - IEEE Ultrasonics Symp. (2007) 1294–1296, https://doi.org/10.1109/ULTSYM.2007.325.
[29] D.W. Rickey, P.A. Picot, D.A. Christopher, A. Fenster, A wall-less vessel phantom for Doppler ultrasound studies, Ultrasound Med. Biol. 21 (9) (1995) 1163–1176, https://doi.org/10.1016/0301-5629(95)00044-5.
[30] E.L. Madsen, G.R. Frank, F. Dong, Liquid or solid ultrasonically tissue-mimicking materials with very low scatter, Ultrasound Med. Biol. 24 (4) (1998) 535–542, https://doi.org/10.1016/S0301-5629(98)00013-1.
[31] H. Kato, M. Hiraoka, T. Ishida, An agar phantom for hyperthermia, Int. J. Medical Phys. Res. Practice 13 (3) (1986) 396–398, https://doi.org/10.1118/1.595882.
[32] R.F. Smith, B.K. Rutt, D.W. Holdsworth, Anthropomorphic Carotid Bifurcation Phantom for MRI Applications, J. Magn. Reson. Imaging 10 (4) (1999) 533–544, https://doi.org/10.1002/(sici)1522-2586(199910)10:4<533::aid-jmri6>3.0.co;2-z.
[33] G. Captur, P. Gatehouse, K.E. Keenan, F.G. Heslinga, R. Bruehl, M. Prothmann, M.J. Graves, R.J. Eames, C. Torlasco, G. Benedetti, J. Donovan, B. Ittermann, R. Boubertakh, A. Bathgate, C. Royet, W. Pang, R. Nezafat, M. Salerno, P. Kellman, J.C. Moon, A medical device-grade T1 and ECV phantom for global T1 mapping quality assurance — the T 1 Mapping and ECV Standardization in cardiovascular magnetic resonance (T1MES) program, J. Cardiovasc. Magn. Reson. 18 (1) (2016), https://doi.org/10.1186/s12968-016-0280-z.

[34] J.O. Christoffersson, L.E. Olsson, S. Sjöberg, Nickel-doped agarose gel phantoms in MR imaging, Acta Radiol. 32 (5) (1991) 426–431, https://doi.org/10.3109/02841859109177599.

[35] Y. Chen, et al., Rapid Volumetric T1 Mapping of the Abdomen Using 3D Through-Time Spiral GRAPPA, Magn. Reson. Med. 75 (4) (2017) 1457–1465, https://doi.org/10.1002/mrm.25693.Rapid.

[36] Q. Li, X. Cao, H. Ye, C. Liao, H. He, J. Zhong, Ultrashort echo time magnetic resonance fingerprinting (UTE - MRF) for simultaneous quantification of long and ultrashort T 2 tissues, Magn. Reson. Med. 82 (4) (2019) 1359–1372, https://doi.org/10.1002/mrm.v82.410.1002/mrm.27812.

[37] M. Nezafat, S. Nakamori, T.A. Basha, A.S. Fahmy, T. Hauser, R.M. Botnar, Imaging sequence for joint myocardial T1 mapping and fat/water separation, Magn. Reson. Med. 81 (1) (2019) 486–494, https://doi.org/10.1002/mrm.27390.

[38] K. Jiang, Y. Zhu, S. Jia, Y. Wu, X. Liu, Y. Chung, Fast T1 mapping of the brain at high fi eld using Look-Locker and fast imaging, Magn. Reson. Imaging 36 (2017) 49–55, https://doi.org/10.1016/j.mri.2016.10.022.

[39] D. Tamada, T. Wakayama, H. Onishi, U. Motosugi, Multiparameter estimation using multi-echo spoiled gradient echo with variable flip angles and multicontrast compressed sensing, Magn. Reson. Med. 80 (4) (2018) 1546–1555, https://doi.org/10.1002/mrm.27151.

[40] T. Yoshida, A. Urikura, K. Shirata, Y. Nakaya, M. Endo, S. Terashima, Short tau inversion recovery in breast diffusion – weighted imaging : signal – to – noise ratio and apparent diffusion coefficients using a breast phantom in comparison with spectral attenuated inversion recovery, Radiol. Med. (Torino) 123 (4) (2018) 296–304, https://doi.org/10.1007/s11547-017-0840-9.

[41] A. Altermatt, F. Santini, X. Deligianni, S. Magon, T. Sprenger, L. Kappos, P. Cattin, J. Wuerfel, L. Gaetano, Design and construction of an innovative brain phantom prototype for MRI, Magn. Reson. Med. 81 (2) (2019) 1165–1171, https://doi.org/10.1002/mrm.27464.

[42] M. De Brabandere, C. Kirisits, R. Peeters, K. Haustermans, F. Van den Heuvel, Accuracy of seed reconstruction in prostate postplanning studied with a CT- and MRI-compatible phantom, Radiother. Oncol. 79 (2) (2006) 190–197, https://doi.org/10.1016/j.radonc.2006.04.009.

[43] D.M. Kashyap, A.J. Fagan, C.M. Moran, J.E. Browne, Comparative imaging study in ultrasound, MRI, CT, and DSA using a multimodality renal artery phantom, Med. Phys. 38 (2) (2011) 565–573, https://doi.org/10.1118/1.3533674.

[44] A. Kozana, T. Boursianis, G. Kalaitzakis, M. Raissaki, T.G. Maris, Neonatal brain: Fabrication of a tissue-mimicking phantom and optimization of clinical T1w and T2w MRI sequences at 1.5 T, Phys. Med. 55 (2018) 88–97, https://doi.org/10.1016/j.ejmp.2018.10.022.

[45] S. Pichardo, D. Melodelima, L. Curiel, J. Kivinen, Suitability of a tumour-mimicking material for the evaluation of high-intensity focused ultrasound ablation under magnetic resonance guidance, Phys. Med. Biol. 58 (7) (2013) 2163–2183, https://doi.org/10.1088/0031-9155/58/7/2163.

[46] K. Yoshimura, H. Kato, M. Kuroda, A. Yoshida, K. Hanamoto, A. Tanaka, M. Tsunoda, S. Kanazawa, K. Shibuya, S. Kawasaki, Y. Hiraki, Development of a Tissue-Equivalent MRI Phantom Using Carrageenan Gel, Magn. Reson. Med. 50 (5) (2003) 1011–1017, https://doi.org/10.1002/mrm.10619.

[47] W. Neumann, F. Lietzmann, L.R. Schad, F.G. Zöllner, Design of a multimodal (MR/CT) anthropomorphic thorax phantom, Z Med. Phys. 27 (2) (2017) 124–131, https://doi.org/10.1016/j.zemedi.2016.07.004.

[48] A. Yoshida, H. Kato, M. Kuroda, K. Hanamoto, K. Yoshimura, K. Shibuya, S. Kawasaki, M. Tsunoda, S. Kanazawa, Y. Hiraki, Development of a phantom compatible for MRI and hyperthermia using carrageenan gel — relationship between T 1 and T 2 values and NaCl concentration, Int. J. Hyperth. 20 (8) (2004) 803–814, https://doi.org/10.1080/0265673042000199268.

[49] W.D. D'Souza, E.L. Madsen, O. Unal, K.K. Vigen, G.R. Frank, B.R. Thomadsen, Tissue mimicking materials for a multi-imaging modality prostate phantom, Am Assoc Phys Med 28 (4) (2001) 688–700, https://doi.org/10.1118/1.1354998.

[50] B. Bazrafshan, F. Hübner, P. Farshid, M.C. Larson, V. Vogel, W. Mäntele, T.J. Vogl, A liver-mimicking MRI phantom for thermal ablation experiments, Med. Phys. 38 (5) (2011) 2674–2684, https://doi.org/10.1118/1.3570577.

[51] J.R. Rice, R.H. Milbrandt, E.L. Madsen, G.R. Frank, E.J. Boote, J.C. Blechinger, Anthropomorphic 1H MRS head phantom, Med. Phys. 25 (7) (1998) 1145–1156, https://doi.org/10.1118/1.598306.

[52] L.W. Hofstetter, L. Fausett, A. Mueller, H. Odéen, A. Payne, D.A. Christensen, D.L. Parker, Development and characterization of a tissue mimicking psyllium husk gelatin phantom for ultrasound and magnetic resonance imaging, Int. J. Hyperthermia 37 (1) (2020) 283–290, https://doi.org/10.1080/02656736.2020.1739345.

[53] Y.u. Yuan, C. Wyatt, P. Maccarini, P. Stauffer, O. Craciunescu, J. MacFall, M. Dewhirst, S.K. Das, A heterogeneous human tissue mimicking phantom for RF heating and MRI thermal monitoring verification, Phys. Med. Biol. 57 (7) (2012) 2021–2037, https://doi.org/10.1088/0031-9155/57/7/2021.

[54] E.L. Madsen, G.R. Frank, T.A. Krouskop, T. Varghese, F. Kallel, J. Ophir, Tissue-mimicking oil-in-gelatin dispersions for use in heterogeneous elastography phantoms, Ultrason. Imaging 25 (1) (2003) 17–38, https://doi.org/10.1177/016173460302500102.

[55] A.I. Farrer, H. Odéen, J. de Bever, B. Coats, D.L. Parker, A. Payne, D.A. Christensen, Characterization and evaluation of tissue-mimicking gelatin phantoms for use with MRgFUS, J. Ther. Ultrasound 3 (1) (2015), https://doi.org/10.1186/s40349-015-0030-y.

[56] C.-C. Cheng, F. Preiswerk, W.S. Hoge, T.-H. Kuo, B. Madore, Multi-Pathway Multi-Echo (MPME) imaging: all main MR parameters mapped based on a single 3D scan, Magn. Reson. Med. 81 (3) (2019) 1699–1713, https://doi.org/10.1002/mrm.v81.310.1002/mrm.27525.

[57] P.G. Anderson, N.C. Rouze, M.L. Palmeri, Effect of Graphite Concentration on Shear-Wave Speed in Gelatin-Based Tissue-Mimicking Phantoms, Ultrason Imaging 33 (2) (2011) 134–142, https://doi.org/10.1177/016173461103300204.

[58] M.P. Robinson, M.J. Richardson, J.L. Green, A.W. Preece, New materials for dielectric simulation of tissues, Phys. Med. Biol. 36 (1565) (1991).

[59] A. Bigi, G. Cojazzi, S. Panzavolta, N. Roveri, K. Rubini, Stabilization of gelatin films by crosslinking with genipin, Biomaterials 23 (24) (2002) 4827–4832, https://doi.org/10.1016/S0142-9612(02)00235-1.

[60] R.A. de Carvalho, C.R.F. Grosso, Characterization of Gelatin Based Films Modified with Transglutaminase, Glyoxal and Formaldehyde, Food Hydrocolloids 18 (5) (2004) 717–726, https://doi.org/10.1016/j.foodhyd.2003.10.005.

[61] A. Bigi, G. Cojazzi, S. Panzavolta, K. Rubini, N. Roveri, Mechanical and thermal properties of gelatin films at different degrees of glutaraldehyde crosslinking, Biomaterials 22 (8) (2001) 763–768, https://doi.org/10.1016/s0142-9612(00)00236-2.

[62] J.C. Blechinger, E.L. Madsen, G.R. Frank, Tissue mimicking gelatin–agar gels for use in magnetic resonance imaging phantoms, Med. Phys. 15 (4) (1988) 629–636, https://doi.org/10.1118/1.596219.

[63] E.L. Madsen, M.A. Hobson, H. Shi, T. Varghese, G.R. Frank, Tissue-mimicking agar/gelatin materials for use in heterogeneous elastography phantoms, Phys. Med. Biol. 50 (23) (2005) 5597–5618, https://doi.org/10.1088/0031-9155/50/23/013.

[64] A.K. Siddiqi, S.H. Cho, Agar-based heat-sensitive gel with linear thermal response over 65–80 °C, J. Therm. Anal. Calorim. 111 (2013) 1805–1809, https://doi.org/10.1007/s10973-012-2491-3.

[65] M. Lazebnik, E.L. Madsen, G.R. Frank, S.C. Hagness, Tissue-mimicking phantom materials for narrowband and ultrawideband microwave applications, Phys. Med. Biol. 50 (18) (2005) 4245–4258, https://doi.org/10.1088/0031-9155/50/18/001.

[66] C. Lafon, V. Zderic, M.L. Noble, J.C. Yuen, P.J. Kaczkowski, O.A. Sapozhnikov, F. Chavrier, L.A. Crum, S. Vaezy, Gel phantom for use in high-intensity focused ultrasound dosimetry, Ultrasound. Med. Biol. 31 (10) (2005) 1383–1389, https://doi.org/10.1016/j.ultrasmedbio.2005.06.004.

[67] N.P. Brodin, A. Partanen, P. Asp, C.A. Branch, C. Guha, W.A. Tomé, A simple method for determining the coagulation threshold temperature of transparent tissue-mimicking thermal therapy gel phantoms: Validated by magnetic resonance imaging thermometry, Med. Phys. 43 (3) (2016) 1167–1174, https://doi.org/10.1118/1.4941361.

[68] A. Eranki, A.S. Mikhail, A.H. Negussie, P.S. Katti, B.J. Wood, A. Partanen, Tissue-mimicking thermochromic phantom for characterization of HIFU devices and applications, Int. J. Hyperth. 36 (1) (2019) 518–529, https://doi.org/10.1080/02656736.2019.1605458.

[69] K. Takegami, Y. Kaneko, T. Watanabe, T. Maruyama, Y. Matsumoto, H. Nagawa, Polyacrylamide gel containing egg white as new model for irradiation experiments using focused ultrasound, Ultrasound. Med. Biol. 30 (10) (2004) 1419–1422, https://doi.org/10.1016/j.ultrasmedbio.2004.07.016.

[70] B. Bazrafshan, F. Hübner, P. Farshid, R. Hammerstingl, J. Paul, V. Vogel, W. Mäntele, T.J. Vogl, Temperature imaging of laser-induced thermotherapy (LITT) by MRI: Evaluation of different sequences in phantom, Lasers Med. Sci. 29 (1) (2014) 173–183, https://doi.org/10.1007/s10103-013-1306-5.

[71] M. McDonald, S. Lochhead, R. Chopra, M.J. Bronskill, Multi-modality tissue-mimicking phantom for thermal therapy, Phys. Med. Biol. 49 (13) (2004) 2767–2778, https://doi.org/10.1088/0031-9155/49/13/001.

[72] M.J. Choi, S.R. Guntur, K.IL. Lee, D.G. Paeng, A. Coleman, A Tissue Mimicking Polyacrylamide Hydrogel Phantom for Visualizing Thermal Lesions Generated by High Intensity Focused Ultrasound, Ultrasound. Med. Biol. 39 (3) (2013) 439–448, https://doi.org/10.1016/j.ultrasmedbio.2012.10.002.

[73] F. De Luca, B. Maraviglia, A. Mercurio, Biological tissue simulation and standard testing material for MRI, Magn. Reson. Med. 4 (2) (1987) 189–192, https://doi.org/10.1002/mrm.1910040213.

[74] K. Zell, J.I. Sperl, M.W. Vogel, R. Niessner, C. Haisch, Acoustical properties of selected tissue phantom materials for ultrasound imaging, Phys. Med. Biol. 52 (20) (2007) N475–N484, https://doi.org/10.1088/0031-9155/52/20/N02.

[75] G.M. Soultanidis, J.E. MacKewn, C. Tsoumpas, P.K. Marsden, PVA cryogel for construction of deformable PET-MR visible phantoms, IEEE Trans. Nucl. Sci. 60 (1) (2013) 95–102, https://doi.org/10.1109/TNS.2013.2238952.

[76] S.-S. Chen, P. Hellier, M. Marchal, J.-Y. Gauvrit, R. Carpentier, X. Morandi, D.L. Collins, An anthropomorphic polyvinyl alcohol brain phantom based on Colin27 for use in multimodal imaging, Am. Assoc. Phys. 39 (1) (2012) 554–561, https://doi.org/10.1118/1.3673069.

[77] K.J.M. Surry, H.J.B. Austin, A. Fenster, T.M. Peters, Poly(vinyl alcohol) cryogel phantoms for use in ultrasound and MR imaging, Phys. Med. Biol. 49 (24) (2004) 5529–5546, https://doi.org/10.1088/0031-9155/49/24/009.

[78] Y. He, Y. Liu, B.A. Dyer, J.M. Boone, S. Liu, T. Chen, F. Zheng, Y.e. Zhu, Y. Sun, Y.i. Rong, J. Qiu, 3D-printed breast phantom for multi-purpose and multi-modality imaging, Quant. Imaging Med. Surgery 9 (1) (2019) 63–74, https://doi.org/10.21037/qims.2019.01.05.

[79] S. Chatelin, E. Breton, A. Arulrajah, C. Giraudeau, B. Wach, L. Meylheuc, J. Vappou, Investigation of PolyVinyl Chloride Plastisol Tissue-Mimicking Phantoms for MR- and Ultrasound-Elastography, Front. Phys. 8 (2020), https://doi.org/10.3389/fphy.2020.577358.

[80] W. Li, B. Belmont, J.M. Greve, A.B. Manders, B.C. Downey, X.i. Zhang, Z. Xu, D. Guo, A. Shih, Polyvinyl chloride as a multimodal tissue-mimicking material with tuned mechanical and medical imaging properties, Med. Phys. 43 (10) (2016) 5577–5592, https://doi.org/10.1118/1.4962649.

[81] D. Goldstein, H. Kundel, M. Daube-Witherspoon, L. Thibault, E. Goldstein, A silicone gel phantom suitable for multimodality imaging, Invest. Radiol. 22 (2) (1987) 153–157, https://doi.org/10.1097/00004424-198702000-00013.

[82] M.A. Dieringer, J. Hentschel, T. de Quadros, F. von Knobelsdorff-Brenkenhoff, W. Hoffmann, T. Niendorf, J. Schulz-Menger, Design, construction, and evaluation of a dynamic MR compatible cardiac left ventricle model, Med. Phys. 39 (8) (2012) 4800–4806, https://doi.org/10.1118/1.4736954.

[83] G.P. Mazzara, R.W. Briggs, Z. Wu, B.G. Steinbach, Use of a modified polysaccharide gel in developing a realistic breast phantom for MRI, Magn. Reson. Imaging 14 (6) (1996) 639–648, https://doi.org/10.1016/0730-725X(96)00054-9.

[84] M.W. Groch, J.A. Urbon, W.D. Erwin, S. Al-Doohan, An MRI tissue equivalent lesion phantom using a novel polysaccharide material, Magn. Reson. Imaging 9 (3) (1991) 417–421, https://doi.org/10.1016/0730-725X(91)90430-T.

[85] A. Antoniou, et al., Simple methods to test the accuracy of MRgFUS robotic systems, Int. J. Med. Robot. 17 (4) (2021), https://doi.org/10.1002/rcs.2287.

[86] C. Yiallouras, N. Mylonas, C. Damianou, MRI-compatible positioning device for guiding a focused ultrasound system for transrectal treatment of prostate cancer, Int. J. Comput. Assist. Radiol. Surg. 9 (4) (2014) 745–753, https://doi.org/10.1007/s11548-013-0964-x.

[87] J.S. Huber, Q. Peng, W.W. Moses, Multi-modality phantom development, IEEE Trans. Nucl. Sci. 56 (5) (2009) 2722–2727, https://doi.org/10.1109/TNS.2009.2028073.

[88] H. Kato, M. Kuroda, K. Yoshimura, S. Kawasaki, N. Yamamoto, An MRI phantom using carrageenan gel, Nippon Jiki Kyomei Igakkai Zasshi 20 (8) (2000) 365–373.

MEDICAL IMAGING

MR relaxation times of agar-based tissue-mimicking phantoms

Anastasia Antoniou[1] | **Leonidas Georgiou[2]** | **Theodora Christodoulou[2]** | **Natalie Panayiotou[2]** | **Cleanthis Ioannides[2]** | **Nikolaos Zamboglou[2]** | **Christakis Damianou[1]**

[1] Department of Electrical Engineering, Computer Engineering, and InformaticsCyprus University of Technology, Limassol, Cyprus

[2] Department of Interventional Radiology, German Oncology Center, Limassol, Cyprus

Correspondence
Christakis Damianou, Department of Electrical Engineering, Computer Engineering, and Informatics, Cyprus University of Technology, 30 Archbishop Kyprianou Street, 3036 Limassol, Cyprus.
Email: christakis.damianou@cut.ac.cy

Abstract
Agar gels were previously proven capable of accurately replicating the acoustical and thermal properties of real tissue and widely used for the construction of tissue-mimicking phantoms (TMPs) for focused ultrasound (FUS) applications. Given the current popularity of magnetic resonance-guided FUS (MRgFUS), we have investigated the MR relaxation times $T1$ and $T2$ of different mixtures of agar-based phantoms. Nine TMPs were constructed containing agar as the gelling agent and various concentrations of silicon dioxide and evaporated milk. An agar-based phantom doped with wood powder was also evaluated. A series of MR images were acquired in a 1.5 T scanner for $T1$ and $T2$ mapping. $T2$ was predominantly affected by varying agar concentrations. A trend toward decreasing $T1$ with an increasing concentration of evaporated milk was observed. The addition of silicon dioxide decreased both relaxation times of pure agar gels. The proposed phantoms have great potential for use with the continuously emerging MRgFUS technology. The MR relaxation times of several body tissues can be mimicked by adjusting the concentration of ingredients, thus enabling more accurate and realistic MRgFUS studies.

KEYWORDS
agar, MR relaxation times, MRgFUS, tissue-mimicking phantoms

1 | INTRODUCTION

Tissue-mimicking phantoms (TMPs) are increasingly used for the preclinical validation of diagnostic and therapeutic modalities, reducing the use of animal subjects.[1] Gel phantoms constitute a more economical and ergonomic solution for preclinical research compared to experimental animals, also given that their lifespan can be simply lengthened by adding preservatives.[1,2] Several categories of gelling agents, including agar,[3] gelatin,[4] polyacrylamide (PAA),[5] poly-vinyl alcohol,[6] polyvinyl chloride,[7] silicone,[8] and TX-151,[9] have been used in the construction of gel phantoms for quality assessment purposes in medicine and biomedical research. Accurate replication of tissue properties is of great importance for the efficacy of such procedures, especially when evaluating therapeutic applications with clinical potential.

The current increasing application of focused ultrasound (FUS) in medicine[10] requires the development of high-quality TMPs specially designed for use with this specific technology to accelerate its clinical translation. The FUS-induced thermal effects were proven to be essential in many oncological applications, thereby serving as an alternative therapeutic solution over surgical and systemic approaches.[11] Thermal therapy

with FUS is based on the ability to precisely focus extracorporeal ultrasonic waves into a millimeter-sized area of malignant tissue, thus elevating the temperature to hyperthermic or ablative levels.[12] Therefore, TMPs intended for FUS studies should be capable of accurately replicating both the acoustical and thermal characteristics of biological tissue. Under FUS exposure, the thermal behavior of a material is a function of various parameters, among which the most critical are the specific heat capacity, thermal conductivity, and thermal diffusivity.[13–14] Concerning acoustical characteristics, the key properties to be emulated are the speed of sound in the medium, acoustic impedance, and attenuation coefficient.[13–14]

FUS treatment is typically applied under the US or magnetic resonance imaging (MRI) guidance,[11] with MRI being the method of choice because of its superior imaging resolution and its ability to acquire temperature data by intraoperative MR thermometry.[15,16] The contrast in MR images emerges from changes in the proton density and the magnetic relaxation times $T1$ and $T2$ of tissues.[16] Several animal studies have shown that the MR parameters of tissue greatly affect the contrast between normal untreated tissue and FUS-ablated areas.[17,18] In fact, the MR relaxation times of FUS lesions were found to vary depending on the tissue type, suggesting that the MR properties of the host tissue define the MR appearance of lesions.[17] More importantly, the temperature dependence of tissue relaxation times allows for noninvasive temperature monitoring during thermal applications.[16,19] Therefore, precise replication of MR relaxation parameters is essential for producing tissue-like MR signals and more realistic temperature maps in the process of evaluating thermal protocols. It is thus of paramount importance that TMPs are both US and MR imageable and possess tissue-like MR properties in order to be qualified for use with the magnetic resonance-guided FUS (MRgFUS) technology.

So far, PAA, gelatin, and agar-based phantoms were proven efficient to properly mimic biological tissues in thermal studies by replicating critical acoustical, thermal, and MR properties.[2–5] Agar and PAA gels are favorable in that they possess melting points sufficiently high for ablative FUS, whereas gelatin phantoms are only proposed for hyperthermia applications since they lack the capacity to withstand ablative temperatures.[2]

PAA gels are beneficial over agar gels in that they are transparent, allowing for visually discriminating coagulative areas.[5,20] These phantoms normally contain heat-sensitive materials, such as bovine serum albumin proteins[20] and thermochromic ink,[5] which exhibit progressive color change and irreversible MR changes upon heating at ablative temperatures. Although visualization of lesions is a substantial advantage of this phantom category, permanent changes make them unsuitable for repeated use. In addition, the ingredients of PAA-based gels are considered to have toxic environmental effects restricting their wider utilization.[2]

On the other hand, agar gels serve as a more natural alternative having easier and more cost-effective preparation and storage.[3] They can be easily shaped to any configuration to form phantoms of durable stability. Their tissue-like MR signal makes them the material of choice for MRI studies.[21–27] In fact, a wide variety of agar-based phantoms simulating specific body parts, such as prostate,[27] carotid,[21] and brain,[26] have been proposed in the literature for evaluating new MR protocols and imaging techniques. This phantom type has also been quite widely used for thermal studies with FUS,[3,28–31] where agar served as the gelling agent, and proper concentration of other materials was added to modify mainly the thermal and acoustical properties depending on the tissue to be mimicked. Notably, quite large data on the acoustical properties of agar phantoms exist in the literature. Silicon dioxide,[28] graphite, and cellulose particles,[32] are examples of ingredients that served as attenuation modifiers enhancing ultrasonic scattering. Accordingly, evaporated milk was shown to be a prominent absorber of acoustic energy, also enhancing ultrasonic attenuation,[4] whereas ultrasonic velocity can be adjusted by incorporating proper concentration of glycerol.[32]

Although more limited research has been applied in the investigation of MR parameters of agar-based phantoms, some interesting trends become apparent through the literature. Agar turned out to be the prominent $T2$ modifier even in the case where another material serves as the gelling agent.[25,33] $T1$ was predominantly tailored by varying the concentration of paramagnetic ion salts[22,23] and copper ions.[25]

We have previously proposed and characterized several agar-based phantoms by estimating critical tissue properties, including the mass density, speed of sound, acoustic attenuation, acoustic impedance, thermal diffusivity, specific heat, and thermal conductivity.[3,14,29] Given the current need for TMPs that can also replicate critical MR parameters, as well as the lack of targeted research on trends between added ingredients and resultant MR properties of agar phantoms, we have investigated the MR relaxation times of different mixtures of agar-based phantoms previously proposed by our group.[3,14]

2 | METHODS

This study concerns the development and MR characterization of agar-based phantoms. No animals or patients were involved in the study. Therefore, no informed consent from patients or approval from an ethics committee was required.
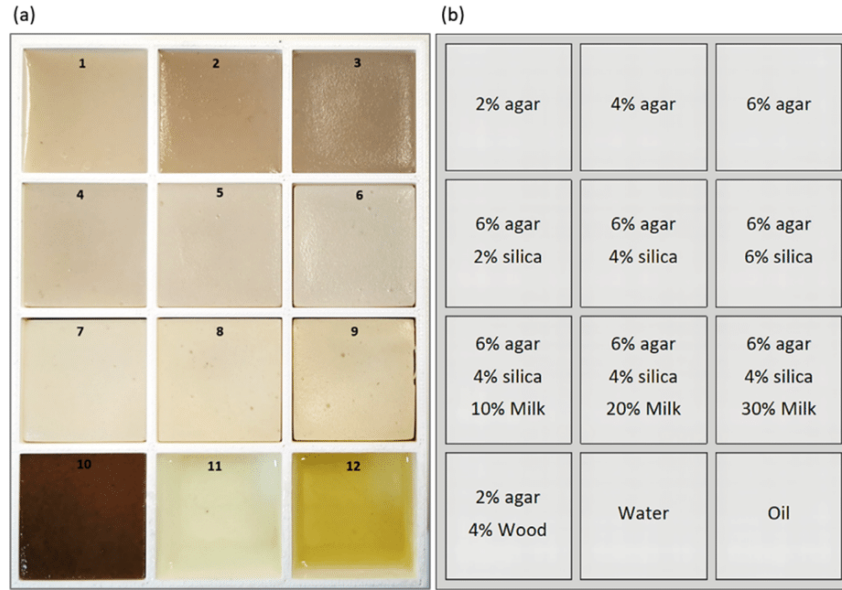
FIGURE 1 (a) Photo of the phantoms in the container and (b) the corresponding recipe used for each one

2.1 | Phantoms' development

Ten agar-based phantoms with different concentrations of additives were prepared and contained in a rectangular container. The container was specially developed having 12 compartments to accommodate the TMPs and two reference liquids (water and oil), as shown in Figure 1a. Figure 1b shows the composition of the corresponding materials used in each insert. The preparation process of the phantoms was previously described in detail.[3]

Three phantoms with varying agarose (Merck KGaA, EMD Millipore Corporation, Darmstadt, Germany) concentrations of 2%–6% weight per volume (w/v) were prepared to assess the role of agar as a modifier of the relaxation times. The effect of varying silicon dioxide (Sigma-Aldrich, St. Louis, Missouri, United States) concentration (2%–6% w/v) on the relaxation times was then investigated using a certain amount of 6% w/v agar. Finally, various amounts of evaporated milk (Nounou, Friesland Campina, Marousi, Greece) were added in phantoms with fixed concentrations of 6% w/v agar and 4% w/v silicon dioxide. The volume per volume (v/v) concentration of evaporated milk varied from 10% to 30%.

Agar-based phantoms doped with wood powder were previously found to possess lower thermal conductivity compared to the silica/evaporated milk doped phantoms and an acoustic absorption coefficient closer to that of soft tissue.[3] Thereby, another phantom containing 2% w/v agar and 4% w/v wood powder was constructed according to the procedure previously described by our group.[3]

2.2 | MR properties of phantoms

2.2.1 | Physical principle of MR relaxation times

Tissues are characterized by two relaxation times, which describe the rate at which protons return to equilibrium following a radiofrequency pulse. The maximum transverse magnetization M_{0xy} after a radiofrequency pulse is lost with time as the spinning protons interact with each other and lose phase coherence. $T2$ is the transverse relaxation time, which by default equals the time needed for the transverse magnetization (M_{xy}) to fall to approximately 37% of its maximum value (M_{0xy}) and mathematically is defined by the following equation[34]:

$$M_{xy} = M_{0xy}\, e^{-\frac{TE}{T2}} \qquad (1)$$

where TE is the echo time.

Accordingly, $T1$ relates to the realignment of spinning protons with the external magnetic field and is defined as the time required for the longitudinal magnetization (M_z) to recover to approximately 63% of its maximum value (M_{oz}). Mathematically, this recovery is described as follows[34]:

$$M_z = M_{0z}\left(1 - 2e^{-\frac{TI}{T1}}\right) \qquad (2)$$

where TI represents the inversion time. It is noted that this expression assumes that the repetition time (TR) is sufficiently longer than the $T1$ to be estimated.

FIGURE 2 The phantom container positioned on the magnetic resonance imaging (MRI) table within the posterior head and face part of the head/neck/spine (HNS) coil

2.2.2 | Estimation of MR relaxation parameters

The developed phantoms were imaged in a 1.5 T MRI scanner (GE Signa HD16; GE Healthcare, Milwaukee, Wisconsin, USA) to demonstrate the effect of the various additives on their MR properties. The container was covered by the posterior head and face part of a head/neck/spine coil (Signa 1.5T, 16 channel, GE Healthcare) as shown in Figure 2.

A 2D MultiEcho imaging sequence was used for assessing the transverse relaxation time. Multiple coronal scans were obtained at variable TE values, thus demonstrating the transverse magnetization exponential decay. $T2$ was estimated by fitting the measured signal intensity (SI) over TE to the exponential function of Equation (1). The images were acquired with the following parameters: TR = 200 ms, TE = 12.0–250.0 ms, flip angle = 90°, echo train length (ETL) = 4, pixel bandwidth (pBW) = 122.1 kHz, matrix size = 160 × 128, field of view = 260 × 260 mm^2, slice thickness = 7 mm, and number of excitations (NEX) = 0.75.

Accordingly, $T1$-weighted ($T1W$) inversion recovery (IR) fast spin echo (FSE) images of the phantoms were obtained at variable TIs for $T1$ mapping. The data were fitted into Equation (2) to estimate the longitudinal relaxation time ($T1$). Two-dimensional axial images were acquired with the following parameters: TR = 7000 ms, TE = 9.94 ms, TI = 50 - 3000 ms, flip angle = 90°, ETL = 9, pBW = 27.10 kHz, matrix size = 192 × 128, field of view = 260 × 260 mm^2, slice thickness = 7 mm, and NEX = 1.

The methodology for estimating the MR relaxation times of each phantom included both region of inter-est (ROI) and voxel-by-voxel analysis. The ROI approach for $T1$ and $T2$ mapping involved measurement of the SI in specific predefined ROI in the phantom for each TI and TE, respectively. The mean values of the SI were fitted to Equations (1) and (2). Similarly, in the voxel-based approach, parametric maps were derived from the series of images by fitting the mathematic models to the acquired data for each individual voxel through automated algorithmic processing.

3 | RESULTS

The phantoms were initially scanned in the coronal plane using a multi-echo sequence with TE values ranging from 12 to 250 ms. Figure 3 shows indicative MR images acquired at various TEs within this range. Figure 4 shows an indicative graph of the estimated mean SI in a predefined ROI of the phantom in insert 7 (6% w/v agar, 4% w/v silica, and 10% v/v milk) plotted against the TE, demonstrating the rate of transverse magnetization decay. The $T2$ parametric map of the phantoms as generated by the voxel-by-voxel analysis is presented in Figure 5.

Imaging of phantoms was then done in the axial plane using a $T1W$ IR FSE sequence at various TI values in the range of 50 to 3000 ms. Indicative results are presented in Figure 6, where the yellow dotted circles indicate the phantoms with the lowest SI for each TI. A typical graph of the change in SI with increasing TI value as estimated by the ROI approach is shown in Figure 7, which demonstrates the mean SI versus TI for the phantom in insert 9 (6 % w/v agar, 4 % w/v silica, and 30 % v/v evaporated milk). The $T1$ parametric map generated by the voxel-by-voxel analysis is presented in Figure 8.

The mean value of the $T1$ and $T2$ relaxation times and the corresponding standard deviations for each phantom as estimated by the voxel-based approach are listed in Table 1. Figure 9A,B shows the estimated $T1$ and $T2$ values plotted against the agar concentration, respectively, where the data points were fitted to a 2nd order polynomial ($R^2 = 1$) using non-linear least square regression. Accordingly, the effect of varying amounts of silicon dioxide and evaporated milk on $T1$ is presented in Figure 10, in which the graphs also represent 2nd order polynomials ($R^2 = 0.899$ and 0.999, respectively).

4 | DISCUSSION

Ten different agar-based TMPs were prepared and imaged in a 1.5 T MRI scanner to assess their suitability to match the MR properties of real tissue. It is widely known that the MR SI depends on the characteristic relaxation times of the imaged object.[16] A typical methodology that makes use of this dependency was followed for $T1$ and $T2$ mapping. A series of MultiEcho
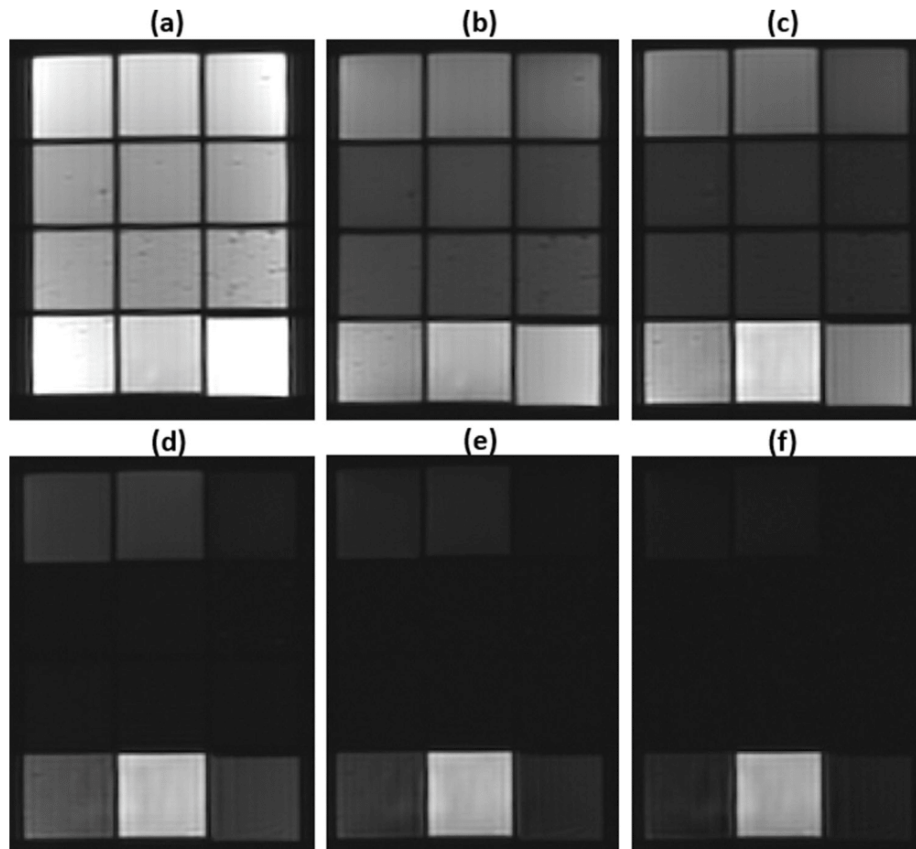
FIGURE 3 Coronal slices acquired using a 2D multi-echo sequence at echo times of (a) 12 ms, (b) 36 ms, (c) 50 ms, (d) 100 ms, (e) 150 ms, and (f) 200 ms

TABLE 1 Mean $T1$ and $T2$ and standard deviation (SD) of phantoms as estimated by voxel-based analysis

Phantom #	Recipe	$T2$ (ms)	SD (ms)	$T1$ (ms)	SD (ms)
1	2% agar	46.2	1.1	1669.5	13.3
2	4% agar	46.7	1.0	1662.7	27.6
3	6% agar	29.4	1.7	1394.9	3.8
4	6% agar, 2% silica	20.9	0.4	1249.8	6.4
5	6% agar, 4% silica	23.4	0.2	1251	3.0
6	6% agar, 6% silica	19.0	0.3	1147.7	7.3
7	6% agar, 4% silica, 10% milk	23.0	0.2	1038.8	4.7
8	6% agar, 4% silica, 20% milk	21.8	0.2	916.8	6.4
9	6% agar, 4% silica, 30% milk	20.1	0.23	841.3	8.1
10	2% agar, 4% wood	65.2	2.7	837.5	12.0
11	Water	–	–	2125.6	42.1
12	Oil	55.2	3.4	193.3	1.8

images were acquired at different TE values for $T2$ mapping. Accordingly, $T1$ mapping was performed by acquiring $T1$W IR images at different TIs after applying the inversion pulse (180°). The relaxation times were estimated by fitting the acquired data to the signal decay and recovery curves, respectively, through both ROI and voxel-based approaches.

Pure agarose phantoms were initially scanned to demonstrate the effect of agar concentration on the relaxation times. Both relaxation parameters showed
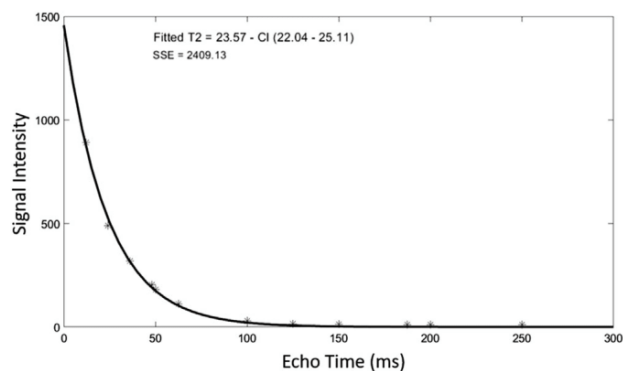
FIGURE 4 Plot of the mean signal intensity measured from the multi-echo images using the region of interest approach against echo time for phantom 7 (6% w/v agar, 4% w/v silica, and 10% v/v milk). SSE corresponds to the sum of square errors. CI corresponds to 95% confidence intervals for the estimated values

FIGURE 5 $T2$ parametric map of phantoms. The map was generated by voxel-based analysis of a series of 2D coronal MultiEcho images with different echo time values (12–250 ms)

similar behavior. Increment of the agar concentration from 2% to 4% w/v had no impact on the resultant relaxation times, whereas both $T1$ and $T2$ showed a noticeable decrease as agar concentration increased to 6% w/v. It is notable that the relation between both relaxation times and the agar concentration can be perfectly modeled as a 2nd-degree polynomial function ($R^2 = 1$). Although the present results are in line with previous studies[25,33] proposing agarose as a $T2$ modifier, they suggest that this only applies for agar concentrations of 4% w/v and above.

The change in MR properties of agar gels upon the addition of various amounts of silicon dioxide and evap-

orated milk was then assessed. The addition of silica particles further lowered the relaxation times. However, no specific trend became apparent with increasing silicon dioxide concentration for none of the relaxation times. The results further suggest that the addition of evaporated milk has no specific impact on $T2$, whereas a noticeable decrease is observed in the case of the longitudinal relaxation time ($T1$). In fact, the $T2$ relaxation time of milk-doped agar gels (6% w/v agar and 4% w/v silicon dioxide) remained similar to those containing only silicon dioxide. On the contrary, milk-doped agar/silica gels exhibit noticeably shorter $T1$ relaxation
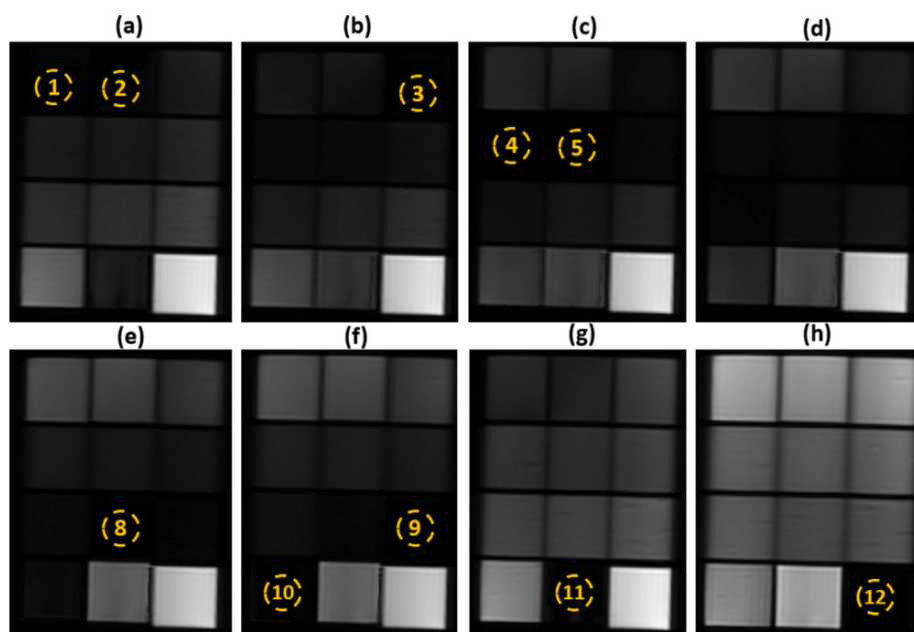
FIGURE 6 Axial slices of the phantoms acquired using a 2D $T1$W IR FSE sequence at inversion times of (a) 1200 ms, (b) 1000 ms, (c) 900 ms, (d) 800 ms, (e) 650 ms, (f) 600 ms, (g) 1500 ms and (h) 125 ms. The material shown in the yellow dotted circle has the lowest SI
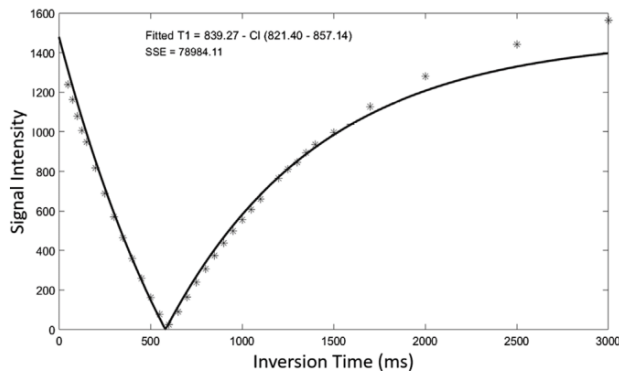
FIGURE 7 Plot of the mean signal intensity measured from the *T*1-weighted inversion recovery fast spin echo (*T*1W IR FSE) images using the region of interest approach against inversion time for phantom 9 (6% w/v agar, 4% w/v silica, and 30% v/v evaporated milk). SSE corresponds to the sum of square errors. CI corresponds to 95% confidence intervals for the estimated values
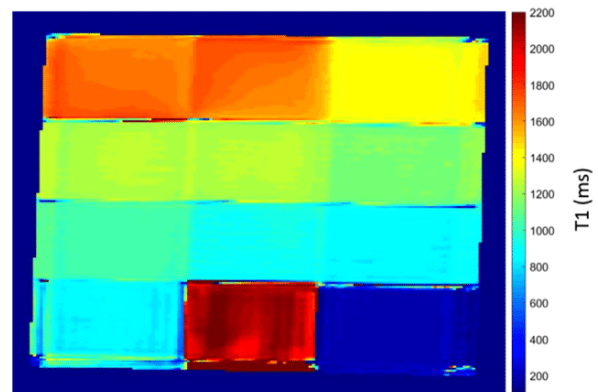

FIGURE 8 *T*1 parametric map of phantoms. The map was generated by voxel-based analysis of a series of 2D axial *T*1-weighted inversion recovery fast spin echo (*T*1W IR FSE) images with different inversion time values (50–3000 ms)

times, with increasing evaporated milk concentration (0%–30 % v/v) resulting in a gradual reduction of *T*1 in a 2nd order polynomial manner ($R^2 = 0.999$). This implies that *T*1 and *T*2 may be changed independently; however, this should be further investigated. It is also noted that milk concentrations higher than 30%, which would probably lower *T*1 even more, were not attempted because they would result in loose phantoms.[35]

Our results further demonstrated that agarose could also serve as a *T*1 modifier. However, it seems that *T*2 depends more strongly on the amount of agarose and is not remarkably affected by the concentration of other additives. Note that with increasing agar concentration at TEs of 36–200 ms the signal drops (Figure 3). On the contrary, with a fixed agar concentration of 6% w/v and increasing silica, the signal does not change much. Note also that the same holds by increasing the milk concentration. This result ties well with previous studies wherein *T*2 was mostly defined by the gelling agent concentration, whereas *T*1 was mainly varied by incorporating different concentrations of paramagnetic ion salts.[22–24]

The MR parameters of TMPs have been previously shown to be dependent on the concentration of scatterers.[4,36] In a study by Hofstetter et al.,[4] a decrease of *T*2 occurred with increasing concentration of psyllium husk in gelatin-based phantoms. A similar trend was reported in a study by Huber et al.,[36] wherein the inclusion of glass beads shortened *T*1 of an agar/gelatin-based phantom. Herein, the addition of wood scatterers also lowered *T*1 of pure agar gel (2% w/v). The phantoms doped with silicon dioxide appeared with lower relaxation times compared to agar only gels as well. However, it should be emphasized that the trend with increasing silica is not reliable as the distribution of silica in the material might be random.

Overall, the MR relaxation times of the proposed agar-based phantoms are comparable with the values reported for body tissues. A review article by Bottomley et al.[37] reports *T*2 relaxation times of soft tissues ranging roughly between 40 and 80 ms. Herein, the estimated *T*2 values ranged from a minimum value of 19.0 (±0.3) ms for the phantom in insert 6 (6% agar, 6% silica) to a maximum value of 65.2 (±2.7) ms for the phantom in insert 10 (2% agar and 4% wood). Authors also report a
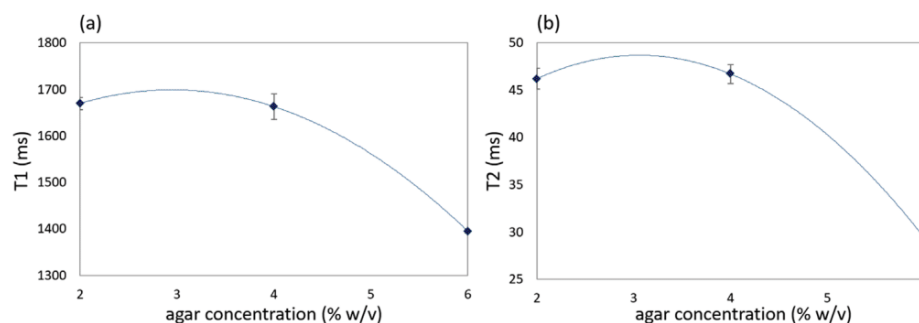

FIGURE 9 The mean (a) *T*1 and (b) *T*2 values plotted against the agar concentration. The data points are fitted by polynomial regression where the error bars correspond to the standard deviation as estimated by voxel-based analysis
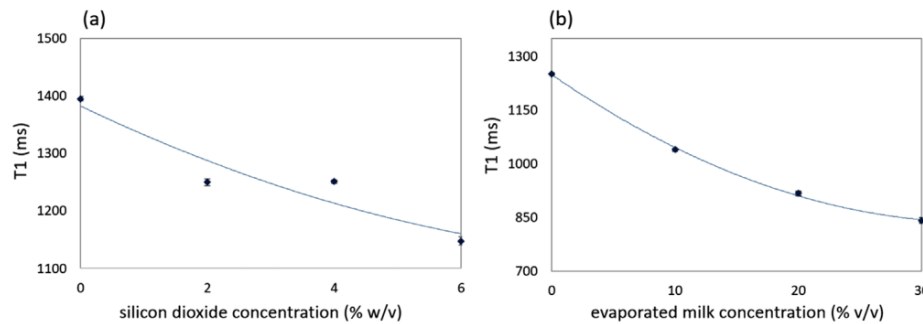
FIGURE 10   The mean $T1$ value plotted against (a) the silica concentration for a fixed amount of 6% w/v agar and (b) the evaporated milk concentration for fixed amounts of 6% w/v agar and 4% w/v silica. The data points are fitted by polynomial regression where the error bars correspond to the standard deviation as estimated by voxel-based analysis

mean $T2$ in adipose tissue of 84 (±36) ms,[37] which compares well with the value of 55.2 (±3.4) ms found by the current study for oil. At this point, it should be noted that the $T2$ measurement of water is not reported because of insufficiently high echo times due to machine limitations. Regarding the longitudinal relaxation time, the estimated $T1$ values range from 837.5 (±12) ms to 1669.5 (±13.3) ms for the phantoms in inserts 10 and 1, respectively. These estimates are partly consistent with the literature documenting $T1$ values for soft tissues harshly between 500 and 1000 ms.[38]

The several phantom recipes can be matched with specific tissue types through a more detailed comparison with the cited literature. For instance, by using concentrations of 2% w/v agar and 4% w/v wood (phantom in insert 10), a $T2$ value of 65.2 (±2.7) ms was found, which agrees with the value of 61 (±11) ms reported by prior research for the kidney tissue.[38] Regarding the $T1$ relaxation time, the value of 837.5 (±12.0) ms estimated by the current study is quite higher than the value of 709 (±60) reported literally for the kidney.[38] Accordingly, the silica/milk doped phantom in insert 7 was found to possess MR properties close to that of skeletal muscle and heart tissue (at 1.5 T).[38] Note that the high $T1$ values estimated for the agar only phantoms can only be well correlated to the $T1$ relaxation times of human blood.[38]

Finally, it is important to notify the reader that quantitative relaxation times are particularly dependent upon the used pulse sequence.[39–40] Furthermore, although the proposed multi-echo SE sequence is conventionally selected for $T2$ relaxometry significantly reducing the scan time of single-echo sequences, it is accompanied by the limitation that $T2$ overestimation may occur when the applied $180°C$ RF pulses fail to perfectly refocus magnetization, which is actually challenging in real practice.[41] Accordingly, $T1$ values may also be underestimated if the TR values employed in the IR sequence are not chosen properly.[40] Therefore, optimal imaging parameters should be employed for accurate and reliable $T1$ and $T2$ determination. It is thus recommended

that the variance in relaxation values between different sequences, as well as their dependence on precise prescan settings should be taken into consideration when comparing the current results with those of other similar studies.[42]

5 | CONCLUSIONS

Overall, the proposed phantoms can be formed in any configuration while maintaining the desired mechanical strength upon solidification. Their manufacturing process is easy, and the materials used are cheap and easy to obtain. The current findings suggest that the transverse relaxation time ($T2$) of agar-based phantoms can be predominantly tailored by varying the agar concentration. The inclusion of silicon dioxide lowers both relaxation times, whereas increasing evaporated milk concentration results in a gradual reduction of the longitudinal time ($T1$). Accordingly, the $T1$ and $T2$ relaxation parameters of several body tissues can be accurately matched by a proper concentration of these inclusions. Therefore, the proposed phantoms have great potential for use with the continuously emerging MRgFUS technology, also given their previously demonstrated feasibility to emulate all critical thermal and acoustical properties of human tissues.

AUTHOR CONTRIBUTIONS
Anastasia Antoniou contributed to analyzing the findings and drafting the work. Leonidas Georgiou contributed

to the analysis and interpretation of MR data for the work. Theodora Christodoulou contributed to the acquisition of MR data for the work. Natalie Panayiotou contributed to the acquisition of MR data for work. Cleanthis Ioannides contributed to the MRI experiments and interpretation of results. Nikolaos Zamboglou contributed to the MRI experiments and interpretation of results. Christakis Damianou served as the scientific coordinator and supervised the development of phantoms, implementation of the experiments, and drafting of the manuscript.

DATA AVAILABILITY STATEMENT

The data that support the findings of this study are available from the corresponding author upon reasonable request.

REFERENCES

1. McGarry CK, Grattan LJ, Ivory AM, et al. Tissue mimicking materials for imaging and therapy phantoms: a review. *Phys Med Biol*. 2020;65(23):1-43. https://doi.org/10.1088/1361-6560/abbd17.
2. Dabbagh A, Abdullah BJJ, Ramasindarum C, Abu Kasim NH. Tissue-mimicking gel phantoms for thermal therapy studies. *Ultrason Imaging*. 2014;36(4):291-316. https://doi.org/10.1177/0161734614526372.
3. Drakos T, Giannakou M, Menikou G, Constantinides G, Damianou C. Characterization of a soft tissue-mimicking agar/wood powder material for MRgFUS applications. *Ultrasonics*. 2021;113:10635. https://doi.org/10.1016/j.ultras.2021.106357.
4. Hofstetter LW, Fausett L, Mueller A, et al. Development and characterization of a tissue-mimicking psyllium husk gelatin phantom for ultrasound and magnetic resonance imaging. *Int J Hyperthermia*. 2020;37(1):283-290. https://doi.org/10.1080/02656736.2020.1739345.
5. Eranki A, Mikhail AS, Negussie AH, Katti PS, Wood BJ, Partanen A. Tissue-mimicking thermochromic phantom for characterization of HIFU devices and applications. *Int J Hyperthermia*. 2019;36(1):518-529. https://doi.org/10.1080/02656736.2019.1605458.
6. Surry KJM, Austin HJB, Fenster A, Peters TM. Poly(vinyl alcohol) cryogel phantoms for use in ultrasound and MR imaging. *Phys Med Biol*. 2004;49(24):5529-5546. https://doi.org/10.1088/0031-9155/49/24/009.
7. Li W, Belmont B, Greve JM, et al. Polyvinyl chloride as a multimodal tissue-mimicking material with tuned mechanical and medical imaging properties. *J Med Phys*. 2016;43(10):5577-5592. https://doi.org/10.1118/1.4962649.
8. Goldstein D, Kundel H, Daube-Witherspoon M, Thibault L, Goldstein E. A silicone gel phantom suitable for multimodality imaging. *Invest Radiol*. 1987;22(2):153-157. https://doi.org/10.1097/00004424-198702000-00013.
9. Mazzara GP, Briggs RW, Wu Z, Steinbach BG. Use of a modified polysaccharide gel in developing a realistic breast phantom for MRI. *Magn Reson Imaging*. 1996;14(6):639-648. https://doi.org/10.1016/0730-725X(96)00054-9.
10. Abe K, Taira T. Focused ultrasound treatment, present and future. *Neurol Med Chir*. 2017;57(8):386-391. https://doi.org/10.2176/nmc.ra.2017-0024.
11. Duc NM, Keserci B. Emerging clinical applications of high-intensity focused ultrasound. *Diagn Interv Radiol*. 2019;25(5):398-409. https://doi.org/10.5152/dir.2019.18556.
12. Izadifar Z, Izadifar Z, Chapman D, Babyn P. An introduction to high intensity focused ultrasound: systematic review on principles, devices, and clinical applications. *J Clin Med*. 2020;9(2):460. https://doi.org/10.3390/jcm9020460.

13. King RL, Herman BA, Maruvada S, Wear KA, Harris G. Development of a HIFU phantom. *AIP Conf Proc*. 2007;911:351-356. https://doi.org/10.1063/1.2744296.
14. Menikou G, Damianou C. Acoustic and thermal characterization of agar based phantoms used for evaluating focused ultrasound exposures. *J Ther Ultrasound*. 2017;5:1-14. https://doi.org/10.1186/s40349-017-0093-z.
15. Hernando CG, Esteban L, Cañas T, Van Den Brule E, Pastrana M. The role of magnetic resonance imaging in oncology. *Clin Transl Oncol*. 2010;12(9):606-613. https://doi.org/10.1007/s12094-010-0565-x.
16. Rieke V, Pauly KB. MR thermometry. *J Magn Reson Imaging*. 2008;27(2):376-390. https://doi.org/10.1002/jmri.21265.MR.
17. Hadjisavvas V, Ioannides K, Komodromos M, Mylonas N, Damianou C. Evaluation of the contrast between tissues and thermal lesions in rabbit in vivo produced by high intensity focused ultrasound using fast spin echo MRI sequences. *J Biomed Sci Eng*. 2010;4(1):51-61. https://doi.org/10.4236/jbise.2011.41007.
18. Eranki A, Farr N, Partanen A, et al. Mechanical fractionation of tissues using microsecond-long HIFU pulses on a clinical MR-HIFU system. *Int J Hyperthermia*. 2019;34(8):1213-1224. https://doi.org/10.1080/02656736.2018.1438672.
19. Waspe AC, Looi T, Mougenot C, et al. Dynamic T 2 -mapping during magnetic resonance guided high intensity focused ultrasound ablation of bone marrow. *AIP Conf Proc*. 2012;1503(1):222-226. https://doi.org/10.1063/1.4769948.
20. Lafon C, Zderic V, Noble ML, et al. Gel phantom for use in high-intensity focused ultrasound dosimetry. *Ultrasound Med Biol*. 2005;31(10):1383-1389. https://doi.org/10.1016/j.ultrasmedbio.2005.06.004.
21. Smith RF, Rutt BK, Holdsworth DW. Anthropomorphic carotid bifurcation phantom for MRI applications. *J Magn Reson Imaging*. 1999;10(4):533-544. https://doi.org/10.1002/(sici)1522-2586(199910)10:4<533::aid-jmri6>3.0.co;2-z.
22. Chen Y, Lee GR, Aandal G, et al. Rapid volumetric T1 mapping of the abdomen using 3D through-time spiral GRAPPA. *Magn Reson Med*. 2017;75(4):1457-1465. https://doi.org/10.1002/mrm.25693.
23. Li Q, Cao X, Ye H, Liao C, He H, Zhong J. Ultrashort echo time magnetic resonance fingerprinting (UTE - MRF) for simultaneous quantification of long and ultrashort T2 tissues. *Magn Reson Med*. 2019;82:1359-1372. https://doi.org/10.1002/mrm.27812.
24. Nezafat M, Botnar M. Imaging sequence for joint myocardial T1 mapping and fat/water separation. *Magn Reson Med*. 2019;81(1):486-494. https://doi.org/10.1002/mrm.27390.
25. Mitchell MD, Kundel HL, Axel L, Joseph PM. Agarose as a tissue equivalent phantom material for NMR imaging. *Magn Reson Imaging*. 1986;4(3):263-266. https://doi.org/10.1016/0730-725X(86)91068-4.
26. Altermatt A, Santini F, Deligianni X, et al. Design and construction of an innovative brain phantom prototype for MRI. *Magn Reson Med*. 2019;81(2):1165-1171. https://doi.org/10.1002/mrm.27464.
27. De Brabandere M, Kirisits C, Peeters R, Haustermans K, Van den Heuvel F. Accuracy of seed reconstruction in prostate postplanning studied with a CT- and MRI-compatible phantom. *Radiother Oncol*. 2006;79(2):190-197. https://doi.org/10.1016/j.radonc.2006.04.009.
28. Partanen A, Mougenot C, Vaara T. Feasibility of agar-silica phantoms in quality assurance of MRgHIFU. *AIP Conf Proc*. 2009;1113:296-300. https://doi.org/10.1063/1.3131434.
29. Menikou G, Dadakova T, Pavlina M, Bock M, Damianou C. MRI compatible head phantom for ultrasound surgery. *Ultrasonics*. 2015;57(C):144-152. https://doi.org/10.1016/j.ultras.2014.11.004.
30. Menikou G, Yiannakou M, Yiallouras C, Ioannides C, Damianou C. MRI-compatible bone phantom for evaluating ultrasonic thermal exposures. *Ultrasonics*. 2016;71:12-19. https://doi.org/10.1016/j.ultras.2016.05.020.

31. Pichardo S, Melodelima D, Curiel L, Kivinen J. Suitability of a tumour-mimicking material for the evaluation of high-intensity focused ultrasound ablation under magnetic resonance guidance. *Phys Med Biol*. 2013;58(7):2163-2183. https://doi.org/10.1088/0031-9155/58/7/2163.

32. Rickey DW, Picot PA, Christopher DA, Fenster A. A wall-less vessel phantom for Doppler ultrasound studies. *Ultrasound Med Biol*. 1995;21(9):1163-1176. https://doi.org/10.1016/0301-5629(95)00044-5.

33. Christoffersson JO, Olsson LE, Sjöberg S. Nickel-doped agarose gel phantoms in MR imaging. *Acta Radiologica*. 1991;32(5):426-431. https://doi.org/10.3109/02841859109177599.

34. Bojorquez JZ, Bricq S, Acquitter C, Brunotte F, Walker PM, Lalande A. What are normal relaxation times of tissues at 3 T? *Magn Reson Imaging*. 2017;35(2017):69-80. https://doi.org/10.1016/j.mri.2016.08.021.

35. Drakos T, Giannakou M, Menikou G, Ioannides C, Damianou C. An improved method to estimate ultrasonic absorption in agar-based gel phantom using thermocouples and MR thermometry. *Ultrasonics*. 2020;103. https://doi.org/10.1016/j.ultras.2020.106089.

36. Huber JS, Peng Q, Moses WW. Multi-modality phantom development. *IEEE Trans Nucl Sci*. 2009;56(5):2722-2727. https://doi.org/10.1109/TNS.2009.2028073.

37. Bottomley PA, Foster TH, Argersinger RE, Pfeifer LM. A review of normal tissue hydrogen NMR relaxation times and relaxation mechanisms from 1–100 MHz: dependence on tissue type, NMR frequency, temperature, species, excision, and age. *Med Phys*. 1984;11(4):425-448. https://doi.org/10.1118/1.595535.

38. Stanisz GJ, Odrobina EE, Pun J, et al. $T1$, $T2$ relaxation and magnetization transfer in tissue at 3T. *Magn Reson Med*. 2005;54(3):507-512. https://doi.org/10.1002/mrm.20605.

39. Matzat SJ, McWalter EJ, Kogan F, Chen W, Gold GE. $T2$ relaxation time quantitation differs between pulse sequences in articular cartilage. *J Magn Reson Imaging*. 2015;42(1):105-113. https://doi.org/10.1002/jmri.24757.

40. Kjaer L, Henriksen O. Comparison of different pulse sequences for in vivo determination of $T1$ relaxation times in the human brain. *Acta Radiol*. 1988;29(2):231-236.

41. Fatemi Y, Danyali H, Helfroush MS, Amiri H. Fast $T2$ mapping using multi-echo spin-echo MRI: a linear order approach. *Magn Reson Med*. 2020;84:2815-2830. https://doi.org/10.1002/mrm.28309.

42. Antoniou A, Damianou C. MR relaxation properties of tissue-mimicking phantoms. *Ultrasonics*. 2022;119.

ORIGINAL ARTICLE

The International Journal of **Medical Robotics** and **Computer Assisted Surgery**

WILEY

Robotic system for top to bottom MRgFUS therapy of multiple cancer types

Anastasia Antoniou[1] | Marinos Giannakou[2] | Nikolas Evripidou[1] |
Stylianos Stratis[1] | Samuel Pichardo[3] | Christakis Damianou[1]

[1]Department of Electrical Engineering, Computer Engineering, and Informatics, Cyprus University of Technology, Limassol, Cyprus

[2]R&D, Medsonic Ltd, Limassol, Cyprus

[3]Hotchkiss Brain Institute, Cumming School of Medicine, University of Calgary, Calgary, Alberta, Canada

Correspondence
Christakis Damianou, Department of Electrical Engineering, Computer Engineering, and Informatics, Cyprus University of Technology, 30 Archbishop Kyprianou St, Limassol 3036, Cyprus.
Email: christakis.damianou@cut.ac.cy

Abstract

Background: A robotic system for Magnetic Resonance guided Focussed Ultrasound (MRgFUS) therapy of tumours in the breast, bone, thyroid, and abdomen was developed.

Methods: A special C-shaped structure was designed to be attached to the table of conventional magnetic resonance imaging (MRI) systems carrying 4 computer-controlled motion stages dedicated to positioning a 2.75 MHz spherically focussed transducer relative to a patient placed in the supine position. The developed system was evaluated for its MRI compatibility and heating abilities in agar-based phantoms and freshly excised tissue.

Results: Compatibility of the system with a clinical high-field MRI scanner was demonstrated. FUS heating in the phantom was successfully monitored by magnetic resonance thermometry without any evidence of magnetically induced phenomena. Cigar-shaped discrete lesions and well-defined areas of overlapping lesions were inflicted in excised tissue by robotic movement along grid patterns.

Conclusions: The developed MRgFUS robotic system was proven safe and efficient by *ex-vivo* feasibility studies.

KEYWORDS
ex vivo tissue ablation, focussed ultrasound, MRI compatible, multipurpose, robotic system, top to bottom

1 | INTRODUCTION

Robotics has gained a prominent role in modern oncology and has been essential in translating new therapeutic modalities to the clinical setting.[1] Accordingly, robotic devices are increasingly being developed for manipulating surgical instruments and energy sources, providing the accuracy required for safe clinical applications.[1] Simultaneously, in recent years, a shift has been observed towards minimally invasive and non-invasive therapeutic solutions, with the Focussed Ultrasound (FUS) technology continuously gaining

prevalence as a non-invasive alternative to surgery for many oncological and other applications.[2,3] The non-invasive nature of FUS along with the increased accuracy offered by robotic guidance promise to minimize all the complications and side effects of traditional surgery, thus greatly improving the life quality of patients. Please refer to Table 1 for the list of abbreviations used in the paper.

FUS constitutes a completely non-invasive technology where ultrasonic waves are focussed on the targeted anatomy percutaneously, inducing thermal and mechanical effects.[3] The most common mechanical bioeffect of FUS is known as cavitation and refers to the

TABLE 1 Complete list of abbreviations used throughout the paper

Abbreviation	Definition
MRgFUS	Magnetic resonance guided focussed ultrasound
MRI	Magnetic resonance imaging
FDA	Food and Drug Administration
DOF	Degrees of freedom
ABS	Acrylonitrile butadiene styrene
HIFU	High intensity focussed ultrasound
SNR	Signal to noise ratio
SI	Signal intensity
ROI	Region of interest
SPGR	Spoiled Gradient Echo
TR	Repetition time
TE	Echo time
FOV	Field of view
NEXs	Number of excitations
PRF	Proton resonance frequency
ASTM	American Society for Testing and Materials

tissue damage caused by gas microbubbles oscillating within the acoustic field.[3] In terms of thermal effects, during high-power FUS, intensive heat is produced by absorption of acoustic energy, thereby increasing the local tissue temperature.[4] Typically, temperature elevation of more than 60°C for 1 s causes instantaneous death of cells mainly via coagulation mechanisms.[4] The thermal effects of FUS were widely exploited in oncology,[3] with the progress in the field being remarkably boosted by the introduction of magnetic resonance imaging (MRI) as the guidance modality, especially through the use of MR thermometry that offers procedural monitoring of heating.[5] Simultaneously, MRI is ideal for high-resolution imaging and delineation of anatomy.[6]

One of the earliest manufacturers of clinical Magnetic Resonance guided Focussed Ultrasound (MRgFUS) devices with marketing activities in Europe, America, and Asia is the Insightec Company that owns the well-known ExAblate body system.[7] The Profound company constitutes another successful company in the field owning the Sonalleve system that is also intended for body targets.[8] The treatment of uterine fibroids and pain palliation of bone metastasis are two of the most widely applied Food and Drug Administration (FDA) approved applications of both systems.[9] Their mechanical and ultrasonic components are arranged into an opening of the MRI bed offering bottom to top ultrasonic delivery by electronically steering the beam using phased array technology.[7,8] Such a therapeutic approach forces the patient in the prone position. Although this is a conventional position in many surgical interventions, it is very uncomfortable and tiring for patients, given

that FUS procedures typically last long and patients may be awake (or sedated) depending on the condition being treated. This feeling is enhanced by the limited enclosed space of the scanner, especially for claustrophobic patients.

The aforementioned limitation can be addressed by positioning the ultrasonic source above the patient so that supine positioning is allowed. Thereby, several manufacturers proceed to the development of products that use a top to bottom therapeutic approach enabling supine placement of patients.[9-14] Commercially available systems are listed in Table 2. Most of them use the same principle of guidance and treatment with a positioning arm navigating the diagnostic and therapeutic equipment relative to the target.[10-13] Typically, this arm is integrated into a transportable platform that includes the hardware for monitoring of therapy by the physician through computer-based treatment programs.[10-13] In other systems, separate platforms are dedicated for US imaging guidance and remote system control, whereas the treatment head is located above or/and below the treatment bed.[9,14] Multi-element array ultrasonic technology is typically employed for precise beam focussing,[9,10,14] as well as for maintaining the acoustic intensity at the skin surface within the permitted limits to avoid pain and skin burns.[9]

Meanwhile, efforts are continuing by the research community with the aim to develop more advanced systems in the field. Tognarelli et al.[15] developed a platform for robotic-assisted FUS treatment of various pathologies under US monitoring, where the robotic module is composed of two manipulators, each featuring motion in 6 degrees of freedom (DOF). The first manipulator incorporates a custom-made phased annular array transducer and a 2D imaging US probe, whereas the second one includes a 3D imaging US probe.

An MR-conditional robot was developed by Price et al.[16] for the purpose of FUS therapy through intact skull in infants. A clinical FUS transducer of 1.2 MHz nominal frequency serves as the robot's end-effector. The mechanism comprises three prismatic joints offering translational movement in three orthogonal axes and two revolute joints enabling rotation of the robot's wrist for positioning the source about the skull. Although the system was designed for MR-guided procedures exploiting the unique capabilities of MRI, it is cited on the MRI table, further reducing the constricted space of the scanner.

It is interesting to mention that Yiannakou et al.[17] modified an already existing MRgFUS system originally developed to be cited on the MRI table for bottom to top and lateral approaches in order to enable top to bottom access of ultrasound to the target. An MR compatible arm was attached to the mechanism to raise the transducer at sufficient height from the MRI table. Accordingly, a height adjustment mechanism was developed for positioning a water bag at various vertical locations so that acoustic coupling with the target is achieved. This may be considered a feasibility study since authors did not proceed to the development of a complete robotic system.

T A B L E 2 Commercial systems for top to bottom US-guided FUS therapy

Company	System	Approval	Application	Main features	Ref.
Alpinion Medical Systems (United States)	ALPIUS 900	CE mark (2016)	Uterine fibroids	6 DOF positioning arm	10
				US imaging/treatment head	
				Multichannel FUS transducer	
				Water circulation/Coupling module	
				Mobile platform	
	VIFU 2000	-	Laboratory research in small animals	3 DOF positioning arm	11
				US imaging/treatment head	
				Compact design	
Theraclion company (France)	SONOVEIN	CE mark (2019)	Varicose veins	Positioning arm	12
				Rotating US imaging/treatment head	
				Single element FUS transducer	
				Coupling/cooling liquid system	
				Mobile platform	
	ECHOPULSE	CE mark (2007/2012)	Thyroid nodules/Breast fibroadenoma	6 DOF positioning arm	13
				4 DOF US imaging/treatment head	
				Coupling/Cooling liquid system	
				Mobile platform	
Shanghai A&S Technology Development (China)	HIFUNIT 9000	CE mark (2008)	Uterine fibroids	3D movement therapy bed	14
				Gantry with multi-axis treatment head	
				Multi-array FUS technology	
				US imaging guidance platform	
Beijing Yuande Bio-Medical Engineering (China)	FEP-BY02	China and Korea (1999+)	Oncology (e.g., liver, pancreas, kidney)	Treatment bed with upper and lower therapeutic transducers	9
				Multi-array FUS technology	
				US imaging guidance platform	

Abbreviations: DOF, degrees of freedom; FUS, Focussed Ultrasound.

Herein, the developed technology relates to a transportable MRgFUS robotic system designed for treating patients in the supine position. In contrast to the aforementioned US-guided systems, the proposed one can safely operate in the MRI environment allowing therapy under real-time MR thermometry. The unique design of the system enables top to bottom access to multiple body locations while the patient is lying in the supine position, and thus, it is superior to systems that are cited on the MRI table.

The proposed system comprises a C-shaped mounting structure that carries the positioning and therapeutic equipment and can be attached to the table of any conventional MR scanner. The positioning mechanism includes four PC-controlled motion stages, piezoelectric actuators, and optical encoders for accurate positioning of a single element spherically focussed transducer relative to the patient. Notably, the mechanical components were assembled in a space-saving manner to leave sufficient space underneath the C-arm for the patient. Overall, the prototype has a commercial ready design. Its performance was assessed in terms of MRI compatibility and

thermal heating capabilities by preclinical studies in tissue mimicking phantoms (TMPs) and freshly excised tissue.

2 | MATERIALS AND METHODS

2.1 | Description of the robotic system

2.1.1 | Main features

An MRgFUS robotic system designed to destroy tumours in the bone, breast, abdomen (e.g., kidney, liver, pancreas) and thyroid is presented. The robotic mechanism that carries the ultrasonic source is placed above the patient with the assistance of a C-arm specially designed to fit in any conventional MRI system making the system universal. Therefore, access of ultrasound to the targeted area is achieved from top to bottom. The concept of treatment is shown in Figure 1.
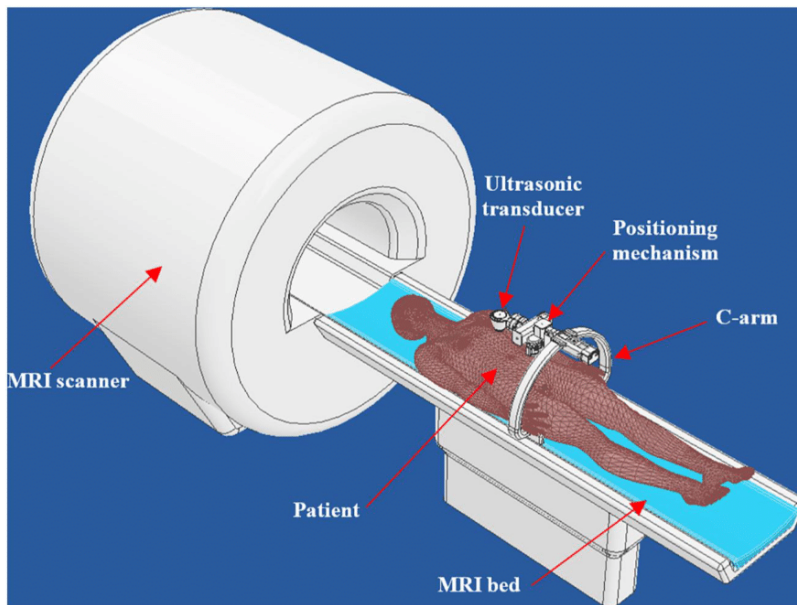
29

FIGURE 1 Concept of treatment. Computer-aided design drawing of the 4 degrees of freedom robotic device attached to the magnetic resonance imaging bed with the patient placed in the supine position

The robotic system employs components that can function inside the MRI environment, such as ultrasonic motors, brass screws, and Acrylonitrile butadiene styrene (ABS) plastic structures. The robotic mechanism features motion in four PC-controlled axes. The Z-stage moves forward and reverse, the Y stage moves up and down, and the X-stage moves left and right, with motion ranges of 73 mm, 49 mm, and 73 mm, respectively. The Θ-stage rotates the transducer about an axis parallel to the Z-axis covering an overall angle of 180 °.

MRI compatible ultrasonic motors (USR30-S3; Shinsei Kogyo Corp.) actuate motion with minimal effect on the signal of the scanner. Highly accurate motion is achieved through the use of MRI compatible optical encoders (linear motion: EM1-0-500-I, angular motion: EM1-2-2500-I; US Digital Corporation). In this regard, specific techniques were implemented, including the incorporation of double-sided guides and brass screws, thereby increasing the robustness and achieving a stable and perfectly aligned robotic movement.

2.1.2 | Design details and principle of motion

The Z-stage of the positioning mechanism is shown in Figure 2A. The moving parts were assembled inside the Z-frame. The Z-motor holder was attached to the rear of the Z-frame. The Z-motor was fixed in the holder and secured by the Z-motor cover. During operation, the rotational motion of the motor is converted into linear motion of the Z-plate inside the respective guide slots of the Z-frame through a jack-screw mechanism. The Z-rectangular shaft moves inside the respective guide of the Z-frame for smooth and stable linear motion in the Z-axis. The rear end of the Z-rectangular shaft was attached to the Z-plate while on its front end a coupling was included for the Y-stage. On each side of the Z-frame there are couplings for attaching the device to the MRI bed via a C-arm.

Accurate motion in the Z-axis is achieved through the use of an optical encoder setup. The optical encoder module was mounted on the Z-plate to move along the respective encoder strip with a resolution of 500 lines per inch, which was attached to the Z-frame. The Z-encoder and Z-motor connectors (4-pin, Fischer) were fixed between the Z-motor holder and the Z-motor cover at the rear of the stage.

Figure 2B shows the Y-stage. The Y-stage was connected with the Z-rectangular shaft to be carried by the Z-stage. The Y-motor was attached to the side part of the Y-frame and merged with the pinion gear that was in turn coupled to the idler gear. Accordingly, the idler gear was coupled to the spur gear that rotates the Y-jackscrew. Similar to Z-stage, the Y-jackscrew was coupled to the Y-plate for converting the angular into linear motion. Monitoring of motion is achieved with an optical encoder system identical to that of the Z-stage.

The X-stage was attached to the Y-stage via a coupling and screws. The assembly of the X-stage is shown in Figure 2C. The motion mechanism of the X-stage uses the same jackscrew principle described previously for the other two stages. In fact, the X-plate was coupled to the X-jackscrew to move within the respective guides of the X-frame. Furthermore, special guides were designed on the X-plate for installing the Θ-stage. Similar to the Z-stage and Y-stage, an optical encoder setup of the same type was incorporated for motion control.

Figure 2D shows the assembly of the Θ-stage that carries the ultrasonic source. The Θ-motor was coupled to a two-stage gear speed reduction mechanism. The speed reduction mechanism amplifies the torque of the Θ-motor helping it to overcome the increased load when during treatment the coupling system is filled with degassed water. The gear ratio of each stage of 1:3 results in a total gear ratio of 1:9. For precise rotation, an angular encoder
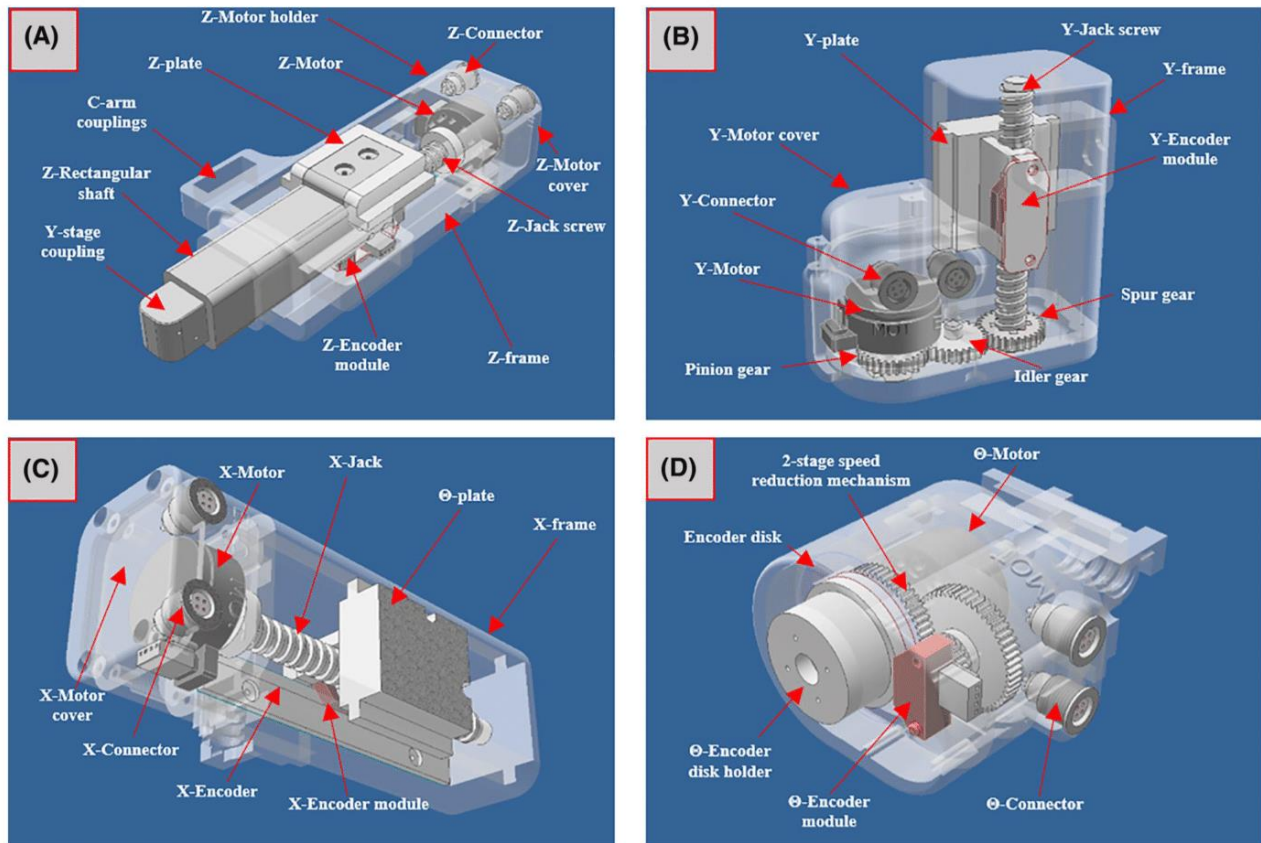
FIGURE 2 Assembly of the (A) Z-stage, (B) Y-stage, (C) X-stage, and (D) Θ-stage

module was installed on the mechanism. The respective optical encoder disk has a resolution of 2500 lines per 360°.

The fully assembled robotic device is shown in Figure 3. The ultrasonic transducer was attached at the front of the Θ-stage via the Θ-arm while being connected to a coupling cone. Upon operation, this cone is filled with degassed water enabling proper transmission of the ultrasonic beam through an opening at its bottom that is sealed with a membrane. It is noted that acoustic coupling membranes are commonly used in MRgFUS systems usually being part of the transducer assembly.[18] In the current study, the membrane was made of silicone with a mean acoustic attenuation of 1.58 ± 0.20 dB/cm-MHz (at 1.1 MHz). Given its very small thickness of 0.2 mm, the induced attenuation of the ultrasonic beam is considered minimal. This membrane is in contact with the skin through a layer of coupling gel to ensure good contact with tissue. Furthermore, the coupling cone includes two brass fittings that are connected to a pump to circulate degassed water, thus cooling the transducer element during high power sonications. The Z-stage carrying the rest of the mechanism is attached to the C-arm via two couplings. The C-arm connects to the respective C-arm bases that are mounted on opposite sides of the MRI table allowing the patient to be placed comfortably under the device in the supine position for a top to bottom access of ultrasound to the targeted area.

2.1.3 | High intensity FUS system

The therapeutic transducer was developed in-house using non-magnetic materials with the proper characteristics as estimated by simulation studies in order to achieve optimal focussing at sufficient depth in tissue. The transducer was designed using a single piezoelectric element so as to be compact and ergonomic. An element with a nominal frequency of 2.75 MHz, diameter of 50 mm, and a radius of curvature of 65 mm was housed in a custom-made case made of ABS plastic. The transducer is activated by a tuned RF amplifier (AG1016, AG Series Amplifier, T & C Power Conversion, Inc.) for maximum power gain. The achieved average efficiency amounts to 30%.

2.1.4 | Controlling software

Remote control of the system is accomplished through an in-house software written in C sharp (Visual Studio 2010 Express; Microsoft Corporation). The main functionalities of the software relate to controlling the High Intensity Focussed Ultrasound (HIFU) and robotic positioning systems. Control algorithms were implemented for selecting the transducer's path by specifying the parameters of grid
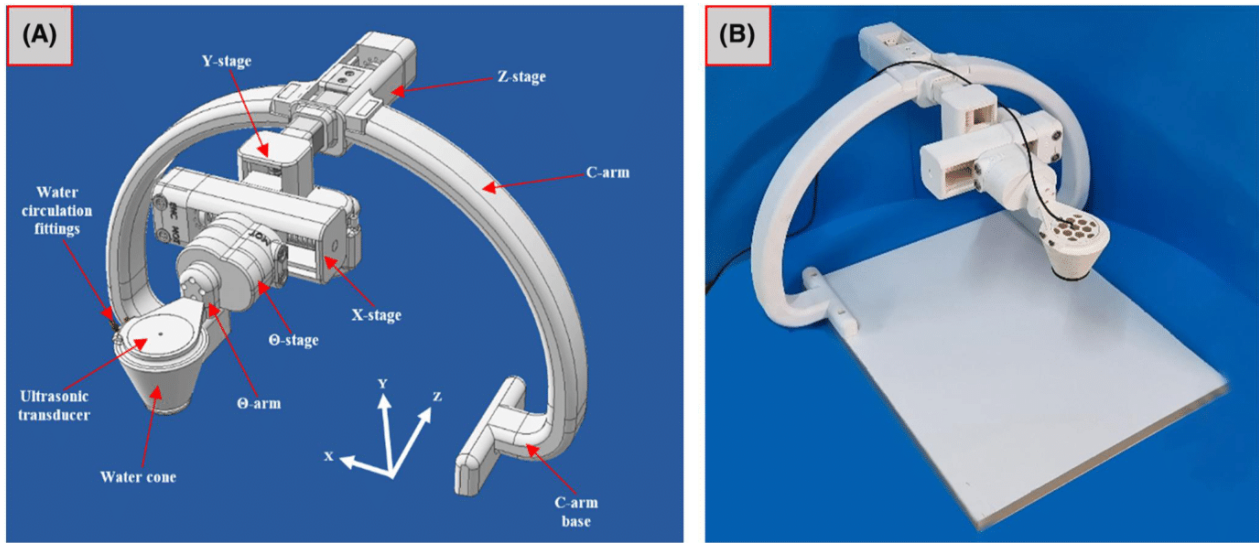
FIGURE 3 (A) Computer-aided design drawing of the robotic device indicating the main components and (B) Photo of the manufactured device

operation, including the grid size, motion pattern, spatial step, and time delay between successive sonications, and sending the relevant commands to an electronic driving system that was developed in-house. The user is also allowed to control the ultrasonic exposure by selecting operating frequency, continuous or pulse mode, power, pulse duration, pulse repetition frequency, and number of exposures. Furthermore, the software was interfaced with the MRI enabling real time transfer and display of MR images and the use of MR thermometry tools during HIFU.

2.2 | Evaluation of system's performance

2.2.1 | MRI compatibility

The system's components intended to operate in the MRI room were entirely manufactured from non-magnetic materials for safety reasons. Upon full implementation of the system, its compatibility with a clinical MRI scanner was assessed using a signal to noise ratio (SNR) methodology. The method was based on comparing the SNR of MR images acquired under different activation states of the robotic system. For this purpose, an agar based TMP was sequentially imaged upon activating different system's components. The SNR was calculated by including the mean signal intensity of a Region of Interest (ROI) in the phantom and a background ROI in the following equation:

$$SNR = \frac{SI_{phantom}}{\sigma_{noise}} \qquad (1)$$

where the denominator represents the standard deviation from the ROI placed in the air/background. It is noted that the noise was assumed to follow a Gaussian distribution.

The agar-based phantom was prepared with 6% weight per volume (w/v) agar (Merck KGaA; EMD Millipore Corporation) according to a procedure previously described in the literature.[19] The selection of agar as the gelling agent was based on several factors such as the ease and low cost preparation process of agar-based phantoms, as well as their tissue-like MRI signal.[20] It is noted that during phantom production, the mixture was carefully dissolved with continuous agitation in order to form a homogeneous phantom offering image homogeneity in MRI. The robotic device was placed on the couch of a 1.5 T MRI scanner (GE Signa HD16; General Electric) and the coupling cone was filled with degassed water for proper ultrasonic coupling with the phantom. MRI scans of the phantom were performed using a body coil (Signa 1.5T 12 Channel; GE Healthcare Coils) and a common Spoiled Gradient Echo (SPGR) sequence.

The MRI compatibility of the robotic device was initially evaluated by measuring the SNR of the phantom using the SPGR sequence with the following MR parameters: repetition time (TR) = 22 ms, echo time (TE) = 10.5 ms, field of view (FOV) = 28 × 28 cm^2, matrix = 192 × 160, flip angle = 30° and number of excitations (NEXs) = 2. Similarly, MRI compatibility assessment of the transducer and MR thermometry were performed by comparing 2D SPGR images acquired using the following parameters: TR = 22 ms, TE = 8.4 ms, FOV = 28 × 28 cm^2, matrix = 192 × 160, flip angle = 30° and NEXs = 2.

2.2.2 | MR thermometry

An agar-based phantom containing 6% w/v agar and 4% w/v silica (Sigma-Aldrich) was sonicated by applying an electrical power of 150 W (acoustical power 45 W) for 35 s at a focal depth of 2.3 cm. It should be noted that the high melting point of agar makes this

phantom suitable for HIFU exposures.[20] The temperature evolution during heating was monitored using MR thermometry. Specifically, the change of temperature was estimated using a technique known as the proton resonance frequency (PRF) shift method.[5] The method takes advantage of the temperature-dependent change of the PRF in tissue. The phase difference between a baseline image acquired before heating $\varphi(T_0)$ (at a known temperature) and an image acquired at a specific time during heating $\varphi(T)$ is proportional to the corresponding PRF change, and thus, it can be easily converted to temperature change as follows:[5]

$$\Delta T = \frac{\varphi(T) - \varphi(T_0)}{\gamma \alpha B_0 TE} \qquad (2)$$

where γ is the gyromagnetic ratio, α is the PRF change coefficient, B_0 is the magnetic field strength, and TE is the echo time.

In accordance, the temperature change in a specific phantom ROI was derived from phase difference calculations in a pixel-by-pixel basis. The relevant data were extracted from 2D SPGR images. The scans were performed using the general-purpose flex surface coil (Signa 1.5T Receiver only; GE Medical Systems. The images acquired during heating were processed by the developed software using a series of libraries written in the Python language (Proteus MRI-HIFU Software Development Suite), which allowed for controlled exposure through MR-based thermometry. Thermal maps were produced at a specific temporal step according to the previously described method.[5] The estimated temperature values were colour-coded by adjusting a colour map from blue to red.

2.2.3 | Grid ablation on excised tissue

After confirming proper operation in the MRI setting, the feasibility of the system in producing thermal lesions was examined by performing high power sonications on freshly excised tissue. The distance between the transducer and the tissue was set at 4 cm resulting in a focal depth of 2.5 cm (given the radius of curvature of 65 mm). The transducer was moved along grid patterns using the software commands. Grid ablations were performed automatically based on predefined protocols while the grid operation was being displayed on the screen and monitored by the user. A 3×3 grid was selected for the experiments while the spatial step was varied. A time delay of 60 s was used between successive sonications.

3 | RESULTS

3.1 | MRI compatibility

MRI compatibility assessment was performed by comparing the SNR of 2D SPGR coronal images of an agar-based phantom at different activation conditions of the system. Regarding the MRI compatibility of the robotic mechanism, Figure 4 shows MR images acquired with the cables disconnected, cables connected, electronic system connected, electronic system activated, and motor moving. Figure 5 shows a bar chart of the measured SNR for each condition tested. Accordingly, Figure 6 shows the MR images acquired under different activation states of the transducer while Figure 7 shows a bar chart of the corresponding SNR measurements.

3.2 | MR thermometry

Thermal maps were generated at temporal step of 7 s.[5] Figures 8A and 8B show the thermal maps acquired at 35 s of sonication (acoustical power of 150 W) in a plane perpendicular (coronal) and parallel (axial) to the ultrasonic transmission, respectively, indicating a temperature change at the focus of about 50°C.

3.3 | Grid ablation on excised tissue

Multiple sonications were performed in freshly excised tissue using grid operation. An acoustical power of 150 W was applied for 20 s at each point of a 3×3 grid (60 s time delay). A spatial step of 15 mm resulted in nine well-formed discrete lesions on tissue. The tissue was cut horizontally (in a plane perpendicular to the beam) at a depth of 2 cm revealing well-defined circle-shaped lesions with a mean diameter of 7.44 ± 1.74 mm, as shown in Figure 9. Figure 10 shows discrete thermal lesions formed using a quite shorter sonication time of 10 s. The tissue was cut vertically to reveal the length of the lesions. The same sonication protocol (150 W for 10 s) but three times smaller spatial step resulted in the overlapping lesions illustrated in Figure 11. The tissue was cut horizontally at 1.5 cm from the sonicated surface. A well-defined coagulative area of about 14 mm in diameter was formed.

4 | DISCUSSION

A transportable robotic system that comprises a C-shaped holder intended to be attached to the MRI bed was developed. The holder carries a 4 DOF positioning mechanism dedicated to manoeuvring a custom-made ultrasonic transducer of 2.75 MHz relative to the patient. The smart design of the device enables treatment of bone, breast, thyroid, and abdominal tumours while the patient is comfortably lying in the supine position.

Motion in all incorporated axes is actuated by piezoelectric motors. Linear motion is established by jackscrew mechanisms that convert the rotational motion of the motors into translation motion of special plates along the respective jackscrews. A smooth and accurate rotation is established through a series of speed reduction gears that amplifies the motors' torque. It is noted that the robotic system has a motion accuracy level comparable to previous versions[21-23] since it follows a similar principle of motion, according to simple accuracy assessment methods.[24]
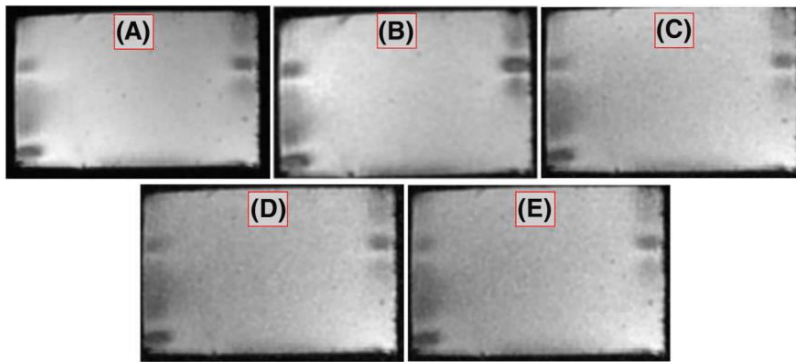
33

FIGURE 4 Coronal images acquired using 2D Spoiled Gradient Echo sequence with the (A) Cables disconnected, (B) Cables connected, (C) Electronic system connected, (D) Electronic system activated, and (E) Motor moving
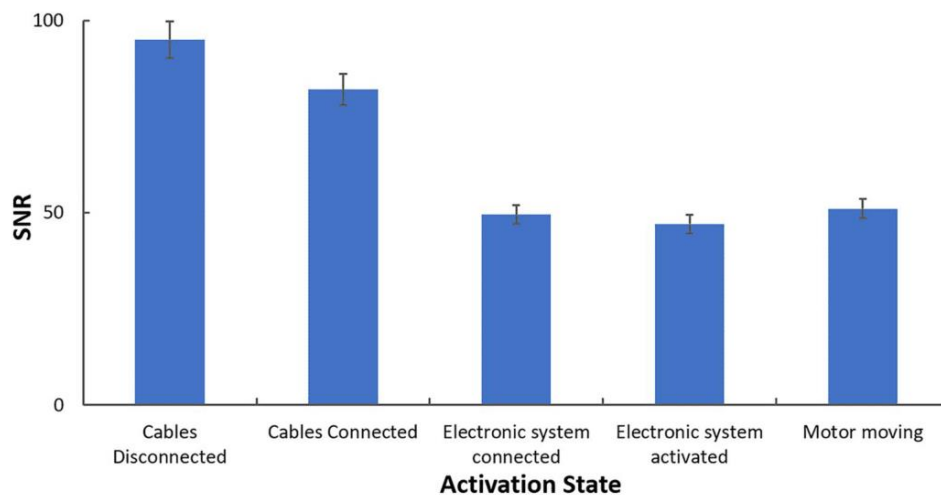

FIGURE 5 Signal to noise ratio (SNR) of the phantom images acquired at different activation states of the robot using the Spoiled Gradient Echo sequence
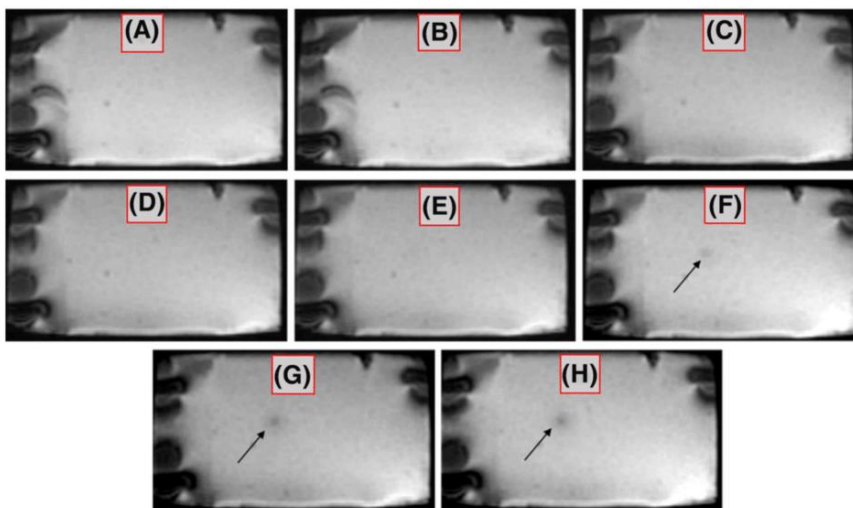

FIGURE 6 Coronal images acquired using 2D Spoiled Gradient Echo sequence under different activation conditions of the transducer: (A) Reference image, (B) Cables disconnected, (C) Cables connected, (D) Amplifier ON, and power set to (E) 50 W for 16 s, (F) 100 W for 16 s, (G) 150 W for 16 s, and (H) 200 W for 16 s

An optical encoder setup was installed on each stage providing precise position estimates, thereby ensuring highly accurate motion along the commanded path. In this regard, each stage was designed with double-sided guides to increase the motion and alignment accuracy, as well as the structural rigidity, also given that the load is increased when the coupling cone is filled with water. Advantageously, the various motion stages were assembled in space saving manner extending horizontally (along the Z-axis) to leave sufficient
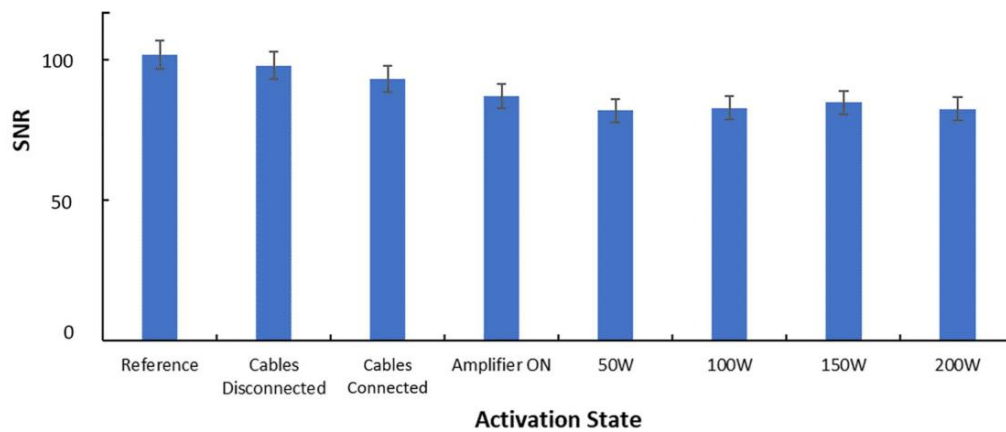
FIGURE 7 Signal to noise ratio (SNR) of the phantom images acquired at different activation states of the ultrasonic transducer using the Spoiled Gradient Echo sequence
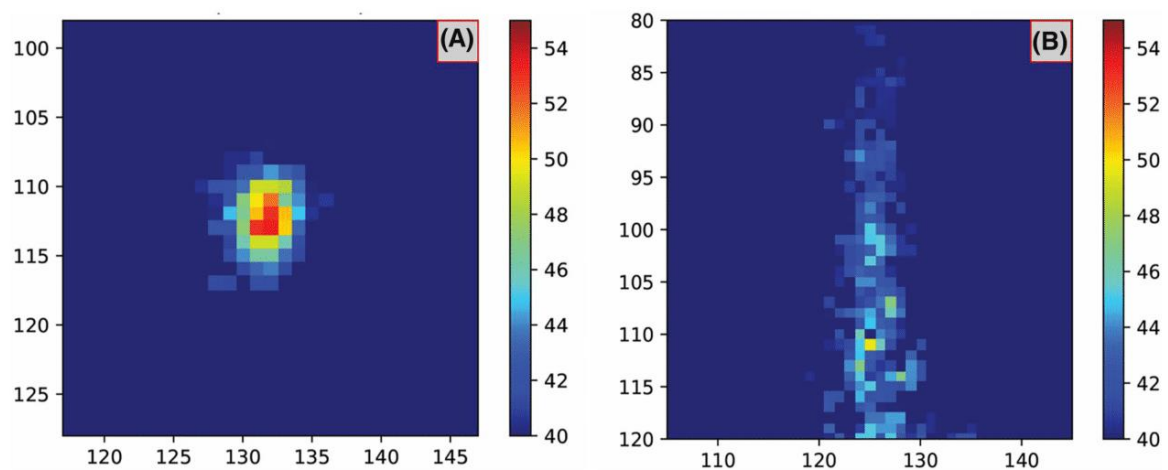
FIGURE 8 (A) Coronal and (B) Axial thermal maps acquired at 35 s of sonication (acoustical power of 150 W) in agar-based phantom

FIGURE 9 Excised tissue sliced horizontally at 2 cm depth showing discrete lesions formed after multiple sonications in a 3 × 3 grid with a 15 mm step and time delay of 60 s using 150 W acoustic power for 20 s at each spot (focal depth of 2.5 cm)

space under the system for comfortable supine positioning of the patient. Simultaneously, the specific configuration, as well as the rigidity of the structure, allow for more motion stages to be installed in the mechanism easily.

Remote control of the various functionalities of the system is achieved using the commands of a dedicated computer-controlled software. The user can define the therapeutic protocol and monitor

the overall procedure through a friendly graphical user interface without specific technical knowledge.

Once the hardware was developed and integrated with the corresponding software, the system was tested by benchtop and MRI experiments. Initially, the reference SNR was measured in the presence of the robot in the MRI scanner and proven sufficiently high for acquisition of high resolution SPGR images, thus demonstrating no
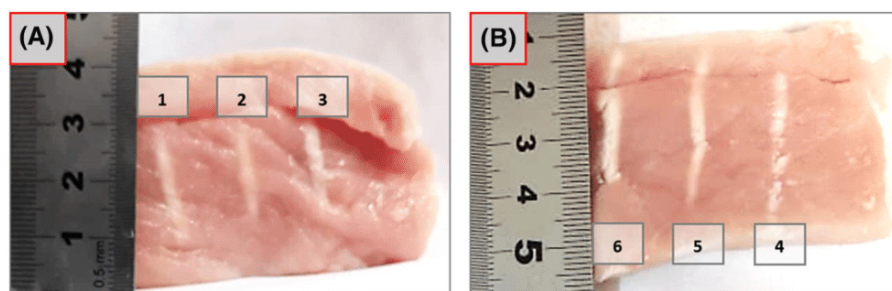
FIGURE 10 Excised tissue sliced vertically showing discrete cigar-shaped lesions formed after ablation in a 3 × 3 grid with a 15 mm step and time delay of 60 s using 150 W acoustic power for 10 s at each spot. Sonication spots: (A) 1, 2, 3, and (B) 4, 5, and 6
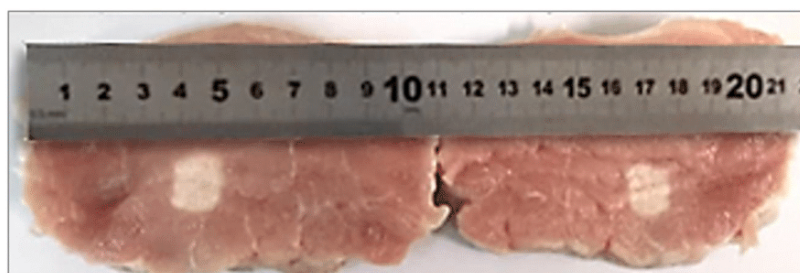

FIGURE 11 Excised tissue sliced horizontally at 1.5 cm depth showing overlapping lesions formed after ablation in 3 × 3 grid with a time delay of 60 s and 150 W for 10 s at each spot, but a smaller spatial step of 5 mm

interference between the system's materials and magnetic field that could compromise the imaging quality. Moreover, no noticeable artefacts were observed on MR images. Overall, the 3D printing plastic and non-magnetic materials used in the current system showed none or little reaction with the magnet minimally affecting the SNR and without causing any magnetically induced shift in the position of the various components.

A reduction of SNR was observed upon connection and activation of the system and transducer as expected. Despite the drop in the SNR, the image quality remained satisfactory with the focal spot being visible even during the highest power operation of 200 W. More importantly, the results suggest that MR thermometry can be performed properly using the specific sequence. In fact, the temperature evolution was successfully monitored, simultaneously demonstrating proper communication between hardware and software. Although the system can safely operate in the MRI environment without compromising the precision of ultrasound delivery, it is classified as MRI-conditional according to American Society for Testing and Materials standards (F2503) since it requires electricity to operate.

The heating abilities of the HIFU system were demonstrated by phantom experiments in the MRI setting. The temperature evolution during high power sonication in an agar-based phantom was successfully monitored using MR thermometry, which allowed for assessing destruction of the phantom's structure before dissection, simultaneously confirming the compatibility of the transducer with the MR scanner.

The feasibility of the system in performing grid ablations was then investigated by sonicating freshly excised tissue using robotic motion of the transducer along predefined grid patterns. Discrete and overlapping lesions were successfully created by adjusting the spatial step between adjacent sonications, demonstrating the ability of the system to produce thermal lesions in array patterns. The water system provided proper acoustic coupling and cooling of the transducer by water recycling with no evidence of overheating of the transducer element. These experiments also allowed for visually confirming high accuracy of robotic motion through the formation of equally spaced lesions, accounting though for tissue inhomogeneities. It was also demonstrated that the software controls the hardware and overall functions properly.

It is widely accepted that FUS therapy when combined with MRI guidance has the ability to ablate tumours with significantly higher precision and safety compared to US-guided procedures. In this regard, the proposed system aiming to fully exploit the unique benefits of MRI guidance is superior to commercial devices that use US guidance.[10–14] Furthermore, although previously proposed systems[21–23,25–28] can also operate in the MRI setting and could potentially be used for similar applications, more advances in terms of design and functionalities have seen the production of the one proposed herein.

Firstly, devices dedicated to be cited on the MRI table[21,25–27] occupy valuable space in the scanner while in some cases, the moving parts are being actuated in close proximity to the patient, possibly compromising the safety of the procedure. Other proposed devices[22,23] are characterized by a simplistic design with all the mechanical and ultrasonic components being installed in a compact housing that is incorporated into the patient's bed. The main limitation of this configuration is that it forces the patient in the prone position, whereas the current system allows comfortable supine positioning. It should also be noted that these devices are partially placed inside the bed with the housing protruding above it, thus occupying some of the already restricted space.

Overall, the systems proposed in the previously cited work may be considered simplistic versions of the presented one that provided proof of concept for the technology and principle of motion. Advantageously, the current device was optimized to meet the clinical requirement, with the prototype having proper size and features and offering sufficient motion range for applications in humans. So far, the system was validated for safety and efficacy by ex-vivo experimentation. However, its performance should be further evaluated by *ex-vivo* and *in-vivo* preclinical studies to obtain sufficient data for translating it to the clinic.

In conclusion, the developed MRgFUS system is simple in use and inexpensive compared to other systems using phased array multi-element technology. It offers excellent top to bottom coupling of ultrasound with the subject through a water-filled coupling cone, which also circulates water for cooling the transducer. The prototype could be easily translated to the clinic to offer an alternative non-invasive therapeutic solution for various cancer types since it already has a commercial ready design.

CONFLICT OF INTERESTS

Anastasia Antoniou declares no conflict of interest. Marinos Giannakou declares no conflict of interest. Nikolas Evripidou declares no conflict of interest. Stelios Stratis declares no conflict of interest. Samuel Pichardo declares no conflict of interest. Christakis Damianou declares no conflict of interest.

AUTHOR CONTRIBUTIONS

Anastasia Antoniou contributed to the drafting of manuscript. Marinos Giannakou contributed to the development of the robotic device. Nikolas Evripidou contributed to the development of the electronic system and software. Stelios Stratis contributed to the experiments in excised tissue. Samuel Pichardo contributed to the MRI experiments. Christakis Damianou supervised the development and evaluation of the robotic system, as well as the drafting of the manuscript.

DATA AVAILABILITY STATEMENT

The data that support the findings of this study are available from the corresponding author upon reasonable request.

ORCID

Marinos Giannakou https://orcid.org/0000-0002-6777-0515
Nikolas Evripidou https://orcid.org/0000-0002-8200-3349
Christakis Damianou https://orcid.org/0000-0003-0424-2851

REFERENCES

1. Peters BS, Armijo PR, Krause C, Choudhury SA, Oleynikov D. Review of emerging surgical robotic technology. *Surg Endosc.* 2018;32(4):1636-1655. https://doi.org/10.1007/s00464-018-6079-2

2. Duc NM, Keserci B, Keserci B. Emerging clinical applications of high-intensity focused ultrasound. *Diagnostic Interv Radiol.* 2019;25(5):398-409. https://doi.org/10.5152/dir.2019.18556

3. Izadifar Z, Izadifar Z, Chapman D, Babyn P. An introduction to high intensity focused ultrasound: systematic review on principles, devices, and clinical applications. *J Clin Med.* 2020;9(2):460. https://doi.org/10.3390/jcm9020460

4. Zhou Y. High intensity focused ultrasound in clinical tumor ablation. *World J Clin Oncol.* 2011;2(1):8-27. https://doi.org/10.5306/wjco.v2.i1.8

5. Rieke V, Pauly KB. MR thermometry. *J Magn Reson Imag.* 2008;27(2):376-390. https://doi.org/10.1002/jmri.21265

6. Hernando CG, Esteban L, Cañas T, Van Den Brule E, Pastrana M. The role of magnetic resonance imaging in oncology. *Clin Transl Oncol.* 2010;12(9):606-613. https://doi.org/10.1007/s12094-010-0565-x

7. Insightec. *Exablate Body.* Accessed November 30, 2021. https://www.insightec.com/products/exablate-body-system/overview

8. Profound Medical. *Customizable Incision-free Ablation Therapies.* Sonalleve | Profound Medical. Accessed November 30, 2021. https://profoundmedical.com/sonalleve/

9. Focused Ultrasound Foundation. *State of the field*; 2020. Accessed November 30, 2021. http://www.fusfoundation.org/images/pdf/Focused_Ultrasound_Foundation_2020_State_of_theFieldReport.pdf

10. Alpinion Medical Systems. *ALPIUS900.* Accessed November 30, 2021. http://www.alpinion.com/en/product/product_view_alpius900.do?productKey=KEY.1505083248000000219

11. Alpinion Medical Systems. *VIFU2000.* Accessed November 30, 2021. http://www.alpinion.com/en/product/product_view_vifu2000.do?productKey=KEY.1606034801000003466

12. Theraclion. *SONOVEIN.* Accessed November 30, 2021. https://www.theraclion.com/products/sonovein/

13. Theraclion. *ECHOPULSE.* Accessed November 30, 2021. https://www.theraclion.com/products/echopulse/

14. allbiomedical.com. *Ultrasonic Therapy Equipment.* HIFU Ablation System. Accessed December 6, 2021. http://aishen.allbiomedical.com/company/product_detail-HIFU-Ablation-System-134.html

15. Tognarelli S, Ciuti G, Diodato A, Miloro P. The FUTURA platform: a new approach merging non-invasive ultrasound therapy with surgical robotics. *Proceedings of the 36th Annual International Conference of the IEEE Engineering in Medicine and Biology Society.* Chicago, Illinois; 2014.

16. Price KD, Sin VW, Mougenot C, et al. Design and validation of an MR-conditional robot for transcranial focused ultrasound surgery in infants. *Med Phys.* 2016;43(9):4983-4995. https://doi.org/10.1118/1.4955174

17. Yiannakou M, Menikou G, Yiallouras C, Damianou C. MRI-guided coupling for a focused ultrasound system using a top-to-bottom propagation. *J Ther Ultrasound.* 2017;5(1):1-8. https://doi.org/10.1186/s40349-017-0087-x

18. Payne A, Chopra R, Ellens N, et al. AAPM Task Group 241: A medical physicist's guide to MRI- guided focused ultrasound body systems. *Med Phys.* 2021;48(9):772-806. https://doi.org/10.1002/mp.15076

19. Drakos T, Giannakou M, Menikou G, Constantinides G, Damianou C. Characterization of a soft tissue-mimicking agar/wood powder material for MRgFUS applications. *Ultrasonics.* 2021;113:10635. https://doi.org/10.1016/j.ultras.2021.106357

20. Antoniou A, Damianou C. MR relaxation properties of tissue-mimicking phantoms. *Ultrasonics.* 2022;119:106600. https://doi.org/10.1016/j.ultras.2021.106600

21. Damianou C, Giannakou M, Menikou G, Ioannou L. Magnetic resonance imaging-guided focused ultrasound robotic system with the subject placed in the prone position. *Digit Med.* 2020;6(1):24-31. https://doi.org/10.4103/digm.digm_2_20

22. Antoniou A, Giannakou M, Evripidou N, et al. Robotic system for magnetic resonance guided focused ultrasound ablation of abdominal

cancer. *Int J Med Robot Comput Assist Surg*. 2021;17(5):e2299. https://doi.org/10.1002/rcs.2299

23. Drakos T, Giannakou M, Menikou G, et al. MRI-guided focused ultrasound robotic system for preclinical use. *J Vet Med Anim Sci*. 2021;4(1):1-11.

24. Antoniou A, Drakos T, Giannakou M, et al. Simple methods to test the accuracy of MRgFUS robotic systems. *Int J Med Robot Comput Assist Surg*. 2021;17(4):e2287. https://doi.org/10.1002/rcs.2287

25. Epaminonda E, Drakos T, Kalogirou C, Theodoulou M, Yiallouras C, Damianou C. MRI guided focused ultrasound robotic system for the treatment of gynaecological tumors. *Int J Med Robot Comput Assist Surg*. 2016;12:46-52.

26. Yiallouras C, Ioannides K, Dadakova T, Pavlina M, Bock M, Damianou C. Three-axis MR-conditional robot for high-intensity focused ultrasound for treating prostate diseases transrectally. *J Ther Ultrasound*. 2015;3(1):1-10. https://doi.org/10.1186/s40349-014-0023-2

27. Mylonas N, Damianou C. MR compatible positioning device for guiding a focused ultrasound system for the treatment of brain deseases. *Int J Med Robot Comput Assist Surg*. 2014;10:1-10. https://doi.org/10.1002/rcs.1501

28. Damianou C, Ioannides K, Milonas N. Positioning device for MRI-guided high intensity focused ultrasound system. *Int J CARS*. 2008;2:335-345.

ORIGINAL ARTICLE

The International Journal of **Medical Robotics** and **Computer Assisted Surgery**

WILEY

Full coverage path planning algorithm for MRgFUS therapy

Anastasia Antoniou | Andreas Georgiou | Nikolas Evripidou [ID] | Christakis Damianou [ID]

Department of Electrical Engineering, Computer Engineering, and Informatics, Cyprus University of Technology, Limassol, Cyprus

Correspondence

Christakis Damianou, Department of Electrical Engineering, Computer Engineering, and Informatics, Cyprus University of Technology, 30 Archbishop Kyprianou Street, 3036 Limassol, Cyprus.
Email: christakis.damianou@cut.ac.cy

Abstract

Background: High-quality methods for Magnetic Resonance guided Focussed Ultrasound (MRgFUS) therapy planning are needed for safe and efficient clinical practices. Herein, an algorithm for full coverage path planning based on preoperative MR images is presented.

Methods: The software functionalities of an MRgFUS robotic system were enhanced by implementing the developed algorithm. The algorithm's performance in accurate path planning following a Zig-Zag pathway was assessed on MR images. The planned sonication paths were performed on acrylic films using the robotic system carrying a 2.75 MHz single element transducer.

Results: Ablation patterns were successfully planned on MR images and produced on acrylic films by overlapping lesions with excellent match between the planned and experimental lesion shapes.

Conclusions: The advanced software was proven efficient in planning and executing full ablation of any segmented target. The reliability of the algorithm could be enhanced through the development of a fully automated segmentation procedure.

K E Y W O R D S
algorithm, MRgFUS, path planning, plastic films, segmentation

1 | INTRODUCTION

High Intensity Focussed Ultrasound (HIFU) has been used in the clinical management of various medical diseases as a beneficial non-invasive alternative to traditional therapeutic approaches.[1] The HIFU-induced thermal effects have been extensively exploited in oncology, where the ultrasound beams are concentrated into a mm-sized location causing rapid temperature elevation in local tissue, without damaging tissues in the acoustic path.[1] Exposure of tissue to temperatures higher than 60°C for 1 s was proven sufficient to produce coagulation necrosis and lesion formation.[2] Since tumours have a diameter of several centimetres, ablation of their entire volume requires generating lesions side-by-side. Navigation of the beam focus through the entire tumour is achieved by mechanically moving the source or by electronically steering the beam using phased array technology.[3]

Through the view of physicians, high-quality methods for treatment planning and real-time monitoring of heating during HIFU are needed for safe and efficient clinical practices. Briefly, the planning process involves pretherapy imaging and tumour segmentation followed by administration of sonication points throughout the marked region of interest (ROI) and selection of the proper scanning pathway.[4] The sonication protocol is then executed commonly under the guidance of ultrasound (US) or Magnetic Resonance Imaging

(MRI).[1] Although both constitute well-established non-invasive imaging modalities, MRI produces anatomical images of significantly higher resolution regardless of depth and intervening structures, thus enabling tissue targeting and focus positioning with very high precision.[5] Simultaneously, MRI has the unique ability of intraoperative temperature monitoring for selective tissue ablation through MR-based thermometry.[6] The HIFU technology combined with MRI is known as Magnetic Resonance guided Focussed Ultrasound (MRgFUS).

The first step in the planning process is localising the ROI in preoperative MR images.[4] Currently, localisation of the ROI typically requires manual involvement by a trained physician, which unavoidably decreases the therapeutic efficacy.[7] Clinical practices will thus be greatly benefited by computer-based methods for automated segmentation and full coverage path planning.[4] As an example, Loeve et al.[4] reported an average time of 18 min for image segmentation of the target based on observations of MRgFUS interventions in the uterine, suggesting that the total treatment duration could be decreased by automated segmentation, especially when multiple segmentation adjustments are needed for motion compensation.[4]

Since MRI is routinely employed in brain disease detection,[8] there is a wide variety of techniques for brain lesion segmentation in MR images available in the literature, which may be helpful given the adaption of MRgFUS as a neurotherapeutic tool.[9] Zhang et al.[10] classified the existing methods into three main categories; conventional methods (i.e., threshold, region, fuzzy theory, and edge detection), classical machine learning-based methods (i.e., K Nearest Neighbour - KNN, random forest, Contingent Valuation Method - CVM, and dictionary learning) and deep learning-based methods (i.e., Convolutional Neural Network - CNN, Fully Convolutional Network - FCN, and encoder-decoder). Another similar review study[11] concluded that the tumour segmentation is more effective when a fully CNN is combined with a Conditional Random Field (CRF) statistical method.

The-wide adaption of HIFU in the clinical management of uterine fibroids has led scientists to the development of more advanced planning and guiding tools for this specific application. Xu et al.[12] proposed an automatic segmentation method for uterine fibroids on US images. The developed algorithm involves dividing the image into smaller regions called superpixels that are characterised using a texture histogram-based feature representation method and finally merging them again based on their similarities, meaning that the tumour's pixels will be merged together since they have similar texture.[12] Recently, Ning et al.[7] proposed an image guidance system featuring tools for automatic detection and segmentation of lesions on MR images through a CNN multi-stage segmentation. Notably, the developed system also enables intraoperative lesion tracking on US images.[7]

Recently, in the effort to enhance MRgFUS therapy planning, three classical methodology types were assessed for their performance in segmenting ROIs (e.g., tissue, water, and transducer) in MR images of a HIFU setup.[13] The tested methods were the simplest image segmentation method known as the Threshold method, the Watershed segmentation algorithm with markers (WSAM), and two Level set methods (LSM); the Geodesic Active Contours (GAC) and the Distance Regularised Level Set Evolution (DRLSE) methods. Preliminary results were promising; however, the methods are accompanied by some limitations, such as the need to establish an initial contour for GAC and DRLSE methods and the complex procedure of defining the markers of WSAM, which both require previous intervention by the user for MR image division.[13]

The segmentation procedure is followed by path planning for selective ablation of the delineated ROI.[4] Selection of the proper scanning pathway is essential in forming uniform lesions throughout the segmented target and minimising thermal exposure of normal tissue.[14] A conventional scanning approach in clinical HIFU is the Raster scanning where the ultrasonic source sequentially visits spots arranged in horizontal lines that are scanned in the same direction.[14] Thermal diffusion was proven an essential phenomenon reducing the therapeutic outcome of this scanning mode through the formation of asymmetric lesions.[14–16] This is attributed to that lesion formation at a specific spot is affected by the thermal energy diffusing from neighbouring previously sonicated spots, thereby leading to inadequate treatment of initial spots and extensive heating of the later ones, as well as excess thermal dose deposition in the pre-focal area, a phenomenon known as the near-field heating.[17]

Therefore, there are still challenges in achieving ablation of a well-defined area by eliminating thermal diffusion effects while ideally using the minimum energy and treatment time possible. In this effort, researchers have investigated how various scanning paths and the used sonication parameters affect the therapeutic result of HIFU therapy.[14,18–21] Zhou et al.[14] investigated how the Spiral scanning from the centre to the outside and vice versa affect the formation of lesions by sonicating a gel phantom and bovine liver in a discrete rhombus-shaped grid. The proposed scanning approaches produced more uniform lesions but of a smaller volume than conventional raster scanning when used under the same protocol.[14] Qian et al.[18] also investigated the performance of a Spiral pathway that was executed in a continuous scanning mode covering a square area in acrylamide-based heat-sensitive phantom and bovine liver. The results suggest that uniform lesions without overheating phenomena can be produced by continuous scanning along the spiral pathway by selecting proper scanning speed to regulate thermal energy diffusion.[18]

Typically, discrete scanning modes employ a time delay between successive sonications of equal duration to eliminate intense heating.[17] In accordance, the accumulation of thermal energy should be controlled by selecting not only the proper pathway, but also sufficient cooling periods. A recent study[17] evaluated the effect of increasing time delay on the induced near-field heating and overall treatment time for six different pathway algorithms, including the commonly used Sequential and Spiral algorithms. It is noted that the Sequential algorithm differs from the aforementioned Raster scanning only in that adjacent lines are scanned in opposite directions. Experimental evaluation in a tissue-mimicking phantom (TMP) revealed that a minimum time delay of 50–60 s

is needed for achieving a safe thermal dose in the near-field region.[17]

At this point, it is interesting to note that the use of different sonication times at the various grid spots was proposed as an alternative method to avoid the introduction of cooling intervals, thus minimising the overall treatment time.[19] The relevant article compared the performance of the Raster, Spiral, and Skip paths using unequal heating duration with the conventional scanning mode by simulating the ablation of a square area through electronic steering of the beam according to each pathway.[19] The results suggest that the proposed method is robust when used in combination with the Skip scanning path and could lead to a treatment time reduction of more than 50%.[19]

Herein, a full area coverage path planning algorithm intended for planning MRgFUS sonication protocols is presented. The ROI in a medical image is initially marked following placement of indicative points by the user. In brief, sonication points are then placed throughout the segmented ROI and sorted based on a Zig Zag pathway to be sequentially visited by the ultrasonic source.

The accuracy of the developed algorithm was evaluated using an MRgFUS robotic system intended for preclinical use. The algorithm was implemented within the relevant controlling software. Once the power field of the incorporated transducer was tested ensuring sufficient emission of ultrasonic energy, the performance of the algorithm was assessed by path planning on medical images and execution of the planned sonications on plastic films for visual assessment of accuracy.

Advantageously, the proposed algorithm is specifically dedicated to path planning of MRgFUS robotic devices, whereas authors in previous studies developed planning tools for US-guided therapy[7,12] or examined the performance of already existing segmentation tools.[13] With the proposed algorithm, the whole procedure from the lesion segmentation stage and distribution of foci to path execution is implemented in the MRI setting. In addition, the algorithm is simplified and fast, and thus more ergonomic in its use.

2 | MATERIALS AND METHODS

2.1 | Robotic system for MRgFUS preclinical use

A robotic system intended for preclinical applications of MRgFUS was used for the purposes of the study.[22] The system was manufactured on a rapid prototyping machine (FDM400, Stratasys, 7665 Commerce Way, Eden Prairie, Minnesota, 55344, USA) with Acrylonitrile Butadiene Styrene (ABS) thermoplastic. All the components were selected based on MR compatibility to enable proper operation in the MRI environment. Due to its compact design (57 cm in length, 21 cm in width and 11.5 cm in height) is capable to be fitted inside the MRI operating table for prone positioning of the subject, simultaneously facilitating ease of transfer, also given its lightweight design of about 5 kg. Accordingly, the treatment area is targeted from the bottom to the top.

The main device comprises an enclosure where the motion mechanism is actuated, being driven by piezoelectric motors (USR30-S3, Shinsei Kogyo Corp., Tokyo, Japan) in 4 computer-controlled degrees of freedom (DOF) for positioning the ultrasonic transducer about the subject. The transducer is accommodated in a separate water-filled enclosure through an arm extending from the mechanism. In this study, a single element spherically focussed transducer with a nominal frequency of 2.75 MHz, a radius of curvature of 65 mm, and a diameter of 50 mm was integrated with the system. The transducer was tuned with an RF amplifier (AG1016, AG Series Amplifier, T & C Power Conversion, Inc., Rochester, US) for optimum power output, achieving a percent acoustic efficiency of 30%. Notably, the positioning mechanism is robust enough to carry a phased array transducer. The described system is shown in Figure 1.

2.2 | Software for robotic control

The various functionalities of the system are controlled remotely through an in-house developed software written in C sharp programing language (Visual Studio 2010 Express, Microsoft Corporation). The main algorithms implemented allow for controlling the robotic motion and FUS operation. The user commands motion in grid patterns by specifying the relevant parameters (grid size, motion pattern, spatial step, and time delay between successive sonications) and visualizes the grid operation in real time through a user-friendly graphical interface. The sonication parameters at each spot are easily adjusted by the user. This software can be interfaced with the MRI so that medical images are directly transferred for further processing and treatment planning, as well as for controlled ultrasonic exposures through the use of MR thermometry.[6] Figure 2 shows a block diagram of the connection between hardware and software through the MRI penetration panel.

2.3 | Path planning algorithm

The software was extended with additional functionalities to support therapy planning. The developed algorithm consists of 5 basic sub-processes as illustrated in the schematic diagram of Figure 3. The algorithm receives as input a list of vertices (at least 3) that are manually selected by the user as points (x, y) on the medical image from the graphical user interface of the software. These points are connected forming a polygon indicating the ROI where sonication will take place. The user should also select the intended motion step in mm for the X and Y axes, which defines the resolution of sonication. The second subprocess involves the Point of Polygon (POP) Algorithm that is responsible for identifying which pixels of the entire medical image are included within the delineated area based on the Jordan Curve Theorem.[23] Once the involved pixels are identified, a boundary box is created around the segmented area. Binary arrays are generated so that each pixel is assigned a number (0 or 1) defining whether or not it
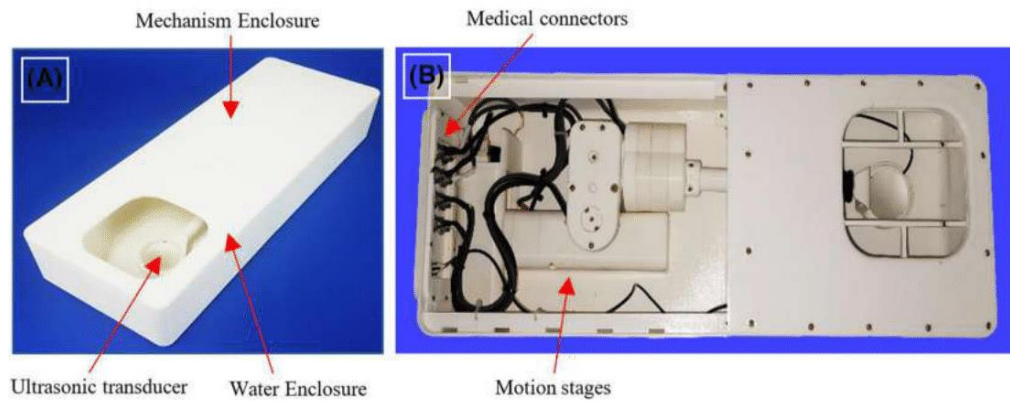
41

FIGURE 1 (A) Exterior and (B) interior views of the 4 degrees of freedom (DOF) Magnetic Resonance guided Focussed Ultrasound (MRgFUS) robotic device
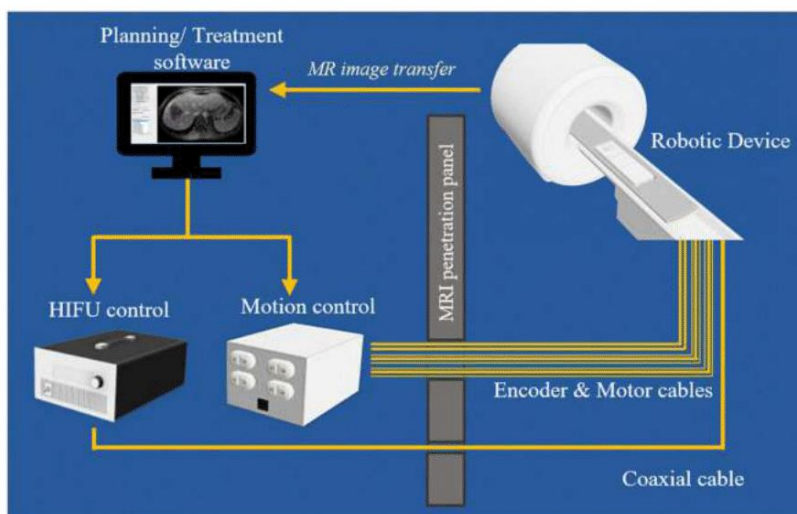

FIGURE 2 Block diagram of the connection between hardware and software through the Magnetic Resonance Imaging (MRI) penetration panel

should be sonicated. The localised sonication points are then sorted in the order to be visited by the transducer based on a Zig Zag pattern (step 4). Finally, the sorted points are converted into motion vectors through step 5. A homing procedure follows where the offset between the origin point of the sonication frame (boundary box of the segmented area) and the real location of the transducer is compensated. The extracted path planning vectors serve as the output defining the transducer's path in two-dimensional space for full coverage of the segmented area. These motion vectors are sent successively to the driving system for execution. Figure 4 is a screenshot of the software interface for path planning.

2.4 | Evaluation of power field

The power field of the transducer was evaluated by HIFU sonications on clear films made of acrylic plastic with a thickness of 0.9 mm (FDM400mc print plate, Stratasys). The ultrasonic attenuation of the plastic films was estimated at 8.5 dB/cm-MHz

(at 2 MHz) according to the transmission through technique.[24] The focussed transducer was mounted on a special holder that was geometrically designed to enable horizontal placement of the film at varying distance above the transducer and the whole structure was immersed in degassed water for proper ultrasonic transmission. The films were sonicated at various distances from the transducer's surface using a constant electric power of 150 W (acoustic power of 45 W) and a sonication time of 10 s. The upper side of the film involved air, and thus, the heating of the film was mainly based on reflection. The diameter of the formed lesion at each distance was estimated.

2.5 | Evaluation of the algorithm's performance

The accuracy of the proposed algorithm was evaluated by path planning on medical images. MR images of brain and TMPs were imported in the software for processing by the user. The sonication protocols were automatically developed after placement of initial
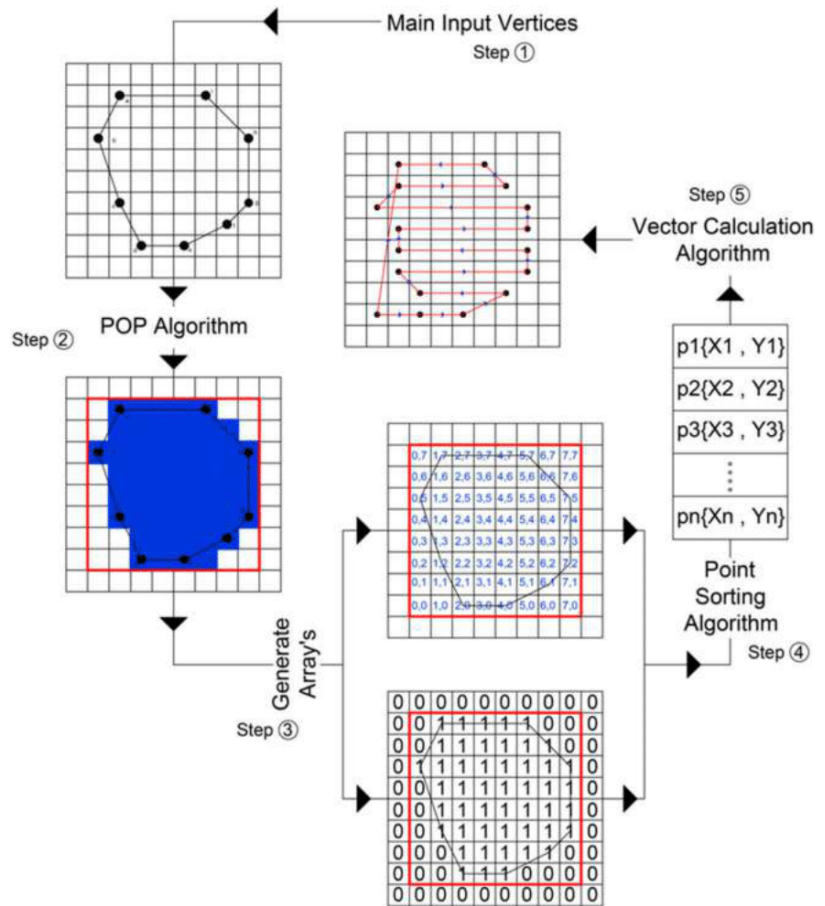
points by the user and executed on acrylic films to assess the performance of the algorithm as implemented in the FUS procedure. Simultaneously, the robotic system was evaluated in terms of proper communication with the software and accuracy of robotic motion.

Plastic films with approximate dimensions of 82 × 87 × 0.9 mm were fixed to the acoustic opening of the water enclosure at a constant distance of approximately 55 mm above the transducer's surface with the assistance of a special holder as illustrated in Figure 5. Again, degassed water served as the coupling medium. Multiple sonications along the planned Zig-Zag pathway were performed using grid operation with a 2 mm step. Each grid spot was sonicated using a moderate acoustical power of 30 W for 7 s with a time delay of 30 s between successive expositions. It is noted that the optimum sonication time for lesion formation was selected at 7 s following initial testing with varying sonication times. The selection of a proper time delay was mainly based on the results of a previous study of the group[17] suggesting that a time delay of 60 s is needed between 2 mm spaced sonication spots to reduce off-target heating in an agar-based TMP. Given that thermal diffusion is a less effective mechanism of energy loss in plastic, a 30 s delay was considered sufficient.

3 | RESULTS

An indication of the power field of the ultrasonic transducer was obtained by sonicating plastic films at increasing depth of 35–95 mm from the transducer's surface. Figure 6 shows a photo of the sonicated films indicating the diameter of the formed lesions. Visual assessment reveals a focal spot shifted at 55 mm. Notably, large lesions were observed at distances of 35, 45 and 65 mm indicating increased heating in the near-field region. No lesions were observed at distances of 85 and 95 mm. The change in the lesion size with varying distance is indicative of the power field distribution. Specifically, assuming a Gaussian distribution of acoustic power around the maxima in axial and radial planes, the dimensions of the formed lesions are defined by the half power length and width, respectively.

Next, MR images were used for assessing the performance of the developed algorithm in accurate path planning. Figure 7 shows a two-dimensional representation of sonication spots sorted along the planned Zig-Zag pathway and the corresponding segmented ROI from an MR TMP image. Indicative results of ablation patterns produced on acrylic films are presented in Figure 8. A 2-mm step was proven suitable for creating overlapping lesions when using
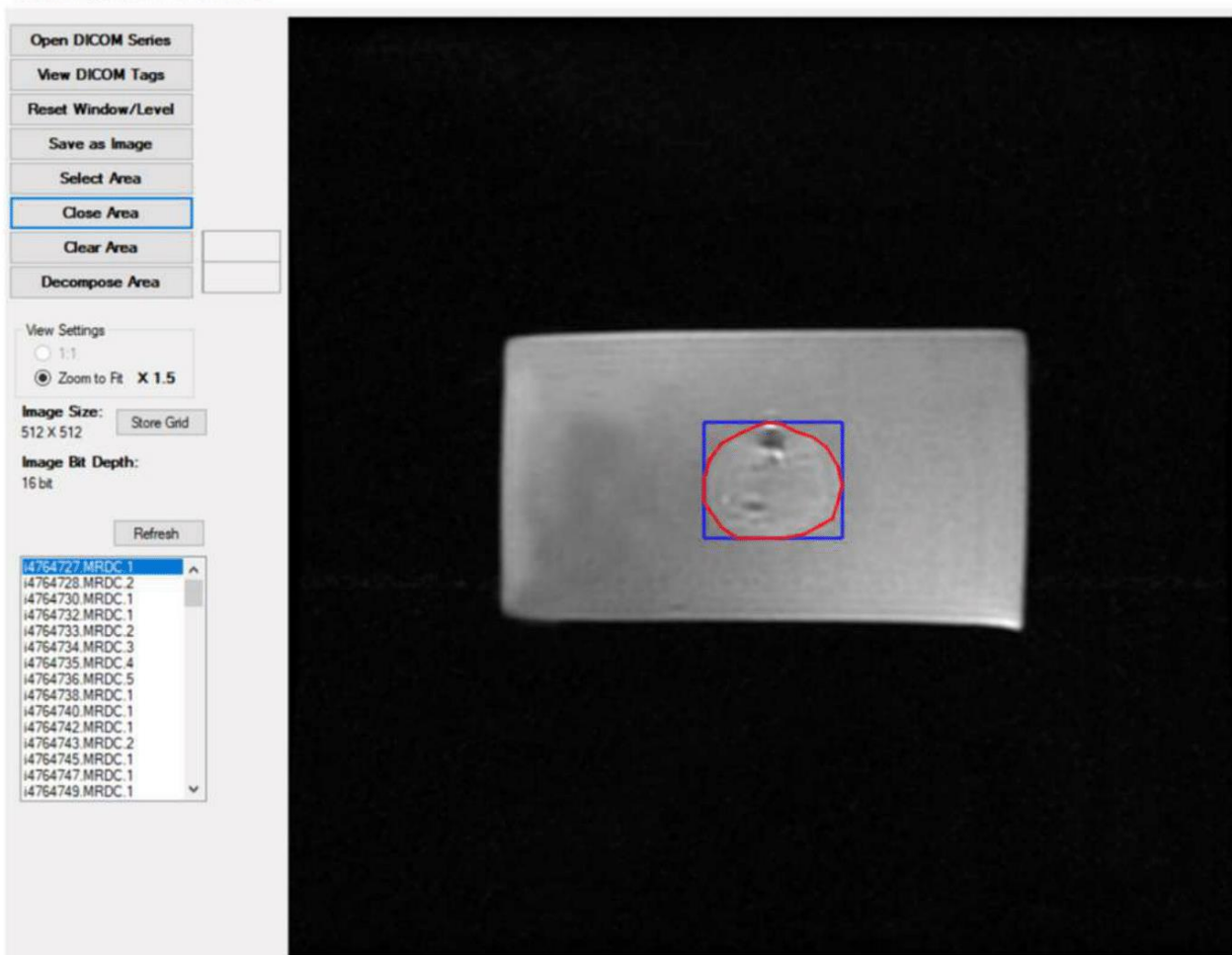
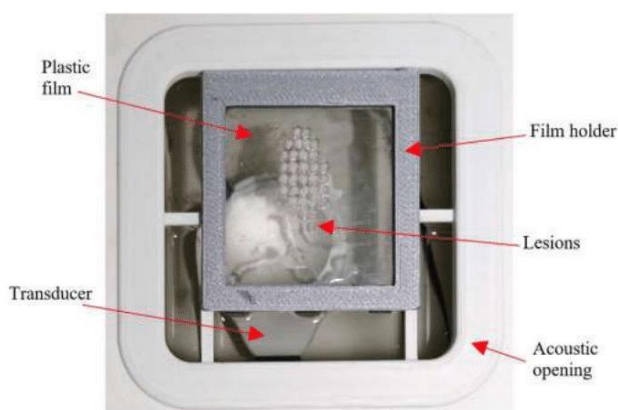**FIGURE 4** Screenshot of the software interface for path planning

FIGURE 5 Photo of the experimental setup used for sonicating plastic films

the specific sonication protocol (30 W acoustical power and 7 s sonication time). As revealed by Figure 8, the shape of the ablated areas matches well with the corresponding ROIs.

4 | DISCUSSION

In this study, the software of an already existing MRgFUS system was enhanced by implementing a full coverage path planning algorithm. Medical images are directly transfer from the MRI scanner to the software's interface for treatment planning. Briefly, the algorithm enables ROI segmentation on preoperative MR images and automatic generation of the sonication pathway based on a Zig-Zag pattern. In fact, the marked area is filled with sonications spots that are being executed individually with a spatial step that is defined by the user. The estimated prediction time of the navigation path on MR images of 512×512 pixels is less 1 s for any lesion size, even when using a very small spatial step of 1 mm.

Thin acrylic films served as the main tool in the evaluation process. Initially, the power field of the FUS transducer was evaluated through visual and quantitative assessment of lesions produced on the plastic films at various distances from the transducer's surface. The results confirmed sufficient emission of ultrasonic energy and revealed a shift of the focal depth of about 10 mm towards the
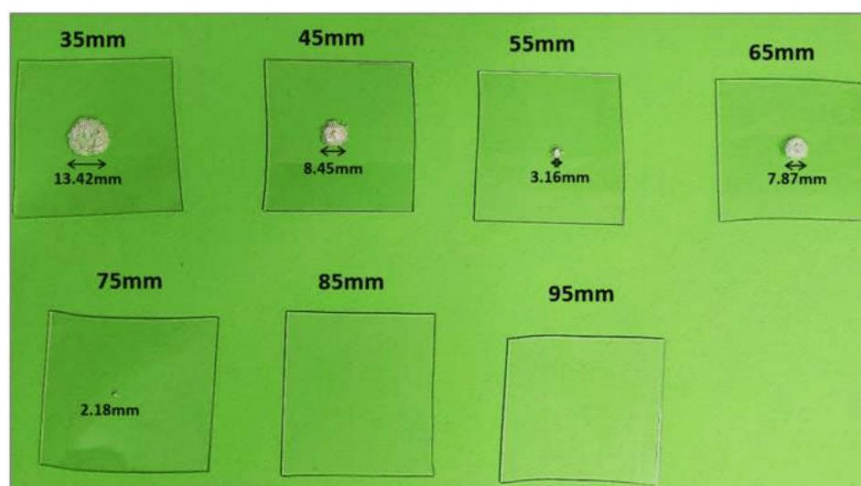
FIGURE 6   Photo of films sonicated at increasing depth from the surface of a single element transducer with central frequency of 2.75 MHz, radius of curvature of 65 mm, and diameter of 50 mm, indicating the diameter of the formed lesions
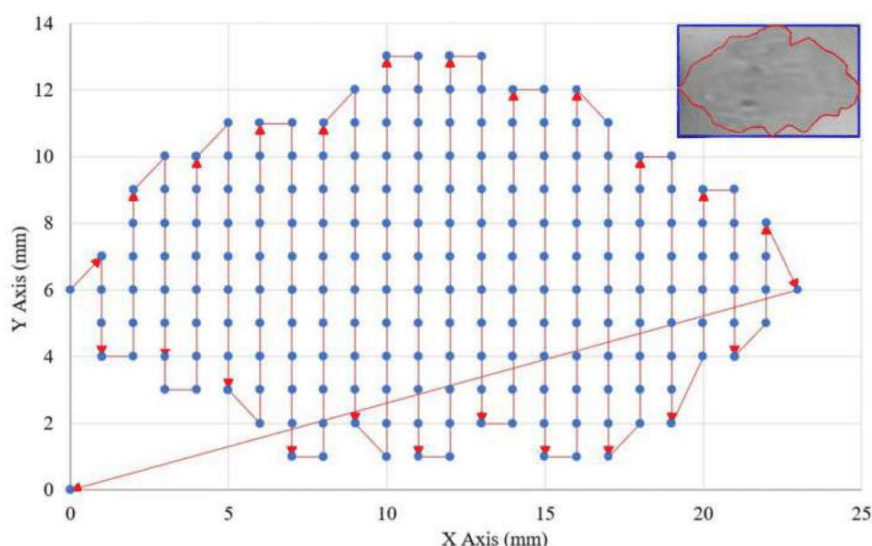

FIGURE 7   Representation of sonication spots arranged in the X-Y plane and the planned Zig-Zag pathway for full coverage of a segmented region of interest (ROI; upper right)

transducer. This information was useful for the next experiments. It should be also noted that lesion formation resulted from reflection at the plastic/air interface.

The main task in the evaluation process concerned the assessment of the path planning performance of the developed algorithm using a series of MR images. Successful planning was observed in all cases without any software defects. Next, the planned sonication protocols were executed by sonicating acrylic films using the integrated MRgFUS robotic system. Acrylic softens gradually as temperature rises. As an amorphous polymer, it crystallises and turns white when experiencing stress. In the current study, it was observed that heating at temperatures of about 55°C softens the material, and as a result acoustic pressure causes formation of white bumps

referred to as lesions. Application of 30 W for 7 s (~200 J energy) produced such temperatures, thus leading to lesion formation. The 2 mm step (with a 30 s delay) was proven suitable for creating overlapping lesions, whereas bigger steps resulted in discrete lesions. Well defined areas of overlapping lesions were produced on the films, with excellent match between the planned and experimental lesion shapes. High accuracy of robotic positioning of the source was also evidenced.

It is interesting to note that plastic films can be considered the cheapest phantom for quality assurance of hardware and software FUS systems. Notably, grid ablation on plastic films was previously proposed as a simple method to test the accuracy of robotic motion of FUS devices,[25] being beneficial over other proposed MRI-based
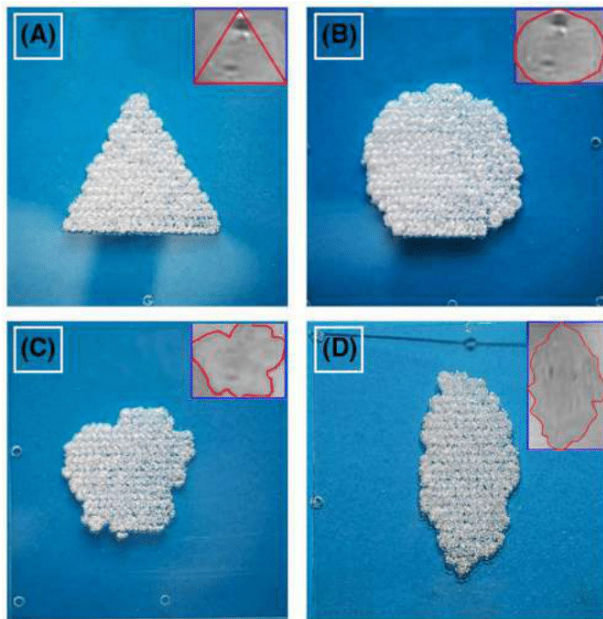
FIGURE 8 Ablation patterns on plastic films as planned on MR images of a tissue-mimicking phantom (TMP; upper right of each image). The sonications were performed using acoustic power of 30 W for 7 s at each spot with a spatial step of 2 mm and a time delay of 30 s, using a single element transducer with central frequency of 2.75 MHz, radius of curvature of 65 mm, and diameter of 50 mm

methods[26] in terms of cost-effectiveness, ease of implementation, and accuracy.

Thermal diffusion from neighbouring spots is an important aspect in the therapeutic outcome of FUS treatment since it affects the formation of uniform lesions in tissue.[14,15] Production of asymmetric lesions was observed in optically transparent TMPs and excised tissue.[14,15] Curiel et al.[15] reported a progressive enlargement of lesion size on in vitro pig liver after sonications in a line grid where each spot was exposed at acoustic power of 37 W for 2 s with 8 s waiting time between them. In the current study, although higher energy was applied at each spot (30 W for 7 s) with a similar spatial and temporal delay, there was no evidence of thermal diffusion effects on lesion production, meaning that visual assessment did not reveal significant variability in lesion density that would indicate variability in size of individual lesions. Note that uniformity of lesions is better observed in Figure 5 that shows a discrete pattern of almost equally spaced lesions of similar size and shape. This is expected given the smaller rate of heat transfer in acrylic plastic compared to soft tissue. In fact, the thermal conductivity of body organs is around 0.5–0.6 W/m-K,[27] whereas a value of 0.2 W/m-K is reported literally for acrylic plastic.[28] Accordingly, although phantoms with tissue like properties are especially useful in the evaluation of thermal protocols,[29,30] plastic films constitute a more practical and cost-effective solution for assessing the performance of planning algorithms without thermal diffusion or other phantom-dependent parameters affecting the results.

The previous version of the software included commands for controlling robotic motion and ultrasonic exposures. Advantageously, the developed algorithm enabled accurate path planning for full coverage of segmented ROIs of any shape, whereas the previous version allowed just for automating motion in XY rectangular grids.[31] Such simplified motion algorithms were widely used in order to test the functionality of MRgFUS robotic devices in creating discrete and overlapping lesions, specifically by performing multiple ablations in line and square grid patterns in gel TMPs and animal tissue.[15,32–36]

In the current version, the software can be interfaced with the MRI system enabling real time transfer and display of MR images on the software screen. The incorporation of path planning and MR thermometry tools aims to offer an efficient procedural workflow from the path planning stage to treatment plan execution. During treatment in the MRI setting, execution of the planned path will be visualised on the screen with simultaneous monitoring of thermal heating and feedback on ablation through the use of MR thermometry.

Follow up studies will test the performance of the developed software in *ex-vivo* and in vivo animal tissue where thermal diffusion phenomena are more likely to affect lesion formation. This will enable better assessment of the performance of the Zig Zag pattern and will provide insights on the sonication protocol for safe in vivo studies. Generally, elevation of tissue temperature to more than 60°C for 1 s was proven to cause instantaneous death of cells mainly via coagulation mechanisms.[2] In this regard, the optimal combination of acoustic parameters, motion step and time delay for achieving such ablative temperatures and formation of uniform lesions in soft tissue should be determined.

Although efforts were made for eliminating manual intervention and related errors in HIFU therapy planning,[7,12] there is still a need for fully automated procedures of high accuracy. The developed algorithm requires manual intervention for tumour segmentation through the user interface. The introduction of deep learning methods for automatic segmentation along the tumour margins is deemed necessary for achieving the precision required for clinical use. Such methods for automatic ROI localization on MR images are available in the literature[10] and may be implemented in the algorithm in a later stage to eliminate user's involvement. Another advancement to be made is the transition from two-dimensional to three-dimensional planning, which may also require the incorporation of deep-learning methods.

5 | CONCLUSIONS

Overall, the herein proposed algorithm enables fast full coverage path planning on preoperative MR images. The developed algorithm as implemented in the software of an MRgFUS system was proven efficient in planning and executing ablation of two-dimensional ROIs of complex geometry by sonicating transparent acrylic films in a Zig-Zag pattern. Visual assessment revealed excellent match between the planned and experimental lesion shapes. Remarkably, plastic films

probably constitute the cheapest phantom for quality assurance purposes of FUS devices. There are still challenges to be overcome for increasing the reliability of the developed algorithm through the development of a fully automated segmentation procedure.

CONFLICT OF INTEREST

The authors have no conflict of interest.

AUTHOR CONTRIBUTION

Andreas Georgiou contributed to the development of the path planning algorithm. Anastasia Antoniou contributed to the draughting of manuscript and scientific methods. Nikolas Evripidou contributed to the evaluation experiments. Christakis Damianou supervised the overall study, as well as the draughting of the manuscript.

DATA AVAILABILITY STATEMENT

The data that support the findings of this study are available from the corresponding author upon reasonable request.

ORCID

Nikolas Evripidou https://orcid.org/0000-0002-8200-3349
Christakis Damianou https://orcid.org/0000-0003-0424-2851

REFERENCES

1. Izadifar Z, Izadifar Z, Chapman D, Babyn P. An introduction to high intensity focused ultrasound: systematic review on principles, devices, and clinical applications. *J Clin Med.* 2020;9(2):460.
2. Zhou Y-F. High intensity focused ultrasound in clinical tumor ablation. *World J Clin Oncol.* 2011;2(1):8-27.
3. Quadri SA, Waqas M, Khan I, et al. High-intensity focused ultrasound: past, present, and future in neurosurgery. *Neurosurg Focus.* 2018;44(2).
4. Loeve AJ, Al-Issawi J, Fernandez-Gutiérrez F, et al. Workflow and intervention times of MR-guided focused ultrasound-predicting the impact of new techniques. *J Biomed Inf.* 2016;60:38-48.
5. Hernando CG, Esteban L, Cañas T, Van Den Brule E, Pastrana M. The role of magnetic resonance imaging in oncology. *Clin Transl Oncol.* 2010;12(9):606-613.
6. Rieke V, Pauly KB. MR thermometry. *J Magn Reson Imag.* 2008;27(2):376-390.
7. Ning G, Zhang X, Zhang Q, Wang Z, Liao H. Real time and multi-modality image-guided intelligent HIFU therapy for uterine fibroid. *Theranostics.* 2020;10(10):4676-4693.
8. Villanueva-Meyer JE, Mabray MC, Cha S. Current clinical brain tumor imaging. *Clin Neurosurg.* 2017;81(3):397-415.
9. Lee EJ, Fomenko A, Lozano AM. Magnetic resonance-guided focused ultrasound: current status and future perspectives in thermal ablation and blood-brain barrier opening. *J Korean Neurosurg Soc.* 2019;62(1):10-26.
10. Zhang W, Wu Y, Yang B, Hu S, Wu L, Dhelimd S. Overview of multi-modal brain tumor MR image segmentation. *Healthcare.* 2021;9(8):1-20.
11. Wadhwa A, Bhardwaj A, Singh Verma V. A review on brain tumor segmentation of MRI images. *Magn Reson Imaging.* 2019;61:247-259.
12. Xu M, Zhang D, Yang Y, Liu Y, Yuan Z, Qin Q. A split-and-merge-based uterine fibroid ultrasound image segmentation method in HIFU therapy. *PLoS One.* 2015;10(5):1-24.
13. Vargas-Olivares A, Navarro-Hinojosa O, Pichardo S, Curiel L, Alencastre-Miranda M, Chong-Quero JE. Image segmentation for the treatment planning of magnetic resonance-guided high-intensity focused ultrasound (MRgFUS) therapy: a parametric study. *Appl Sci.* 2019;9(24):1-23.
14. Zhou Y, Kargl SG, Hwang JH. The effect of the scanning pathway in high-intensity focused ultrasound therapy on lesion production. *Ultrasound Med Biol.* 2011;37(9):1457-1468.
15. Curiel L, Chavrier F, Gignoux B, Pichardo S, Chesnais S, Chapelon JY. Experimental evaluation of lesion prediction modelling in the presence of cavitation bubbles: intended for high-intensity focused ultrasound prostate treatment. *Med Biol Eng Comput.* 2004;42(1):44-54.
16. Zhou Y, Kargl SG, Hwang JH. Producing uniform lesion pattern in HIFU ablation. *AIP Conference Proceedings.* 2009;1113:91-95.
17. Filippou A, Drakos T, Giannakou M, Evripidou N, Damianou C. Experimental evaluation of the near-field and far-field heating of focused ultrasound using the thermal dose concept. *Ultrasonics.* 2021;116:106513.
18. Qian K, Li C, Ni Z, Tu J, Guo X, Zhang D. Uniform tissue lesion formation induced by high-intensity focused ultrasound along a spiral pathway. *Ultrasonics.* 2017;77:38-46.
19. Li D, Shen G, Luo H, Bai J, Chen Y. A study of heating duration and scanning path in focused ultrasound surgery. *J Med Syst.* 2011;35:779-786.
20. Vykhodtseva NI, Hynynen K, Damianou C. Pulse duration and peak intensity during focused ultrasound surgery: theoretical and experimental effects in rabbit brain in vivo. *Ultrasound Med Biol.* 1994;20(9):987-1000.
21. Damianou C, Hynynen K. The effect of various physical parameters on the size and shape of necrosed tissue volume during ultrasound surgery. *J Acoust Soc Am.* 1994;95(3):1641-1649.
22. Drakos T, Giannakou M, Menikou G, et al. MRI-guided focused ultrasound robotic system for preclinical use. *J Vet Med Anim Sci.* 2021;4(1):1-11.
23. Zhang X. A proof of the Jordan Curve Theorem. *Nat Sci.* 2019;11(12):345-360.
24. Antoniou A, Evripidou N, Giannakou M, Constantinides G, Damianou C. Acoustical properties of 3D printed thermoplastics. *J Acoust Soc Am.* 2021;149(4):2854-2864.
25. Antoniou A, Drakos T, Giannakou M, et al. Simple methods to test the accuracy of MRgFUS robotic systems. *Int J Med Robot Comput Assist Surg.* 2021;17(4).
26. Yiannakou M, Menikou G, Yiallouras C, Ioannides C, Damianou C. MRI guided focused ultrasound robotic system for animal experiments. *Int J Med Robot Comput Assist Surg.* 2017;13(4):e1804.
27. Giering K, Minet O, Lamprecht I, Müller G. Review of thermal properties of biological tissues. In: *Proceedings of SPIE - The International Society for Optical Engineering*; 1995:45-65.
28. Donev J, Stenhouse K, Hanania J, Afework B. Energy education - thermal conductivity. Accessed December 18, 2021. https://energyeducation.ca/encyclopedia/Thermal_conductivity
29. Damianou C. The role of phantoms in magnetic resonance imaging-guided focused ultrasound surgery. *Digit Med.* 2019;5(2):52-55.
30. Antoniou A, Damianou C. MR relaxation properties of tissue-mimicking phantoms. *Ultrasonics.* 2022;119.

31. Yiallouras C, Menikou G, Yiannakou M, Damianou C. Software that controls a magnetic resonance imaging compatible robotic system for guiding high-intensity focused ultrasound therapy. *Digit Med.* 2017;3(3):123-132.

32. Yiallouras C, Mylonas N, Damianou C. MRI-compatible positioning device for guiding a focused ultrasound system for transrectal treatment of prostate cancer. *Int J Comput Assist Radiol Surg.* 2014; 9(4):745-753.

33. Yiallouras C, Ioannides K, Dadakova T, Pavlina M, Bock M, Damianou C. Three-axis MR-conditional robot for high-intensity focused ultrasound for treating prostate diseases transrectally. *J Ther Ultrasound.* 2015;3(1):1-10.

34. Epaminonda E, Drakos T, Kalogirou C, Theodoulou M, Yiallouras C, Damianou C. MRI guided focused ultrasound robotic system for the treatment of gynaecological tumors. *Int J Med Robot Comput Assist Surg.* 2016;12:46-52.

35. Antoniou A, Giannakou M, Evripidou N, et al. Robotic system for magnetic resonance guided focused ultrasound ablation of abdominal cancer. *Int J Med Robot Comput Assist Surg.* 2021;17(5).

36. Damianou C, Ioannides K, Hadjisavvas V, Mylonas N, Couppis A, Iosif D. In vitro and in vivo brain ablation created by high-intensity focused ultrasound and monitored by MRI. *IEEE Trans Ultrason Ferroelectrics Freq Control.* 2009;56(6):1189-1198.

Ultrasonic attenuation of canine mammary tumours

Antria Filippou, Christakis Damianou[*]

Cyprus University of Technology, Department of Electrical Engineering, Computer Engineering, and Informatics, Limassol, Cyprus

A B S T R A C T

Background: Canine mammary tumours (CMTs) are the most common neoplasm appearing in female dogs and are considered the equivalent animal model of human breast cancer. However, in the literature, there is a gap for ultrasonic characterisation of these tumours. In this study, experimental measurements for acoustic attenuation and propagation speed of three surgically excised malignant CMTs were implemented.

Methods: The three tumours were fixed in formaldehyde for up to 72 h and a total of five sample pieces were sectioned from the three tumours to account for the varied morphology observed along the tumours. The through-transmission and pulse-echo techniques were employed for experimental measurements of the acoustic attenuation and propagation speed.

Results: Acoustic propagation speed of the five samples as measured at 2.7 MHz was in the range of 1568–1636 m/s. Correspondingly, acoustic attenuation was in the range of 1.95–3.45 dB/cm.MHz. Variations in both speed and attenuation were observed between samples acquired from the same tumour.

Conclusions: Present findings suggest that both acoustic attenuation and propagation speed of CMTs are higher than normal canine tissues due to increased heterogeneity and varied morphology visually observed between the tumour specimens and evidenced by histological examination. Nevertheless, experimental results could aid in enhancing the use of ultrasound in the diagnosis and treatment of CMTs as well as provide essential data for comparative oncology.

1. Introduction

Canine mammary gland tumours (CMTs) represent the most common neoplasm appearing in female dogs [1], accounting for approximately 50–70 % of all reported cancer cases [2,3] while, more rarely, they also affect male canines [4]. The prevalence of CMTs is more frequent in the abdominal caudal and inguinal regions [5] and is significantly increased in unspayed canines [2,5]. Additionally, these tumours mostly affect dogs older than 8 years of age [6], with pure-blooded canines showing an increased risk of development [4,5]. Although there are several types of benign or malignant CMTs [7,8], the majority of tumours are malignant, with an incidence of 41–68% [9], and malignancy being highly correlated with increased dog age [10]. In veterinary medicine, classification of CMTs as either benign or malignant occurs at the histological study stage [11] since, unlike human medicine, conventional diagnostic ultrasound examinations cannot accurately characterise tumour malignancy [9,12,13]. Nevertheless, unlike conventional ultrasound, acoustic radiation force impulse elastography [13] or Doppler ultrasound [12] can potentially provide sufficient differentiation between benign and malignant CMTs [12,13].

CMTs are often considered the equivalent animal model of human breast cancer [2,12] since the appearance of such tumours in both groups is similarly hormonally dependent [14] with the tumours showing interchangeable biological behaviour [13,15]. However, despite the variety of therapies available for human breast cancer, a more limited number of treatment options exists for CMTs [5]. Surgical resection with complete margins is the gold standard for efficient treatment [2,5], achieving complete remission of benign tumours [5], while approximately half of the malignant tumours have been associated with metastasis [5] or recurrence [16]. Although similar to the treatment protocol of human breast cancer, adjuvant treatments such as chemotherapy, radiotherapy and hormonal therapy could potentially reduce the incidence of metastasis and recurrence, these are not routinely performed in veterinary medicine [5]. Radiotherapy combined with medication has only recently been utilised for the treatment of inflammatory mammary cancer [17], while hormonal therapy [18] and

more frequently, chemotherapy [19,20] have also been proposed for improving the outcome of CMTs. Nevertheless, these treatments also result in disease recurrences [17] or induce toxic effects [21] aside from lacking essential data regarding required doses [2].

Ultrasonic tissue characterisation with respect to attenuation, and propagation velocity provides increased information regarding the physical composition and nature of the tissue, thus enhancing current diagnostic and therapeutic applications of ultrasound [22]. Acoustic attenuation refers to distance-related energy losses emerging during ultrasonic propagation in tissue and has been associated with several pathological and physiological tissue properties [22]–[24]. Attenuation mechanisms are a combination of absorption, reflection and scattering, with absorption characterised the leading attenuation mechanism in soft tissues [24]. Especially in veterinary medicine, and specifically for CMTs, accurate attenuation estimations could potentially aid in establishing tumour benignity or malignancy following similar classification performed on human breast tumours [25]. Moreover, attenuation combined with other echogenic characteristics has been indicative of canine mammary tumour (CMT) malignancy [26], thus its estimation could potentially discriminate malignancy and determine the choice of treatment. In particular, surgery could be avoided in older dogs with deprived health [27]. Furthermore, employing novel targeted therapies already followed in human medicine, for the treatment of CMTs could provide increased benefits in companion dogs. For example, the recent use of High-Intensity Focused Ultrasound (HIFU) in the veterinary setting [28], characterised by the increasing development of several HIFU systems dedicated for veterinary applications [29–31], could soon be established as an alternative non-invasive treatment for mammary tumours in companion animals, sparing the need for stitches and the discomfort associated with an Elizabethan collar. In this regard, characterisation of CMTs based on their ultrasonic properties and particularly attenuation would potentially provide additional data required for the extension of current treatment management of canine mammary cancer. Moreover, because of the inherent similarities between canine mammary cancer and human breast cancer, accurate estimations of attenuation appear essential for providing increased data for comparative oncology, with CMTs potentially acting as an animal model for testing novel therapeutic and diagnostic ultrasound systems, ultimately advancing human medicine [2].

Since attenuation is considered a fundamental acoustic property of tissue, several immersion techniques have been progressively introduced for its experimental measurement. The pulse-echo technique employs a transmit-receive transducer and a high impedance reflector [32] while contrary, through-transmission techniques utilise one transmitting and one receiving transducer coaxially aligned [33,34]. These techniques are only suitable for in vitro measurements of attenuation since they require immersion of the tissue samples in a propagating medium, while in vivo measurements of tissue attenuation can be acquired by analysing backscattered signals from a conventional diagnostic ultrasound transducer [24,35].

Due to the importance of attenuation, the several techniques have been comprehensively utilised for attenuation measurements for several types of materials [36–39] as well as in vivo or in vitro measurements for various canine tissues, with canine myocardium being the most greatly reported [23,40–44]. Although CMTs are one of the primary tumours presenting in dogs [5], surprisingly no literature studies have been identified estimating their acoustic attenuation. Notably, attenuation measurements of canine tissues are often temperature-dependent, with different tissue types exhibiting a distinctive temperature-dependency [45]. Additionally, increasing temperature induces a dependence of attenuation on post-excision time [44], increasing with post-excision time, potentially as a result of tissue degradation [23,44]. Furthermore, measurements performed on canine myocardium have concluded a direct correlation of attenuation with collagen and an inverse correlation with water content [42].

More importantly, in vitro measurements of attenuation often employ the use of fixed samples since the fixation procedure, usually in formaldehyde liquid, ensures that any physical tissue properties are not severely altered. However, fixation of tissue specimens has often been reported to result in alterations in the measured acoustic properties, with formaldehyde concentration and fixation time having different effects [46]. Furthermore, tissue type has been reported to exhibit different effects on the dependency of acoustic properties on formalin fixation [40,46]. In particular, fixed canine spleen tissue specimens exhibited higher attenuation than fresh samples when measured at 4.5 MHz using a modified pulse-echo technique [40]. Contrary, fixing canine lung tissue samples in 40% formaldehyde did not significantly affect ultrasonic parameters since measured attenuation coefficients were similar between fixed [47] and fresh lung samples [48]. However, different experimental methods and temperatures were employed [47,48] leading to inconclusive results on the effect of fixation on canine lung tissue. Additionally, more importantly, attenuation of fixed samples measured as a function of frequency contradicted the linear attenuation increase with increasing frequency exhibited by fresh tissue [40,47]. As a result, large variations in the measured attenuation of the fixed samples [47] were observed, probably as a result of the fixation procedure affecting ultrasonic absorption and scattering.

The present study was inspired by the apparent absence in literature for data of acoustic attenuation of CMTs. As aforementioned, such data would be highly beneficial for better diagnosis, management and expansion of available treatments for CMTs that could potentially provide additional information regarding management of human breast carcinoma. Herein, we present experimental measurements for calculating the acoustic attenuation coefficient of excised malignant CMTs. The naturally occurring malignant mammary tumours were surgically removed from different dogs (n = 5) and experimental measurements of acoustic attenuation and ultrasonic propagation speed were performed ex vivo.

2. Materials and methods

2.1. Canine mammary tumours

Naturally occurring malignant mammary gland tumours were surgically removed by an experienced veterinarian surgeon during scheduled traditional surgeries performed on several companion dogs that presented with tumours and were brought by their owners to the veterinary clinic for treatment. A total of 3 malignant mammary gland tumours were individually acquired by the veterinarian surgeon from 3 canines. The excised tumour samples were placed in plastic sample containers where they were immersed in 38 % formaldehyde in aqueous solution. Immersion of the tumours in the fixation liquid was performed instantly after their excision, to ensure that any physical properties of the tumour samples would not be altered since tissue degradation presents upon the use of a lengthy timeframe between post-excision and specimen fixation [49]. The sample containers were supplied by the veterinarian surgeon to the laboratory premises for conduction of experimental measurements within a specific timeframe from the time of fixation. In this regard, all three tumour specimens were fixed for a duration of up to 72 h.

Upon their arrival at the laboratory, the tumour specimens (labelled A, B or C) were removed from the formaldehyde solution right before the conduction of the experiments. Fig. 1 shows the three surgically excised tumours. From each tumour specimen, several sample pieces from different locations were cut with 17 mm thicknesses to accommodate for the different morphology that was visually observed across the tumour specimen. In the majority of this manuscript, sample pieces sectioned from the same tumour specimen, are referred to with the tumour specimen label (either A, B or C) and the sectioned sample piece number (e.g. 1, 2).

A total of 5 sample pieces were then arranged in specially designed 3D-printed (FD270, Stratasys, Minnesota, USA) Acrylonitrile Butadiene
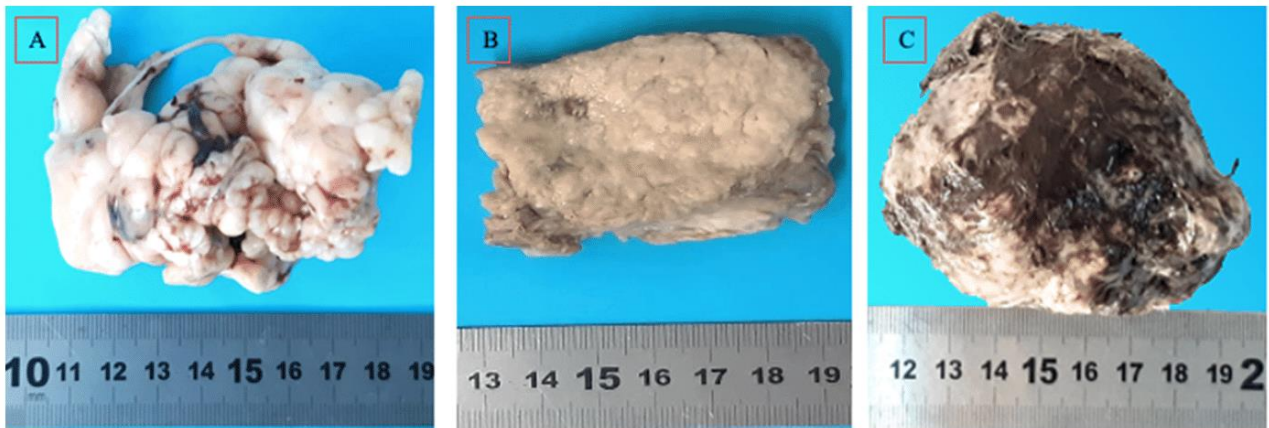
Fig. 1. Photo of the three surgically excised malignant CMTs fixed for up to 72 h. A) Tumour A, B) Tumour B, C) Tumour C.

Styrene (ABS) holders that were employed to accommodate the samples and restrict their movement during conduction of the experimental procedure. The holders additionally featured circular apertures on both sides to allow for propagation of the ultrasonic wave through the tumour samples. Fig. 2 shows a photo of the 5 different sample pieces of malignant CMTs as featured in the 3D-printed ABS holders.

2.2. Experimental measurements of ultrasonic propagation speed

Initially, measurements of the ultrasonic propagation speed for each tumour sample piece were performed utilising a standard widely employed pulse-echo technique [38]. Since this method is characterised as an immersion technique, experimental measurements were
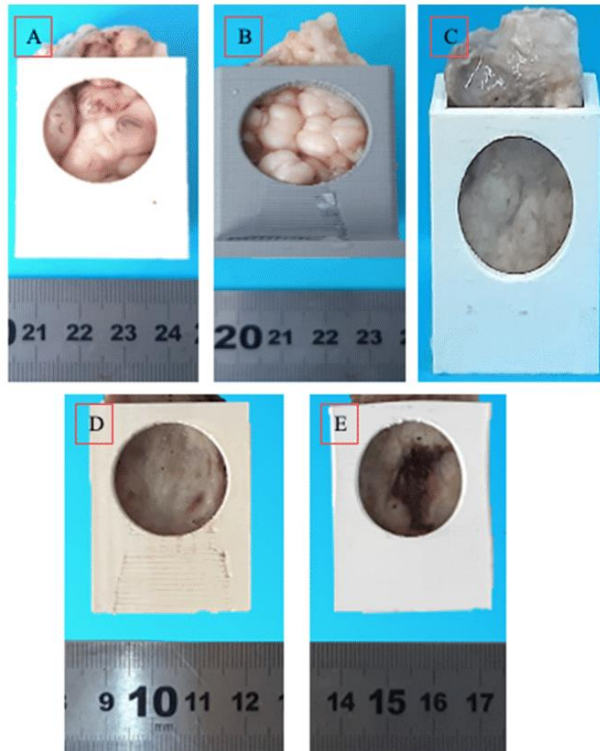

Fig. 2. Photo of the five sample pieces of malignant CMTs fixed for up to 72 h as arranged in the 3D printed ABS holders. A) Sample piece A.1, B) Sample piece A.2, C) Sample piece B.1, D) Sample piece C.1, E) Sample piece C.2.

implemented in an acrylic water tank filled with deionized water that had previously undergone degasification. All experimental measurements for ultrasonic speed were executed at a water temperature of 25 °C. An immersion planar ultrasonic transducer with a dynamic element diameter of 10 mm operating at a central frequency of 2.7 MHz (Piezo Technologies, Indianapolis, USA) working in transmit/receive mode was employed. The transducer transmitted sinusoidal ultrasonic waves that were generated by a pulser/receiver (500, PR, GE Panametrics, Waltham, USA). A specially designed 3D-printed (FD270, Stratasys) ABS holder was utilised to accommodate the transducer and each of the tumour samples in a coaxial alignment. The transducer was positioned on the ABS holder through a cylindrical cavity designed with a 10 mm diameter to provide a tight fit, thus offering stability to the transducer at the edge of the holder. Each of the tumour specimens was coaxially accommodated on a dedicated location in the middle of the 3D-printed holder. At the opposite end of the holder and close to the rear surface of the tumour sample, a thick aluminium metal plate was accommodated serving as a reflector. The ultrasonic waves coaxially propagated through each of the tumour samples and were then reflected by the aluminium plate. The pulser/receiver was connected to a digital oscilloscope (TDS 2012, Tektronix Inc., Oregon, USA) that was employed for the visualisation of the reflected signals received by the transducer. Fig. 3A shows the complete experimental set-up utilised for determining the ultrasonic propagation speed, while Fig. 3B provides a schematic representation of the 3D-printed holder indicating distances between the tumour sample and each of the transducer and reflector. The 17 mm thickness of the tumour samples was considered adequate for providing sufficient ultrasonic propagation time through the samples, thereby resulting in accurate measurements between zero-crossings of the reflected signals on the oscilloscope (TDS 2012, Tektronix Inc.).

Firstly, the propagation speed of ultrasound in water (c_{water}) was calculated by analysing the recorded oscilloscope echo signals arising from propagation of ultrasound between the transducer and the reflector in the water path, without the presence of the sample and using Equation (1) [38]:

$$c_{water} = \frac{2d}{t_{water}} \tag{1}$$

where d is the distance between the planar transducer and the metal reflector, set at 64 mm, while t_{water} represents the time required for the ultrasound beam to travel from the transducer to the metal reflector and back, determined by measuring transit time between zero-crossings of received echoes arising from reflections from the transducer-water and water-reflector interfaces. Thereafter, each of the tumour samples was correspondingly accommodated on the holder, between the transducer
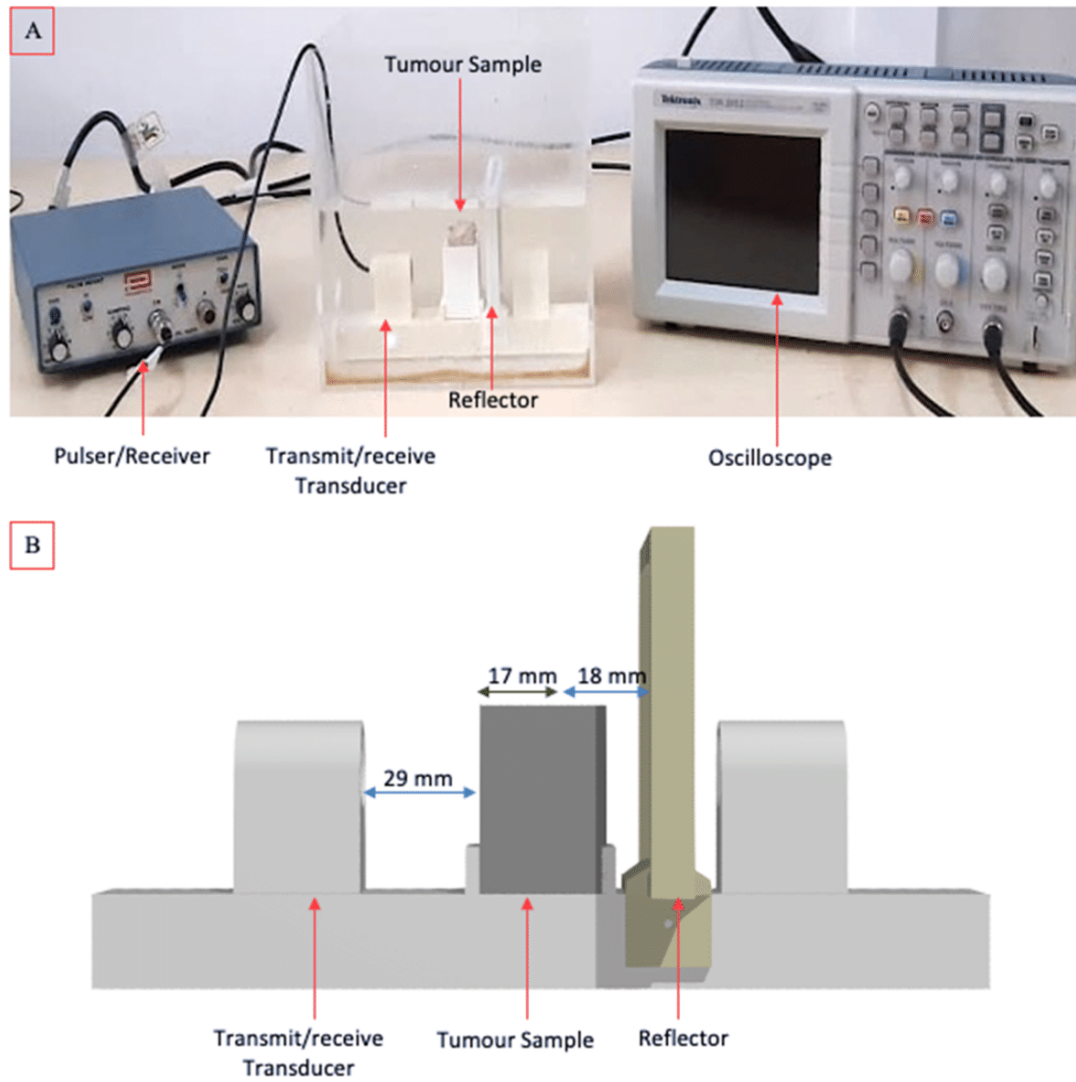
Fig. 3. A) Photo of the experimental set-up utilised for measurement of the ultrasonic propagation speed of the CMTs, B) Schematic representation of the experimental set-up indicating distances. Green arrow indicates sample thickness and blue arrows indicate transducer-sample and sample-reflector distances.

and the metal reflector, and the group velocity of ultrasound was calculated for each of the sample pieces by employing Equation (2) [39]:

$$c_{tumour} = c_{water} \left[\frac{(t_{water} - t_{tumour})}{\Delta t} + 1 \right] \tag{2}$$

where c_{water} is the propagation speed of ultrasound in water, measured as abovementioned, t_{water} is the time taken for propagation of ultrasound between the transducer and the reflector in the water path without the presence of the tumour sample measured from echoes as above-mentioned, t_{tumour} is the time of flight for ultrasound to cover the corresponding distance but with the tumour specimen accommodated on the holder and in the ultrasonic beam pathway, calculated from zero-crossings between echoes arising from the transducer-water and water-reflector interfaces during presence of the tumour specimen on the holder, while Δt is the time difference between the zero-crossings of the echo signals occurring from reflections between water and the rear and front interfaces of the tumour sample.

2.3. Experimental measurements of acoustic attenuation

Initially, the mass density of each different mammary tumour sample

was measured. A high-precision (± 0.01 g) digital scale (1479 V, Tanita Corporation, Tokyo, Japan) was utilised for precisely measuring the mass of each sample. The volume of each specimen was measured by immersing it in a volumetric tube (± 0.1 ml) filled with water and employing the water displacement method. Thereafter, the acoustic impedance Z of each tumour sample under investigation was calculated by using Equation (3):

$$Z = \rho . c_{tumour} \tag{3}$$

where ρ is the measured mass density of the corresponding tumour sample and c_{tumour} is the experimentally estimated propagation velocity of ultrasound within each tumour under investigation.

The reflection coefficient R for each investigated tumour sample arising from the interaction of the ultrasonic wave with the tumour-water interface was calculated by employing Equation (4):

$$R = \left(\frac{Z_1 - Z_2}{Z_1 + Z_2} \right)^2 \tag{4}$$

where Z_1 is the acoustic impedance of water, calculated by using Equation (3) and multiplying water density with the acoustic

propagation speed in water, while Z_2 is the characteristic acoustic impedance as estimated for each tumour sample under investigation. Thereafter, the ultrasonic transmission coefficient T for each tumour specimen was estimated by introducing its characteristic estimated reflection coefficient R in Equation (5):

$$T = 1 - R \qquad (5)$$

The acoustic attenuation of each mammary tumour specimen was measured utilising a conventional through-transmission technique which has been extensively reported for in vitro measurements of ultrasonic attenuation of several tissues [23,42,43,50,51]. For experimental measurements, the tumour samples were immersed in a larger acrylic water tank than the one utilised for experimental measurement of the ultrasonic propagation speed and an enlarged identical ABS holder was 3D-printed (FD270, Stratasys) and employed. All experimental measurements were implemented at 25 °C degassed water.

Two identical immersion planar transducers, having the same gain and response, with an active element diameter of 30 mm and operating at a frequency of 1.1 MHz (MEDSONIC, Limassol, Cyprus) were introduced on the two opposite ends of the 3D-printed holder. The identical transducers were coaxially aligned on the holder with their active elements directly facing each other. Two ABS enclosures were 3D-printed (FD270, Stratasys) for accommodating the two planar transducers on the cylindrical cavities of the 3D-printed holder. Each enclosure provided a rigid fit with both the cylindrical cavity of the 3D-printed holder and either of the two planar transducers, ensuring a secure collinear arrangement of the larger diameter transducers during experimental measurements for attenuation. One of the two identical planar transducers operated in a transmit mode thus it was connected to a function generator (TG550, Thurlby Thandar Instruments, Huntingdon, UK) that continuously sent a sinusoidal ultrasonic wave to the planar transmit transducer. The second planar transducer operated in a receive mode and was connected to the digital oscilloscope (TDS 2012, Tektronix Inc.) for visualising and analysing the received attenuated signal. Fig. 4 shows the experimental set-up utilised for measurements of the acoustic attenuation coefficient. Considering the distances between the transmitting transducer and the tumour sample as shown in Fig. 4, attenuation measurements were performed in the near-field of the transmitting transducer.

Firstly, voltage wave signals were recorded for propagation of ultrasound in the water path. Thereafter, the mammary tumour sample under evaluation was accommodated on a location on the 3D printed holder, between the planar transducers. The attenuated voltage wave signals were recorded in the presence of the tumour specimen in the pathway of the ultrasonic beam. The attenuation coefficient α_{tumour} of

the investigated mammary tumour specimen was calculated by using the following Equation (6) [39]:

$$\alpha_{tumour} = \alpha_{water} + \frac{20 log e}{x} * ln\left(\frac{A_{water}}{A_{tumour}} T\right) \qquad (6)$$

where α_{water} is the acoustic attenuation of water, A_{water} is the voltage wave signal recorded for ultrasound propagation in the water path, A_{tumour} is the attenuated voltage wave signal recorded with the presence of the mammary tumour sample between the transducers, T is the estimated transmission coefficient of the investigated tumour sample, while x is the thickness of the tumour sample (17 mm) as measured utilising a digital caliper (ROHS NORM 2002/95/EC).

For each tumour sample, three individual measurements of both the signals in the water path and attenuated signals in presence of the tumour were recorded and thus three calculations of the attenuation coefficient were implemented. The rationale for performing three calculations was to ensure the precision of the experimental measurement and examine any variations arising between individual measurements for the attenuation coefficient of each tumour sample.

2.4. Histology study

The samples of CMTs were sent for histological examination to an advanced histopathological and cytological centre. The samples were embedded in paraffin, sectioned and stained with Haematoxylin and Eosin (H&E). Thereafter, histology slides were examined by an experienced histopathologist utilising a microscope (Olympus BX51, Shinjuku City, Tokyo, Japan) for microanatomically examining the cell morphology of the mammary tumour samples and providing pathology details on tissue structure. The histology results were digitally saved as virtual slides using a small capacity brightfield slide scanner (VENTANA DP 200, Roche Diagnostics International AG, Rotkreuz, Switzerland).

3. Results

3.1. Experimental measurements of ultrasonic propagation speed

The propagation velocity of ultrasound in degassed water at a temperature of 25 °C was experimentally measured as 1497.6 ± 6.6 m/s at a frequency of 2.7 MHz. Correspondingly, the ultrasonic propagation speeds as measured for each of the five sample pieces acquired from the three tumour specimens are shown in Table 1. As visually observed from the data, variations in ultrasonic speed seemed to exist between the five sample pieces and notably between sample pieces acquired from different locations of a single CMT specimen. Approximately a 3 %
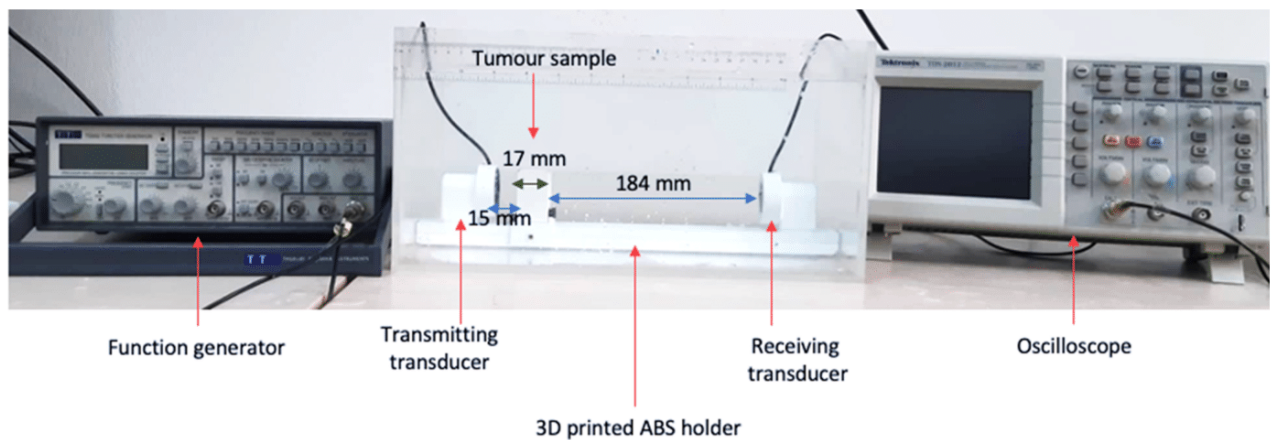

Fig. 4. Photo of the experimental set-up utilised for measurement of the acoustic attenuation of the CMTs. Green arrow indicates sample thickness and blue arrows indicate transducer-sample distances.

Table 1

Ultrasonic propagation speeds of the five sample pieces of CMTs fixed for up to 72 h as measured at 25 °C for a frequency of 2.7 MHz.

Tumour sample piece	Ultrasonic propagation speed (m/s)
A.1	1587 ± 7.4
A.2	1633 ± 7.9
B.1	1568 ± 7.8
C.1	1596 ± 7.6
C.2	1636 ± 7.6

Table 3

Average acoustic attenuation of the five sample pieces of CMTs fixed for up to 72 h as measured at 25 °C at a frequency of 1.1 MHz.

Tumour sample piece	Acoustic attenuation (dB/cm) at 1.1 MHz	Acoustic attenuation (dB/cm. MHz)
A.1	2.43 ± 0.05	2.21 ± 0.05
A.2	3.79 ± 0.06	3.45 ± 0.06
B.1	2.15 ± 0.05	1.95 ± 0.05
C.1	2.14 ± 0.08	1.95 ± 0.08
C.2	2.91 ± 0.09	2.65 ± 0.09

difference existed between ultrasonic propagation speeds of the two sample pieces acquired from different locations from a single mammary tumour specimen (A.1 & A.2 or C.1 & C.2).

3.2. Experimental measurements of acoustic attenuation

The mass density of the five sample pieces was calculated as 900 ± 22.6 kg/m³, 900 ± 22.6 kg/m³, 1166.7 ± 19.5 kg/m³, 933 ± 31.3 kg/m³ and 933 ± 31.3 kg/m³ for tumour samples A.1, A.2, B.1, C.1 and C.2 respectively. Notably, the mass density of the sample pieces acquired from the same mammary tumour specimen did not seem to vary between the different sectioned sample pieces. For each sample piece, the estimated mass density and the ultrasonic propagation speed were utilised for calculating the characteristic acoustic impedance of the investigated tumour sample. The characteristic acoustic impedance of degassed water was calculated as 1.49 ± 0.001 MRayl by utilising the ultrasonic propagation speed in water as experimentally estimated in the present study and the literature value for the density of water (997 kg/m³) [52]. Thereafter the characteristic acoustic impedances of both water and each of the tumour pieces were utilised to calculate the reflection and transmission coefficients of each tumour sample piece. Table 2 shows the acoustic impedance, reflection and transmission coefficients as estimated for each of the tumour sample pieces. As observed, both the acoustic impedance and reflection coefficients varied among the five sample pieces. Furthermore, small variations in either the reflection coefficients or acoustic impedances existed between sample pieces acquired from different locations of the same tumour specimen.

At the frequency of 1.1 MHz, the acoustic attenuation of water was estimated as 0.0024 dB/cm by multiplying the literature value of the attenuation coefficient of water (0.0022 dB/cm.MHz) [53] with the operating frequency of the transducer (1.1 MHz). Three individual measurements of the attenuation coefficient were implemented for each tumour sample piece, and the average attenuation was calculated from these three measurements. Table 3 shows the average attenuation coefficient for each of the tumour sample pieces as directly calculated in dB/cm from introduction of all required variables in Equation (6). Moreover, the attenuation coefficient is also provided in dB/cm.MHz by simply dividing with the operating frequency (1.1 MHz). Large variations in the average attenuation values were observed between the five sample pieces. Moreover, variations in the average attenuation coefficient were present between sample pieces acquired from a single mammary tumour specimen, reaching up to 56 % difference for pieces acquired from different locations of the same mammary tumour (A.1 and A.2).

Table 2

Acoustic impedance, reflection and transmission coefficients of the five sample pieces of CMTs fixed for up to 72 h.

Tumour sample piece	Acoustic impedance Z (MRayl)	Reflection coefficient	Transmission coefficient
A.1	1.43 ± 0.04	0.0005	0.9995
A.2	1.47 ± 0.04	0.0001	0.9999
B.1	1.83 ± 0.03	0.0101	0.9899
C.1	1.49 ± 0.05	0	1
C.2	1.53 ± 0.05	0.0001	0.9999

3.3. Histology study

Fig. 5 shows a representative example of a histological result of the cellular structure of CMT, with similar pathological results on tissue structure obtained for the three tumour specimens. The histology studies revealed the presence of polymorphic cells and areas of heterogeneity across the mammary tumour samples as indicatively shown with labelled areas (A-E), on Fig. 5. The characteristic cluster arrangement of the epithelial cells as shown with areas labelled with A on the histology slide, established the malignant nature of the tumour specimens. The large-scale light pink-stained areas on the histology study (B) indicated that the tumour specimens were mostly collagen rich, while the bright-pink stained areas (C) showed that in large parts, the tumours contained areas of necrosis. Similarly, the bright purple-stained areas (D) revealed that a smaller but still significant part of the tumour samples consisted of glandular tissue, while in minimal parts the tumours contained fat areas as indicated by the circular voids appearing on the histology slide (E).

4. Discussion

The current study focused on the ex vivo experimental measurement of acoustic attenuation of five malignant CMT samples to replenish the existing paucity in the literature for ultrasonic tissue characterisation of these types of tumours. The five samples were sectioned from three naturally occurring malignant CMTs acquired through traditional surgical excision from different dogs and fixed in formaldehyde for a duration of up to 72 h. Acquisition of several sample pieces from each tumour was considered essential for examining any correlation of ultrasonic attenuation and velocity with the visually observed varied morphology of the outer surface of each tumour specimen.

Herein, experimental measurements of the attenuation coefficient and propagation speed of the tumour specimens were performed following the majority of literature studies that utilise the through-transmission [42,44,45,50,51] and pulse-echo techniques [54] for respectively measuring in vitro the attenuation and propagation speed of a variety of canine tissues. Experimental measurements for the ultrasonic propagation speed of degassed water as measured herein at 25 °C for a frequency of 2.7 MHz, resulted in a value (1497.6 m/s) which is well in accordance with reported literature values for ultrasonic speed in water of this specific temperature [45,55,56]. Correspondingly, the range of ultrasonic propagation speeds (1568–1636 m/s) of the five malignant CMT samples as reported in the present study at 2.7 MHz is marginally higher than previous in vitro measurements of ultrasonic speed for canine liver, kidney, muscle and prostate tissues [45]. Measurements performed for these canine tissues over a similar frequency (3 MHz) and temperature (25 °C) with the current study, reported values in the range of 1545–1576 m/s [45], thereby indicating that malignant CMTs exhibit higher ultrasonic velocities than other canine tissues. Similarly, the propagation speed reported for CMTs is significantly higher than the acoustic propagation speed reported for excised [57] and in vivo human breast tissue [58–60] as well as benign human breast tumours [60]. Nevertheless, the range of speeds reported for the CMTs is slightly higher than the respective values reported for excised [61] and in vivo malignant human breast tumours (1548 ± 17 m/s) [60], thereby
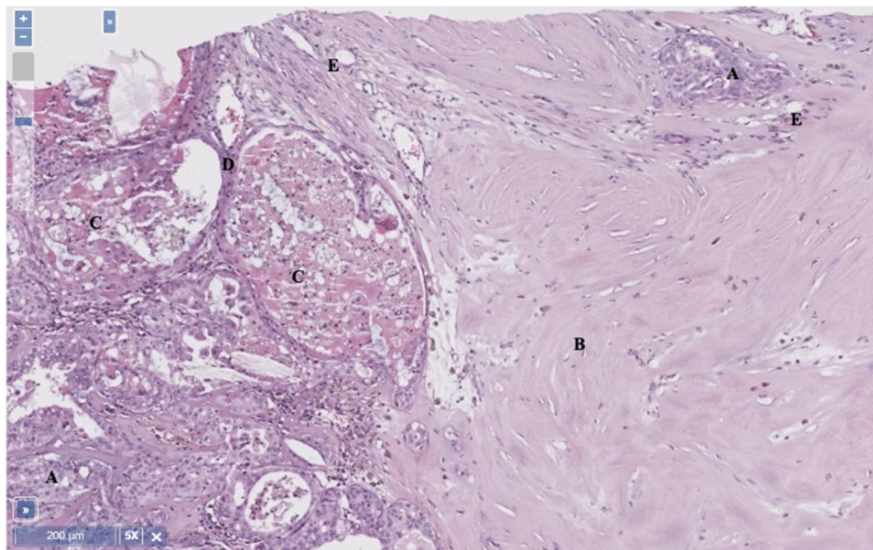
Fig. 5. Histology slide of canine mammary tumour (H&E 40 ×). Labelled areas show indicative areas of heterogeneity and polymorphism. Cluster arrangement of epithelial cells indicates malignant nature (A) of tumour with collagen (B), necrotic (C), glandular (D) and fat (E) areas.

suggesting possible similarities between acoustic properties of malignant CMTs and human breast tumours.

Notably, significant variations (~3%) in ultrasonic propagation speed existed between different sample pieces acquired from the same tumour specimen, thus corroborating a correlation of ultrasonic speed with the varied tumour morphology. Nevertheless, no specific relation of tumour morphology with ultrasonic speed was examined. The relation of ultrasonic speed with the different tumour morphology indicated herein, is corroborated by previous in vitro measurements of ultrasonic speed of canine kidney tissue that reported significant speed variations along the kidney, attributed to structural inhomogeneities [45].

Remarkably, despite morphological variations encountered along CMT specimens, the mass density of different pieces sectioned from varied locations across each of the mammary tumours did not vary. Mass densities of the CMT specimens were in the range of 900–1166.7 kg/m^3, analogous to mass density values reported for canine muscle tissue [62] and well in the range of mass densities reported for human breast tissue [63] and breast cancer [64]. This validates the characteristic similarities in physical properties exhibited between CMTs and human breast cancer, thereby further indicating that CMTs can act as an animal model.

The characteristic impedance of degassed water (1.49 MRayl) as calculated within the scopes of the present study was approximately similar to the corresponding value of 1.48 MRayl reported in the literature [65]. Furthermore, it was demonstrated that the acoustic impedance of the five sample pieces exhibited variations among different samples, with the values being similar to acoustic impedances reported for canine muscle (1.40–1.46 MRayl), liver (1.64–1.75 MRayl), and heart tissues (1.64–1.78 MRayl) [66]. The acoustic impedance of a single tumour specimen (1.83 MRayl) was greater than the other sample pieces and marginally higher than the reported literature range for acoustic impedances of other canine tissues [66], attributed to the slightly higher density (1166.7 kg/m^3) measured for the specific tumour specimen. Remarkably, variations in acoustic impedances observed between sample pieces acquired from the same tumour specimen contradicted the uniform acoustic impedance observed throughout several normal canine tissues [66]. Nevertheless, contrary to normal tissues, CMTs exhibit a high heterogeneity [27] and the morphology can vary across a specific tumour [5] as evidenced from the herein histological studies, thus further validating the relation of the tumour morphology with varied acoustic properties observed in the current study.

To the best of our knowledge, no literature data on the acoustic attenuation of CMTs exist, thereby calculation of the reflection and transmission coefficients of each mammary tumour was considered essential for accounting for ultrasonic energy lost because of possible reflection arising between the water-tumour interface. Varied reflection coefficients were observed between the five tumour pieces with the majority exhibiting only minimal reflection and only a single sample exhibiting a higher reflection coefficient. Nevertheless, all reflection coefficients were minor, indicating that the majority of acoustic attenuation of CMTs is due to absorption and scattering arising in the interior of the samples as already suggested by attenuation studies of normal canine tissues [24,67].

Employment of the through-transmission technique for measuring the acoustic attenuation of the five sample pieces of malignant CMTs was performed at 1.1 MHz instead of the higher frequency utilised in measurements of the propagation speed. The large variations in the attenuation values of the five samples (1.95–3.45 dB/cm.MHz) as well as variations from 36 % to 56 % observed between sample pieces acquired from varied locations across a single tumour further confirm the effect of the varied morphology on the acoustic properties of the tumour, thus being in accordance with studies performed on canine skin where variations in measured attenuation existed as a consequence of heterogeneity among samples [68]. Additionally, the large variations in attenuation values of CMTs corroborate similar large variations observed between values of acoustic attenuation of human malignant breast tumours [25]. Furthermore, the measured attenuation coefficients of the five mammary tumour samples have been found considerably higher upon comparison with attenuation values previously reported for canine liver [50,51], kidney [40,50,51], muscle [51], normal [40] and infarcted myocardium [23,40,42,43] during in vitro measurements executed at corresponding temperatures and following similar techniques with those in the present study. Nevertheless, the lower attenuation values of CMTs as reported herein, are slightly higher than the attenuation coefficient of excised human breast tissue [57,59] as well as higher than attenuation values reported for in vivo benign [25,69] and malignant human breast tumours [25,69].

The significantly higher attenuation values for CMTs were attributed to the increased heterogeneity of the tumour specimens, and the presence of polymorphic cells as evidenced from the performed histology studies. Furthermore, CMTs have been reported to contain areas of necrosis, fibrous tissue, and bone [70,71], thereby explaining the increased attenuation values presented herein and the variations in attenuation values observed across a single tumour. This was evidenced from the histology studies that showed a heterogeneous distribution of areas of

necrosis, collagen, glandular and fat tissues across the tumour speci-mens, with these areas differently affecting attenuation depending on their distribution along the ultrasonic beam path. Additionally, considering that in vitro studies on canine skin [68,72] and myocardium [23,43] have reported a direct relation of increased attenuation of these tissues with an increased percentage of collagen, and CMTs often exhibit more collagen than non-neoplastic tissue [73] with the CMTs of the present study being collagen rich as evidenced from the histology studies, would further justify the increased values for acoustic attenu-ation of CMTs presented in this study.

Furthermore, considering the variations in attenuation values and the small sample size utilised in the present study, no characteristic relations between acoustic attenuation and either mass density or propagation speed could be deduced for the CMTs. Additionally, in vitro studies previously performed have indicated that the fixation procedure alters the ultrasonic properties of tissue [46], with the formaldehyde concentration, fixation time and tissue type exhibiting different effects [40,46]. However, since previous studies [46,47] examining the effect of fixation on acoustic properties performed measurements in both fixed and fresh specimens, and no literature studies exist reporting measure-ments for acoustic properties of fresh CMTs, the effect of fixation on the acoustic properties of CMTs could not be examined.

Results presented within the scope of this study could aid in enhancing the diagnostic and therapeutic uses of ultrasound for the management of CMTs as well as provide data for potentially acting as an animal model for the advancement of human medicine. Acoustic prop-erties of malignant CMTs as measured herein, have demonstrated similar propagation speed and higher attenuation coefficient than human breast cancer. Since attenuation is considered the main mecha-nism of ultrasonic energy loss, thus determining the success of HIFU treatment [74], values presented for CMTs could be potentially used for determining ultrasonic protocols for HIFU treatment of mammary tu-mours in dogs. Previous employment of HIFU in the veterinary setting did not result in successful outcomes in CMT [28], probably as a result of the high attenuation of CMTs as indicated in the current study. In this regard, the present results could be employed to result in successful HIFU treatments in CMTs. Additionally, due to similarities found be-tween acoustic properties of CMTs and human breast tumours, the re-sults presented herein, could be potentially employed in the development and preclinical testing of HIFU systems dedicated for breast cancer treatment thereby advancing human medicine. The pre-sent study could be further enhanced by performing measurements in excised normal canine mammary tissue as well as fresh CMT specimens.

Declaration of Competing Interest

The authors declare that they have no known competing financial interests or personal relationships that could have appeared to influence the work reported in this paper.

References

[1] K. Sorenmo, Canine mammary gland tumors, Veterinary Clinics of North America - Small Animal Practice, 33(3), 2003, 10.1016/S0195-5616(03)00020-2.

[2] G. Valdivia, Á. Alonso-Diez, D. Pérez-Alenza, L. Peña, From Conventional to Precision Therapy in Canine Mammary Cancer: A Comprehensive Review, Front. Veterinary Sci., 8. 2021, 10.3389/fvets.2021.623800.

[3] D.F. Merlo, et al., Cancer incidence in pet dogs: Findings of the animal tumor registry of Genoa, Italy, J. Vet. Intern. Med., 22(4), 2008, 10.1111/j.1939-1676.2008.0133.x.

[4] C.F. Saba, K.S. Rogers, S.J. Newman, G.E. Mauldin, D.M. Vail, Mammary gland tumors in male dogs, J. Vet. Intern. Med., 21(5), 2007, 10.1892/0891-6640(2007) 21[1056:MGTIMD]2.0.CO;2.

[5] N. Sleeckx, H. de Rooster, E.J.B. Veldhuis Kroeze, C. van Ginneken, L. van Brantegem, Canine mammary tumours, an Overview, Reproduction in Domestic Animals, 46(6), 2011, 10.1111/j.1439-0531.2011.01816.x.

[6] K.U. Sorenmo, R. Rasotto, V. Zappulli, M.H. Goldschmidt, Development, anatomy, histology, lymphatic drainage, clinical features, and cell differentiation markers of canine mammary gland neoplasms, Vet. Pathol., 48(1), 2011, 10.1177/ 0300985810389480.

[7] M.H. Goldschmidt, L. Peña, R. Rasotto, V. Zappulli, Classification and grading of canine mammary tumors, Vet. Pathol., 48(1), 2011, 10.1177/0300985810393258.

[8] S. Murphy, Mammary tumours in dogs and cats, In Pract., 30(6), 2008, 10.1136/ inpract.30.6.334.

[9] S.B. Mülazimoğlu, et al., B-mode echotexture analysis and color doppler sonography in canine mammary tumors, Kafkas Univ. Vet. Fak. Derg., 22(6), 2016, 10.9775/kvfd.2016.15686.

[10] K.U. Sorenmo, et al., Canine mammary gland tumours; a histological continuum from benign to malignant; clinical and histopathological evidence, Vet. Comp. Oncol., 7(3), 2009, 10.1111/j.1476-5829.2009.00184.x.

[11] M.A.R. Feliciano, A.S. Silva, R.V.R. Peixoto, P.D. Galera, W.R.R. Vicente, Clinical, histopathological and immunohistochemical study of mammary neoplasm in bitches, Arq. Bras. Med. Veterinária e Zootec. 64 (5) (Oct. 2012) 1094–1100, https://doi.org/10.1590/S0102-09352012000500002.

[12] M.A.R. Feliciano, W.R.R. Vicente, M.A.M. Silva, Conventional and Doppler ultrasound for the differentiation of benign and malignant canine mammary tumours, J. Small Anim. Pract., 53(6), 2012, 10.1111/j.1748-5827.2012.01227.x.

[13] M.A.R. Feliciano, et al., Ultrasonography methods for predicting malignancy in canine mammary tumors, PLoS One, 12(5), 2017, 10.1371/journal.pone.0178143.

[14] J. Thuróczy, G.J.K. Reisvaag, E. Perge, A. Tibold, J. Szilágyi, L. Balogh, Immunohistochemical detection of progesterone and cellular proliferation in canine mammary tumours, J. Comp. Pathol., 137(2–3), 2007, 10.1016/j. jcpa.2007.05.005.

[15] E. Jensen-Jarolim, et al., Crosstalk of carcinoembryonic antigen and transforming growth factor-β via their receptors: Comparing human and canine cancer, Cancer Immunology, Immunotherapy, 64(5), 2015, 10.1007/s00262-015-1684-6.

[16] N. Stratmann, K. Failing, A. Richter, A. Wehrend, Mammary tumor recurrence in bitches after regional mastectomy, Vet. Surg., 37(1), 2008, 10.1111/j.1532-950X.2007.00351.x.

[17] F. Rossi, S. Sabattini, M. Vascellari, L. Marconato, The impact of toceranib, piroxicam and thalidomide with or without hypofractionated radiation therapy on clinical outcome in dogs with inflammatory mammary carcinoma, Vet. Comp. Oncol., 16(4), 2018, 10.1111/vco.12407.

[18] P. Lombardi, S. Florio, U. Pagnini, A. Crispino, L. Avallone, Ovarian function suppression with a GnRH analogue: D-ser(But[t])[6]-Arzgly10]-LHRH (Goserelin) in hormone dependent canine mammary cancer, J. Vet. Pharmacol. Ther., 22(1), 1999, 10.1046/j.1365-2885.1999.00184.x.

[19] L. Marconato, R.M. Lorenzo, F. Abramo, A. Ratto, E. Zini, Adjuvant gemcitabine after surgical removal of aggressive malignant mammary tumours in dogs, Vet. Comp. Oncol., 6(2), 2008, 10.1111/j.1476-5829.2007.00143.x.

[20] M. Clemente, P.J. De Andrés, L. Peña, M.D. Pérez-Alenza, Survival time of dogs with inflammatory mammary cancer treated with palliative therapy alone or palliative therapy plus chemotherapy, Vet. Rec., 165(3), 2009, 10.1136/ vetrec.165.3.78.

[21] X. Zambrano-Estrada, et al., Molecular iodine/doxorubicin neoadjuvant treatment impair invasive capacity and attenuate side effect in canine mammary cancer, BMC Vet. Res., 14(1), 2018, 10.1186/s12917-018-1411-6.

[22] J. Chen, G.Y. Hou, F. Marquet, Y. Han, F. Camarena, E. Konofagou, Radiation-force-based estimation of acoustic attenuation using harmonic motion imaging

(HMI) in phantoms and in vitro livers before and after HIFU ablation, Phys. Med. Biol., 60(19), 2015, 10.1088/0031-9155/60/19/7499.

[23] M. O'Donnell, J.W. Mimbs, J.G. Miller, The relationship between collagen and ultrasonic attenuation in myocardial tissue, J. Acoust. Soc. Am., 65(2), 1979, 10.1121/1.382352.

[24] R.T. O'Brien, J.A. Zagzebski, Z.F. Lu, H. Steinberg, Measurement of acoustic backscatter and attenuation in the liver of dogs with experimentally induced steroid hepatopathy, Am. J. Vet. Res., 57(12), 1996.

[25] K. Nam, J.A. Zagzebski, T.J. Hall, Quantitative assessment of in vivo breast masses using ultrasound attenuation and backscatter, Ultrason. Imaging, 35(2), 2013, 10.1177/0161734613480281.

[26] C. Marquardt, E. Burkhardt, K. Failing, A. Wehrend, Sonographic examination of mammary tumors in bitches. Part 1: Individual criteria detectable by sonography and their correlation with tumor dignity, Tierarztl. Prax. Ausgabe K Kleintiere - Heimtiere, 31(5), 2003, 10.1055/s-0037-1622367.

[27] M. Soler, et al., Comparison between ultrasonographic findings of benign and malignant canine mammary gland tumours using B-mode, colour Doppler, power Doppler and spectral Doppler, Res. Vet. Sci. 107 (2016), https://doi.org/10.1016/j.rvsc.2016.05.015.

[28] M.O. Ryu, S.H. Lee, J.O. Ahn, W.J. Song, Q. Li, H.Y. Youn, Treatment of solid tumors in dogs using veterinary high-intensity focused ultrasound: A retrospective clinical study, Vet. J. 234 (2018), https://doi.org/10.1016/j.tvjl.2018.02.019.

[29] K. Spanoudes, N. Evripidou, M. Giannakou, T. Drakos, G. Menikou, C. Damianou, A high intensity focused ultrasound system for veterinary oncology applications, J. Med. Ultrasound, 29(3), 2021, 10.4103/JMU.JMU_130_20.

[30] T. Drakos, et al., MRI-Guided Focused Ultrasound Robotic System for Preclinical use, J. Vet. Med. Anim. Sci., 4(1), 2020.

[31] T. Drakos, M. Giannakou, G. Menikou, C. Damianou, Magnetic Resonance Imaging–Guided Focused Ultrasound Positioning System for Preclinical Studies in Small Animals, J. Ultrasound Med., 40(7), 2021, 10.1002/jum.15514.

[32] A.W. Nolle, S.C. Mowry, Measurement of Ultrasonic Bulk-Wave Propagation in High Polymers, J. Acoust. Soc. Am. 20 (4) (1948) 432–439, https://doi.org/10.1121/1.1906394.

[33] S. Umchid, Frequency dependent ultrasonic attenuation coefficient measurement, pp. 234–238, 2008.

[34] P. He, J. Zheng, Acoustic dispersion and attenuation measurement using both transmitted and reflected pulses, Ultrasonics 39 (1) (2001) 27–32, https://doi.org/10.1016/S0041-624X(00)00037-8.

[35] C. Guittet, F. Ossant, J.P. Remenieras, L. Pourcelot, M. Berson, High-frequency estimation of the ultrasonic attenuation coefficient slope obtained in human skin: Simulation and in vivo results, Ultrasound Med. Biol., 25(3), 1999, 10.1016/S0301-5629(98)00176-8.

[36] T. Drakos, et al., Ultrasonic attenuation of an agar, silicon dioxide, and evaporated milk gel phantom, J. Med. Ultrasound 29 (4) (2021) 239–249.

[37] T. Drakos, M. Giannakou, G. Menikou, G. Constantinides, C. Damianou, Characterization of a soft tissue-mimicking agar/wood powder material for MRgFUS applications, Ultrasonics 113 (2021), https://doi.org/10.1016/j.ultras.2021.106357.

[38] G. Menikou, C. Damianou, Acoustic and thermal characterization of agar based phantoms used for evaluating focused ultrasound exposures, J. Ther. Ultrasound 5 (1) (2017) 1–14, https://doi.org/10.1186/s40349-017-0093-z.

[39] A. Antoniou, N. Evripidou, M. Giannakou, G. Constantinides, C. Damianou, Acoustical properties of 3D printed thermoplastics, J. Acoust. Soc. Am., 149(4), 2021, 10.1121/10.0004772.

[40] M.P. Kadaba, P.K. Bhagat, V.C. Wu, Attenuation and Backscattering of Ultrasound in Freshly Excised Animal Tissues, IEEE Trans. Biomed. Eng., BME-27(2), 1980, 10.1109/TBME.1980.326710.

[41] J.W. Mimbs, M. O'Donnell, J.G. Miller, B.E. Sobel, Changes in ultrasonic attenuation indicative of early myocardial ischemic injury, Am. J. Physiol. - Hear. Circ. Physiol., 5(2), 1979, 10.1152/ajpheart.1979.236.2.h340.

[42] M. O'Donnell, J.W. Mimbs, J.G. Miller, Relationship between collagen and ultrasonic backscatter in myocardial tissue, J. Acoust. Soc. Am., 69(2), 1981, 10.1121/1.385433.

[43] J.W. Mimbs, M. O'Donnell, D. Bauwens, J.W. Miller, B.E. Sobel, The dependence of ultrasonic attenuation and backscatter on collagen content in dog and rabbit hearts, Circ. Res., 47(1), 1980, 10.1161/01.RES.47.1.49.

[44] M. O'Donnell, J.W. Mimbs, B.E. Sobel, J.G. Miller, Ultrasonic attenuation of myocardial tissue: Dependence on time after excision and on temperature, J. Acoust. Soc. Am., 62(4), 1977, 10.1121/1.381600.

[45] U. Techavipoo, T. Varghese, J.A. Zagzebski, T. Stiles, G. Frank, Temperature Dependence of Ultrasonic Propagation Speed and Attenuation in Canine Tissue, Ultrason. Imaging 24 (2002) 246–260.

[46] J.C. Bamber, C.R. Hill, J.A. King, F. Dunn, Ultrasonic propagation through fixed and unfixed tissues, Ultrasound Med. Biol., 5(2), 1979, 10.1016/0301-5629(79)90084-X.

[47] T.J. Bauld, H.P. Schwan, Attenuation and reflection of ultrasound in canine lung tissue, J. Acoust. Soc. Am., 56(5), 1974, 10.1121/1.1903488.

[48] F. Dunn, Attenuation and speed of ultrasound in lung, J. Acoust. Soc. Am., 56(5), 1974, 10.1121/1.1903489.

[49] M. van Seijen, et al., Impact of delayed and prolonged fixation on the evaluation of immunohistochemical staining on lung carcinoma resection specimen, Virchows Arch., 475(2), 2019, 10.1007/s00428-019-02595-9.

[50] U. Techavipoo, T. Varghese, Q. Chen, T.A. Stiles, J.A. Zagzebski, G.R. Frank, Temperature dependence of ultrasonic propagation speed and attenuation in excised canine liver tissue measured using transmitted and reflected pulses, J. Acoust. Soc. Am. 115 (6) (2004) 2859–2865, https://doi.org/10.1121/1.1738453.

[51] C.A. Damianou, N.T. Sanghvi, F.J. Fry, R. Maass-Moreno, Dependence of ultrasonic attenuation and absorption in dog soft tissues on temperature and thermal dose, J. Acoust. Soc. Am. 102 (1) (1997) 628–634, https://doi.org/10.1121/1.419737.

[52] W.B. Floriano, M.A.C. Nascimento, Dielectric constant and density of water as a function of pressure at constant temperature, Brazilian J. Phys., 34(1), 2004, 10.1590/S0103-97332004000100006.

[53] M.C. Ziskin, Fundamental physics of ultrasound and its propagation in tissue, Radiographics 13 (3) (1993) 705–709, https://doi.org/10.1148/radiographics.13.3.8316679.

[54] T. Bowen, W.G. Connor, R.L. Nasoni, A.E. Pifer, R.R. Sholes, Measurement of the temperature dependence of the velocity of ultrasound in soft tissues, Ultrason. tissue Charact. II 525 (1979) 57–61.

[55] V.A. Del Grosso, C.W. Mader, Speed of Sound in Pure Water, J. Acoust. Soc. Am., 52(5B), 1972, 10.1121/1.1913258.

[56] J. Lubbers, R. Graaff, A simple and accurate formula for the sound velocity in water, Ultrasound Med. Biol., 24(7), 1998, 10.1016/S0301-5629(98)00091-X.

[57] M. Sanchez, V. Barrere, I. Treilleux, N. Chopin, D. Melodelima, Development of a noninvasive HIFU treatment for breast adenocarcinomas using a toroidal transducer based on preliminary attenuation measurements, Ultrasonics 115 (2021), https://doi.org/10.1016/j.ultras.2021.106459.

[58] E.A.M. O'Flynn, et al., Ultrasound Tomography Evaluation of Breast Density, Invest. Radiol., 52(6), 2017, 10.1097/rli.0000000000000347.

[59] I. Katz-Hanani, T. Rothstein, D. Gaitini, Z. Gallimidi, H. Azhari, Age-Related Ultrasonic Properties of Breast Tissue In vivo, Ultrasound Med. Biol., 40(9), 2014, 10.1016/j.ultrasmedbio.2014.03.034.

[60] C. Li, N. Duric, P. Littrup, L. Huang, In vivo Breast Sound-Speed Imaging with Ultrasound Tomography, Ultrasound Med. Biol., 35(10), 2009, 10.1016/j.ultrasmedbio.2009.05.011.

[61] Y. Sun, Y. Dong, J. Tong, Z. Tang, Ultrasonic propagation parameters in human tissues, Ultrasonics Symposium Proceedings (1986), https://doi.org/10.1109/ultsym.1986.198866.

[62] J. Mendez, Density and composition of mammalian muscle, Metabolism 9 (2) (1960) 184–188.

[63] P. Hasgall, et al., IT'IS Database for thermal and electromagnetic parameters of biological tissues, Version 4, 2018. [Online]. Available: www.itis.ethz.ch/database. [Accessed: 20-Nov-2021].

[64] N.N.A. Nazri, H. Aris, Z. Sauli, W.M.W. Norhaimi, Assessment of stress and strain on women's breast tissue caused by single round malignant tumor, in AIP Conference Proceedings, 2020, vol. 2203, 10.1063/1.5142108.

[65] M.O. Culjat, D. Goldenberg, P. Tewari, R.S. Singh, A review of tissue substitutes for ultrasound imaging, Ultrasound Med. Biol. 36 (6) (2010) 861–873, https://doi.org/10.1016/j.ultrasmedbio.2010.02.012.

[66] E.C. Gregg, G.L. Palagallo, Acoustic impedance of tissue, Invest. Radiol., 4(6), 1969, 10.1097/00004424-196911000-00001.

[67] P. Muleki-Seya, et al., High Frequency Quantitative Ultrasound Spectroscopy of Excised Canine Livers and Mouse Tumors using the Structure Factor Model, Ferroelectr. Freq. Control 63 (9) (2016) 1335–1350.

[68] J.E. Olerud, et al., Ultrasonic assessment of skin and wounds with the scanning laser acoustic microscope, J. Invest. Dermatol., 88(5), 1987, 10.1111/1523-1747.ep12470221.

[69] H.G. Nasief, I.M. Rosado-Mendez, J.A. Zagzebski, T.J. Hall, A Quantitative Ultrasound-Based Multi-Parameter Classifier for Breast Masses, Ultrasound Med. Biol., 45(7), 2019, 10.1016/j.ultrasmedbio.2019.02.025.

[70] H.T. Nyman, A.T. Kristensen, M.H. Lee, T. Martinussen, F.J. McEvoy, Characterization of canine superficial tumors using gray-scale B mode, color flow mapping, and spectral Doppler ultrasonography - A multivariate study, Vet. Radiol. Ultrasound, 47(2), 2006, 10.1111/j.1740-8261.2006.00127.x.

[71] H.T. Nyman, et al., Comparison of B-mode and Doppler ultrasonographic findings with histologic features of benign and malignant mammary tumors in dogs, Am. J. Vet. Res., 67(6), 2006, 10.2460/ajvr.67.6.985.

[72] F.K. Forster, J.E. Olerud, M.A. Riederer-Henderson, A.W. Holmes, Ultrasonic assessment of skin and surgical wounds utilizing backscatter acoustic techniques to estimate attenuation, Ultrasound Med. Biol., 16(1), 1990, 10.1016/0301-5629(90)90085-Q.

[73] M. Terajima, et al., Collagen molecular phenotypic switch between non-neoplastic and neoplastic canine mammary tissues, Sci. Rep., 11(1), 2021, 10.1038/s41598-021-87380-y.

[74] G. Menikou, M. Yiannakou, C. Yiallouras, C. Ioannides, C. Damianou, MRI-compatible breast/rib phantom for evaluating ultrasonic thermal exposures, Int. J. Med. Robot. Comput. Assist. Surg. 14 (1) (2018) 1–12, https://doi.org/10.1002/rcs.1849.